Development of III-V Semiconductor Surface Quantum Wells for Hybrid Superconducting Device Applications

by

Emma Annelise Bergeron

A thesis
presented to the University of Waterloo
in fulfillment of the
thesis requirement for the degree of
Doctor of Philosophy
in
Physics (Quantum Information)

Waterloo, Ontario, Canada, 2024

Examining Committee Membership

The following served on the Examining Committee for this thesis. The decision of the Examining Committee is by majority vote.

External Examiner:	Ray LaPierre Professor, Dept. of Engineering Physics, McMaster University
Supervisor(s):	Jonathan Baugh Professor, Dept. of Chemistry, University of Waterloo
Internal Member:	Robert Hill Professor, Dept. of Physics and Astronomy, University of Waterloo
Internal-External Member:	Zbig Wasilewski Professor, Dept. of Electrical and Computer Engineering, University of Waterloo
Other Member(s):	Jan Kycia Professor, Dept. of Physics and Astronomy, University of Waterloo

Author's Declaration

This thesis consists of material all of which I authored or co-authored: see Statement of Contributions included in the thesis. This is a true copy of the thesis, including any required final revisions, as accepted by my examiners.

I understand that my thesis may be made electronically available to the public.

Statement of Contributions

Material in Chapter 3 has been adapted from,

Bergeron, E. A., F. Sfigakis, Y. Shi, George Nichols, P. C. Klipstein, A. Elbaroudy, Sean M. Walker, Z. R. Wasilewski, and J. Baugh. "Field effect two-dimensional electron gases in modulation-doped InSb surface quantum wells." *Applied Physics Letters*, 122(1):012103, 2023 [10].

Author Contributions:

- Emma Bergeron was responsible for conceptualization, device fabrication, experiments, formal analysis, and visualization.
- Francois Sfigakis contributed to conceptualization of the project, methodology of fabrication and experiments, and data analysis.
- Emma Bergeron and Francois Sfigakis were responsible for writing - original draft and writing - review and editing with contributions from all co-authors.
- Yinqiu Shi performed the growth of InSb heterostructures by molecular beam epitaxy and crystal defect density analysis.
- George Nichols operated the ^{3}He/^{4}He dilution refrigerator.
- Philip Klipstein performed the formal analysis and writing of Section 3.2.4.
- Ahmed Elbaroudy assisted with the growth of InSb heterostructures by molecular beam epitaxy.
- Sean Walker contributed to the transport data analysis.
- Zbignew Wasilewski and Jonathan Baugh supervised the project.

Material from Chapter 4, Chapter 5, and Chapter 6 has been adapted from,

Bergeron, E. A., F. Sfigakis, A. Elbaroudy, A.W.M Jordan, F. Thompson, George Nichols, Y. Shi, Man Chun Tam, Z.R. Wasilewski, and J. Baugh. "High transparency induced superconductivity in field effect two-dimensional electron gases in undoped InAs/AlGaSb surface quantum wells." *Applied Physics Letters*, Submission Number: APL24-AR-JOSE2023-00951 (2024) [11].

Author Contributions:

- Emma Bergeron was responsible for conceptualization, device fabrication, experiments, formal analysis, and visualization.
- Francois Sfigakis was responsible for conceptualization of the project, methodology of fabrication and experiments, and data analysis.
- Emma Bergeron and Francois Sfigakis were responsible for writing - original draft and writing - review and editing with contributions from all co-authors.
- Ahmed Elbaroudy was responsible for the growth of InAs heterostructures by molecular beam epitaxy and assisted in device fabrication.
- A.W.M. Jordan assisted in device fabrication.
- Fiona Thompson assisted with data acquisition and transport data analysis.
- George Nichols operated the ^{3}He/^{4}He dilution refrigerator.
- Y. Shi assisted with the MBE growth of InAs heterostructures.
- Man Chun Tam was responsible for MBE maintenance and general operation.
- Zbignew Wasilewski and Jonathan Baugh supervised the project.

Abstract

This thesis concerns the materials development of both InSb/InAlSb and InAs/AlGaSb surface quantum wells: Two of the most promising platforms for the study of proximity-induced superconductivity in semiconductors with strong spin-orbit interaction. Our work covers the growth, fabrication, and measurement of Hall-bar and Josephson junction devices in both material systems. We optimize surface quantum well heterostructure growth by molecular beam epitaxy (MBE) for single subband occupation and no parasitic parallel conduction. Electronic transport measurements in magnetic fields were carried out on the resulting heterostructures and analyzed.

We highlight issues with the reproducibility of modulation-doped structures in InSb quantum wells and investigate the influence of doping density, buffer choice, growth parameters, and alloy composition on observed parallel conduction in the heterostructure. We show that nominally identical growths can differ by occupation of a parallel conduction channel. We also show that the window for modulation δ doping density between growths is smaller than the observed deviation in calibrated doping densities. We report on the growth, fabrication, and transport characteristics of high-quality, gate-tunable InSb two-dimensional electron gases (2DEGs) in surface quantum wells grown on (001) SI-GaAs substrates. We demonstrate the influence of modulation doping on gating characteristics, magnetotransport behavior, and spin-orbit interaction in two heterostructures, one with and one without a modulation-doped InAlSb layer. Magnetoresistance measurements confirm that intentional dopants in InSb are compatible with high-quality and reproducible transport characteristics, without parasitic parallel conduction or unstable carrier densities. This could be further tested in a 2DEG heterostructure with a short-period InSb/InAlSb superlattice doping scheme, where only the thin layer is doped.

We present the first report of a surface quantum well in the lattice-matched InAs/AlGaSb material system on GaSb substrates. Deep quantum wells in this system have demonstrated record mobilities, by an order of magnitude, over the more commonly reported InAs/InGaAs system, making it a promising platform for topological quantum computing with Majorana zero modes. The surface of the quantum well is protected by lithography techniques designed to protect the surface from unnecessary chemical exposure during fabrication. Our results show that the carrier density is greatly enhanced in a surface quantum well compared to deeper structures and is highly influenced by the choice of gate dielectric in top-gated devices, often pushing the 2DEG into the second subband. However, the gating characteristics of the 2DEG show that the device can be tuned to a single-subband occupation. Josephson junctions with ex-situ sputtered contacts to these InAs surface quantum wells are fabricated using a surface passivation technique. Our lift-off process

for ex-situ sputtered Nb/Ti contacts achieves smooth edges compatible with top-gated devices. We report the observation of induced superconductivity in undoped InAs surface quantum wells using this fabrication process. Two generations of SNS samples were fabricated with ebeam lithography and surface passivation techniques. The interface transparencies of the two generations of samples were determined. We observe a dependence of the critical current on junction length, corresponding to a sensitivity to elastic scattering in the semiconductor. The temperature dependence of the critical current in the junction with arbitrary transparency is modeled by the Kulik-Omelyanchuk relation. The measured excess current, resulting from Andreev reflection processes at the normal/superconducting (SN) interfaces, confirms the presence of phase-coherent behavior in our SNS devices. The process further achieves ex-situ high-transparency superconducting contacts in league with reports of epitaxial aluminum systems to InAs surface quantum wells.

Acknowledgements

I would first like to thank my supervisor, Jonathan Baugh, for the amazing opportunity of pursuing my Ph.D. at IQC where the facilities and people made it possible to undertake this project. I would like to acknowledge my advisory committee, Zbig Wasilewski, Matteo Mariantoni, and Robert Hill, for their advice and support throughout my graduate studies. I also extend thanks to Jan Kycia and Ray LaPierre, for taking their time to be a part of my thesis defence committee. Many thanks are further owed to the staff of QNC-Nanofabrication facility for the astounding facility they maintain. They made it possible to find solutions to all the problems that inevitably arise.

My utmost gratitude goes to the people I have met at IQC who were there for all the ups and downs. To this end, Francois Sfigakis deserves the most thanks for always being there, for being a mentor, answering every question, addressing lab problems at any hour, discussing peculiar data sets, and accompanying overnight measurements. To Zbig Wasilewski, Peyton and Ahmed—the dream team—we made it happen! To George Nichols, for sharing his knowledge of cryogenics and being infinitely understanding and accommodating of tight schedules. To Sean Walker for being a true friend and, most importantly, always being available for a coffee. I don't have to say I will miss our conversations because I know there are more to come, but they were surely a highlight of my years at RAC. On this note, special thanks goes to Chris Dietrich for always having open arms, an ear to listen, and a fresh pot of coffee whenever we needed it. Your presence made a home away from home. To Kay, I have the utmost admiration for you as a researcher and as a friend. You offer support without contingencies and I am glad I was and continue to be a recipient. Lastly, to Pri, I am so grateful that Waterloo gave me my best friend and in all the ways that matter, a sister. Passion, drive, and empathy emanate from you, and I am better for knowing you.

Lastly, I would like to thank my family, especially my mom and dad, for being my base camp. Your endless love and support has given me the confidence to chase my dreams and I am forever grateful. Chloé, for being the best sister in the world. Your beautiful soul and idealism inspires me everyday, but mostly I'm thankful that you remind me constantly that we'll never truly be apart. Corey, for swooping in with the brotherly guidance in all the times I really needed it and for the endless laughs any other time. And Jordan, for your encouragement, support and pride in all pursuits. Without you, it would have been impossible for me to finish this Ph.D. journey, as well fed and as happy as I have been. I cannot thank Canada enough for you and I can not wait for our next adventure together.

Dedication

This is dedicated to my grandmother Shirley Haydel. I love you Mawmaw.

Table of Contents

List of Figures

List of Tables

Chapter 1

Introduction

Since the discovery of the Josephson effect in 1962, the study of hybrid superconducting devices has led to the observation and control of novel phenomena in mesoscopic physics. The Josephson effect first described the existence of tunnel currents across a junction composed of two superconductors separated by a thin insulating barrier. The advancement of materials then allowed for the study of novel effects in Josephson junctions composed of superconductors separated by novel insulators, ferromagnetic materials, normal metals, and semiconductors. Advances in the coupling of superconductors to other materials have motivated and been motivated by the discovery of new materials, new states of matter, advanced heterostructure growth techniques, and advanced nanofabrication techniques. We now have the resources to custom design nanotechnologies with any number of desired material properties.

In this endeavor, semiconductors are at the forefront of fundamental physics research. The advent of semiconductor heterostructure growth earned the Nobel Prize in 2000 for applications in high-speed and opto-electronic applications. Rapid advances in molecular beam epitaxy (MBE) technology have made it possible to produce material heterostructures at unprecedented quality, greatly enhancing the prospects for fundamental research. For example, the 2016 Nobel prize in physics was awarded for the study of topological phases of matter in theoretical condensed matter systems. Nobel laureate David J. Thouless's work theoretically described the quantum Hall effect, the first topological state of matter to be understood as such (and whose experimental discovery earned the Nobel prize in 1985). Since then advances in semiconductor heterostructure growth have led to even higher quality materials (by orders of magnitude), responsible for the observation and pursuit of even more exotic states of matter, like the fractional quantum Hall effect and topological phases hosting Majorana Fermion quasiparticles.

Excitement in the world of experimental condensed matter physics over the possibility of realizing Majorana particles brought the less prevalent III-V semiconductors, InSb and InAs, into the limelight. Although not necessarily new, they were certainly overshadowed by GaAs/AlGaAs until recently. The narrow band gap semiconductors InAs and InSb offer the ability to combine the inherent material properties of strong spin-orbit interaction and Zeeman energy with proximity-induced superconductivity, the combination of parameters that is anticipated to host elusive Majorana quasiparticles [25]. The study of quantum well heterostructures in these two materials and their compatibility with proximity-induced superconductivity is the subject of this thesis.

1.1 Semiconductor Essentials

The following sections review the theoretical foundations of the experimental chapters, but are not to be considered a comprehensive review of the topics discussed. The topics reviewed include the essentials of band structure in semiconductor heterostructures, magnetotransport in quantum wells, and proximity-induced superconductivity, all of which are covered more extensively in the following recommended texts [53, 124, 139, 107]. We hope that topics covered are sufficient for a general understanding of the applied methods used in later chapters.

1.1.1 Band Structure

The behavior of an electron in a two-dimensional electron gas (2DEG) can be understood from the behavior of a free electron accounting for perturbations from the electron's true environment. The energy of a free electron, uninfluenced by any environmental potential energy, is described by a Hamiltonian containing only a kinetic energy term,

$$H_0 = \frac{\hbar^2 k^2}{2m_0}, \tag{1.1}$$

where $\hbar$ is the reduced Plank's constant, m_0 is the mass of an electron, and $\mathbf{k} = k_x\hat{x} + k_y\hat{y} + k_z\hat{z}$ is the electron wavevector. The wavefunction equations describing such an electron are called plane waves given by,

$$\Psi = Ae^{ik\cdot\mathbf{r}} \tag{1.2}$$

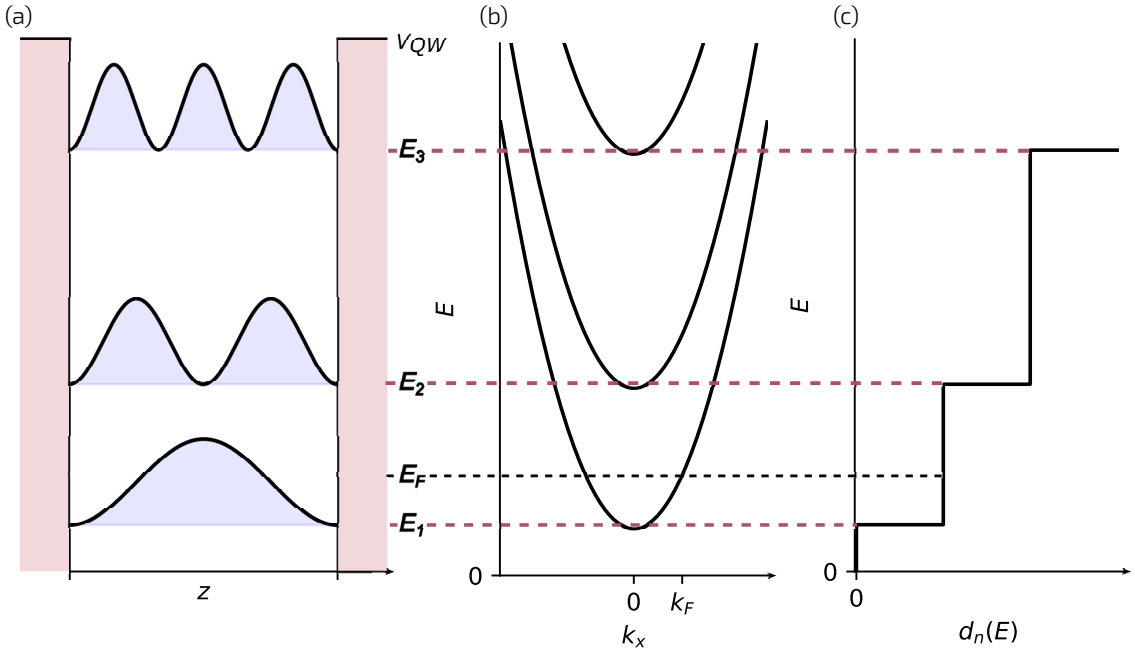

Figure 1.1: (a) Schematic of a quantum well defined by a confining potential V_{QW} in the z-direction. The probability amplitude of the corresponding wave functions are depicted and shifted in energy according to the subband energy spacings illustrated in (b). (c) The total density of states as a function of energy depicting the step-wise increase in the number of states at each subband.

where $\mathbf{r} = x\hat{x} + y\hat{y} + z\hat{z}$ is the position vector. Given the Hamiltonian and a wavefunction describing these free electrons, we can solve the time independent Schrödinger equation

$$H\Psi = E\Psi \tag{1.3}$$

for the energy eigenvalue solutions E. The resulting $\mathbf{k}$- dependent solutions are

$$E = \frac{\hbar^2\mathbf{k}^2}{2m_0}. \tag{1.4}$$

The relation $E(\mathbf{k})$ is known as an energy dispersion and in the case of a free electron it has a parabolic dependence.

Considering now the environment of an electron in a semiconductor crystal, the electron experiences a periodic potential and is described by a Hamiltonian containing both a kinetic energy and a potential energy term,

$$H = H_0 + V(\mathbf{r}), \tag{1.5}$$

where $V(\mathbf{r})$ is the periodic crystal potential energy. This is considered the case of a "nearly-free" electron. The electron wavefunction in this case is described by Bloch's theorem which states that the wavefunctions of particles in a periodic potential are plane-waves modulated by functions periodic with the crystal lattice. From Bloch's theorem we have

$$\Psi_{n\mathbf{k}}(\mathbf{r}) = e^{i\mathbf{k}\cdot\mathbf{r}} u_{n\mathbf{k}}(\mathbf{r}). \tag{1.6}$$

where $u_n(\mathbf{r})$ is periodic over the crystal lattice. The index n denotes the band index of the multiple eigenvalue solutions $E_n(k)$ to the Schrödinger equation. The energy eigenvalues are determined by solving the Schrödinger equation with methods such as the $k \cdot p$ theory where $V(\mathbf{r})$ is treated as a perturbation. The energy eigenvalue solutions compose what is known as the electronic band structure of the crystal. The band structure presents the allowed energy states of electrons which form energy *bands* as well as the energy *gaps* where there are no allowed energies.

Luckily, in the case of electronic transport in semiconductor crystals, the Fermi level resides within the bandgap of the semiconductor and in the case of a direct bandgap semiconductor like InSb only states around the Γ point are involved in transport. For small enough k, near the bottom of the conduction band, the dispersion can be approximated as parabolic and the electron will move like a free-particle with an effective mass m^*. This is known as the effective mass approximation which accounts for the net effect of the periodic potential $V(\mathbf{r})$ via a modified mass, given by

$$m^* = \left(\frac{1}{\hbar^2} \frac{d^2 E}{dk^2} \right)^{-1} \tag{1.7}$$

which is a constant value for an isotropic parabolic dispersion relation. The Hamiltonian then resembles the free-electron Hamiltonian

$$H = \frac{\hbar^2 k^2}{2m^*} \tag{1.8}$$

differing from H_0 by only the effective electron mass m^*. The effective mass approximation is extremely useful for understanding transport near the band edge of semiconductors and is considered an accurate approximation as long as the energy dispersion considered is nearly parabolic.

1.1.2 Two-Dimensional Systems

Continuing from the case of a "nearly-free" electron residing in a crystal lattice, we can see the effects of introducing an additional confining potential. The simplest example is a 1D infinite potential well which can be described by the following potential energy term:

$$V_{QW}(z) = \begin{cases} 0, & 0 < z < w \\ \infty, & z \leq 0,\ z \geq w. \end{cases} \tag{1.9}$$

where w is the width of the potential well. An illustration of this confining potential is depicted in 1.1a. Combining this with the kinetic energy term for a "nearly-free" electron (Eq. 1.8), we have the Hamiltonian H_{QW} for an electron confined to an infinite potential well,

$$H_{QW} = H + V_{QW}(z). \tag{1.10}$$

The wavefunctions are approximated as the periodic component of a Bloch wavefunction at k=0 modulated by an envelope function $F_n(\mathbf{r})$

$$\Psi(\mathbf{r}) = u_{n0}(\mathbf{r})F_n(\mathbf{r}). \tag{1.11}$$

In a 2DEG, electrons are confined in the z-direction but are freely moving in the x-y plane. Confinement in the z-direction leads to energy subbands

$$E_n^z = \frac{\hbar^2}{2m^*}\left(\frac{n\pi}{w}\right)^2 \tag{1.12}$$

However, motion in the x-y plane resembles the case of the "nearly-free" electron. The total energy is therefore the sum of the confinement energy and a kinetic energy term

$$E_n(k_x, k_y) = \frac{\hbar^2 k^2}{2m^*} + E_n^z \tag{1.13}$$

where $k^2 = k_x^2 + k_y^2$ with k_x and k_y denoting the electron momenta along the x and y directions. The n-indexed parabolic bands resulting from this energy dispersion are depicted in Figure 1.1b for momenta along k_x and are presented alongside the resulting probability amplitudes $|\Psi_n(\mathbf{r})|^2$ shifted in energy by their band index in Figure 1.1a. Furthermore, the total density of states (DOS) is given by the number of occupied subbands according to

$$D(E) = \sum_n d_n(E) \tag{1.14}$$

where $d_n(E) = \frac{m^*}{\pi\hbar^2}$ is each 2D subband's energy independent contribution of states as shown Figure 1.1c. The electron density in a 2DEG, in the case of single subband occupation, can be calculated from the density of states according to

$$n = \int_{E_1}^{E_F} dE D(E) = \frac{m^*}{\pi\hbar}(E_F - E_1). \tag{1.15}$$

Since the density of states per unit area is constant up to the Fermi energy at T = 0 in a 2DEG, the wave vector at the Fermi energy is defined by $k_F = E_F - E_1 = \frac{\hbar^2 k^2}{2m^*}$ [5]. We therefore arrive at a relation for the Fermi wavevector in terms of the carrier density,

$$k_F = \sqrt{2\pi n}, \tag{1.16}$$

a measurable quantity in transport experiments.

1.1.3 Boltzmann transport

Though quantum effects appear in two-dimensional systems, much of the intuition can be derived from classical effects. For the scope of this work, the regime of diffusive classical transport in a 2DEG is a good starting point. There is no better start than Ohm's law, the basic law of electron transport

$$\mathbf{j} = \sigma\mathbf{E} \tag{1.17}$$

where $\mathbf{j}$ is the current density, σ is conductivity, and $\mathbf{E}$ is electric field. In a 2D conductor of width w and length l, where the thickness is neglected, the current density is defined as $\mathbf{j} = I/w$. In the diffusive transport regime, scattering of electrons takes place on length scales that are small compared to the size of the device. If an electron undergoes a large

number of scattering events while traversing the sample, the average velocity of an electron in the direction of current (in the absence of magnetic field) is then defined as the drift velocity $\mathbf{v}_D$. The conductivity is related to drift velocity according to

$$\sigma = \frac{-en\mathbf{v}_D}{\mathbf{E}} = -en\mu \tag{1.18}$$

where e is the electron charge, n is the two-dimensional carrier density, and the ratio of the drift velocity to the electric field is referred to as the electron mobility μ. The drift velocity can also be defined in terms of a mean scattering time τ_0 from the Drude model, in which case we define the electron mobility as

$$\mu = \frac{-e\tau_0}{m^*} \tag{1.19}$$

The mobility is therefore inversely related to the frequency of scattering events and is used as a benchmark for crystal quality. From this relationship, we can define a characteristic length scale known as the mean free path,

$$l_e = v_F\tau_0 = \frac{\hbar k_F}{m^*}\tau = \frac{\hbar\mu}{|e|}\sqrt{2\pi n} \tag{1.20}$$

where v_F is the Fermi velocity and k_F is the Fermi wavevector given by the relation $K_F = \sqrt{2\pi n}$. The mean free path is the length scale for the elastic impurity scattering in the diffusive transport regime [53].

1.2 Magnetotransport

1.2.1 Classical Hall Effect

In the classical Hall effect, a voltage transverse to the direction of current is observed in a sample when an external magnetic field is applied. This transverse voltage, proportional to the strength of the magnetic field is called the Hall voltage,

$$U_H = R_H BI \tag{1.21}$$

where R_H is the Hall coefficient, B is the magnetic field, and I is the current [45]. The classical Hall voltage arises when charge carriers in a current are exposed to a magnetic

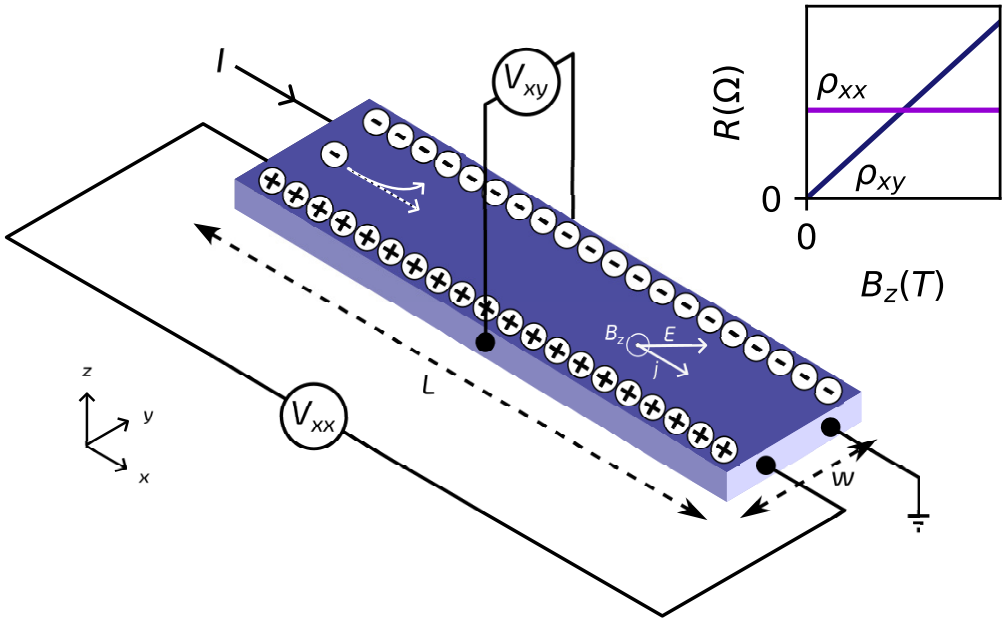

Figure 1.2: Measurement circuit diagram depicting the longitudinal voltage V_{xx} and transverse Hall voltage V_{xy} measurements for a source drain current I oriented in the x-direction and a perpendicular magnetic field B_z. Particles traversing from source to drain along the x-direction experience a Lorentz force which causes a buildup of opposite charges along opposite lengths (L) of the sample and generates an electric field perpendicular to the direction of current as depicted. (Inset) Example of the classical Hall effect with a constant longitudinal resistivity and a linear magnetic field dependent transverse resistivity.

field oriented perpendicular to the direction of current. The resulting Lorentz force is felt by charge carriers in a direction perpendicular to both the velocity and the magnetic field directions according to

$$F = q\mathbf{E} + q(\mathbf{v} \times \mathbf{B}) \tag{1.22}$$

where q is particle electric charge and $\mathbf{v}$ is particle velocity. This causes the accumulation of like charges along the edges of the sample oriented parallel to the current as shown in Figure 1.2. In the figure, the current flows from source to drain in the x-direction and an applied magnetic field is oriented perpendicular to the substrate and thus to the current in the z-direction. The Lorentz force is then felt by carriers in the y-direction and an accumulation of charge generates a compensating electric field

$$E_y = v_x B_z \tag{1.23}$$

where v_x is particle velocity parallel to the current and B_z is the applied magnetic field strength in the z-direction. Due to this additional electric field, the total electric field and the current density enclose an angle that is known as the Hall angle, which approaches zero as B_z approaches zero. In this case the conductivity, defined in Equation (1.17), and therefore the resistivity ρ become 2x2 tensors with diagonal components σ_{xx} and ρ_{xx} and off diagonal elements σ_{xy} and ρ_{xy}. The Hall resistivity

$$\rho_{xy} = \frac{V_{xy}}{I} \tag{1.24}$$

is the transverse voltage V_{xy} divided by the current and can be measured according to Figure 1.2. For a field dependence measurement, the linear relationship of the Hall voltage with respect to magnetic field as in Equation (1.21), is depicted in Figure 1.2 (inset). Also seen in the figure is a measure of the longitudinal resistivity ρ_{xx} which is independent of the magnetic field. The longitudinal resistivity

$$\rho_{xx} = \frac{V_{xx}}{I}\frac{w}{l} \tag{1.25}$$

is a measure of the longitudinal resistance of the sample, $R = V_{xx}/I$ scaled by the length to width ratio l/w of the device geometry. Since resistivity ρ is scaled by the geometry of the sample, it is a far better metric for comparing samples made of the same material but perhaps differing geometries than just resistance R.

From these measurements of the longitudinal and transverse voltages, the 2D carrier density

$$n = \frac{1}{|e|d\rho_{xy}/dB|_{B=0}} = \frac{IB}{eV_{xy}} \tag{1.26}$$

and carrier mobility

$$\mu = \frac{d\rho_{xy}/dB|_{B=0}}{\rho_{xx}(B=0)} = \frac{I(l/w)}{enV_{xx}} \tag{1.27}$$

can be determined. As will be seen in later chapters, the carrier density and mobility are invaluable measurements for understanding the transport behavior of a 2DEG heterostructure.

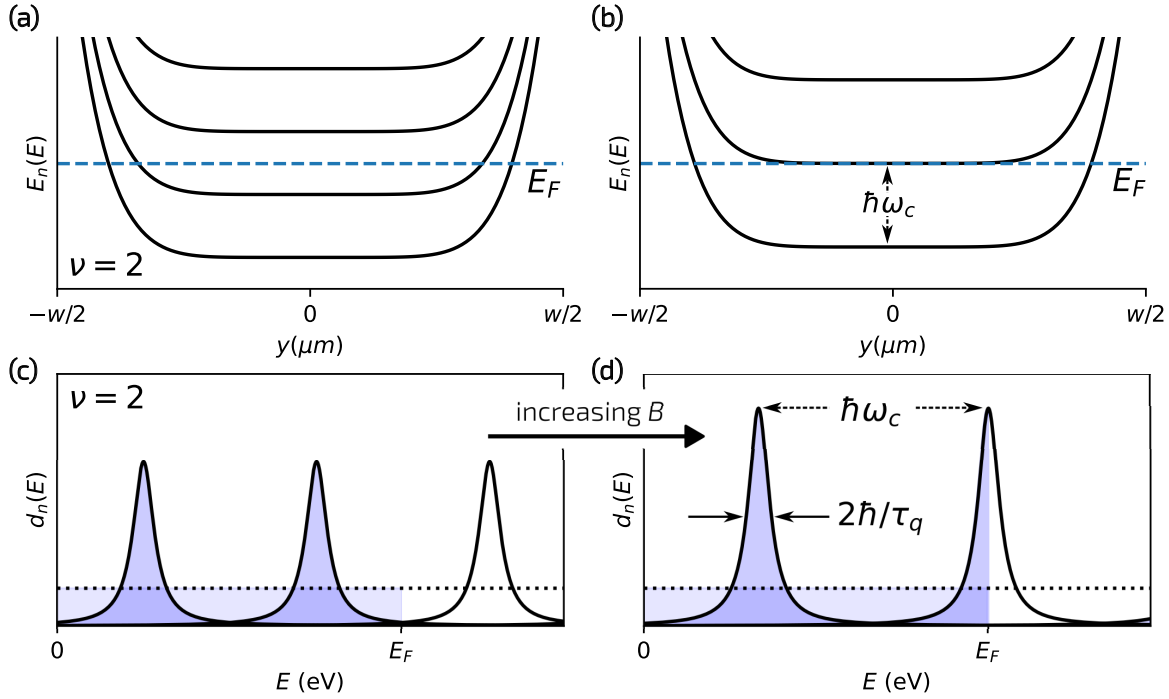

Figure 1.3: (a) Energy subbands with $\nu = 2$ fully occupied Landau levels (LL) below the Fermi energy E_F. The Fermi level lies between two LL's where localized edge states are the only states involved in transport. For increasing magnetic field (b), the space between LL's increases according to $\hbar\omega_c$. In samples with disorder (c,d), LL's are not fully degenerate and are instead broadened in energy with a full width half maximum determined by the quantum lifetime τ_q. As a LL passes through the Fermi energy, extended states near the DOS maximum are involved in transport as shown in (d).

1.2.2 Landau Quantization

The behavior of an electron in a quantum well exposed to a perpendicular magnetic field can be described by the Hamiltonian

$$H = \frac{(\mathbf{p} + |e|\mathbf{A})^2}{2m^*} + V_{QW}(z) \tag{1.28}$$

where $\mathbf{p}$ is the particle momentum, $\mathbf{A}$ is a Landau gauge vector magnetic potential, and $V_{QW}(z)$ is the quantum well potential defined as in Equation (1.9). Choosing a Landau

gauge $\mathbf{A} = (-By, 0, 0)$ which corresponds to $B = (0, 0, B)$ leads to a Hamiltonian describing motion in the z-direction

$$H_z = -\frac{\hbar^2}{2m^*}\frac{\partial^2}{\partial z^2} + V_{QW}(z) \tag{1.29}$$

and the in-plane Hamiltonian

$$H_{xy} = \frac{(p_x - |e|B_z y)^2 + p_y^2}{2m^*}. \tag{1.30}$$

where p_x and p_y are the x and y directed electron momentum. The eigenvalue solutions to the Schrödinger equation are found using the ansatz

$$\Psi(x, y) = e^{-ik_x x}\eta(y). \tag{1.31}$$

Inserting Equation (1.31) and Equation (1.30) into the Schrödinger equation, we get

$$\left[\frac{p_y^2}{2m^*} + \frac{1}{2}m^*\omega_c^2\left(y - \frac{\hbar k_x}{|e|B_z}\right)^2\right]\eta_{k_x}(y) = E\eta_{k_x}(y) \tag{1.32}$$

where the cyclotron frequency is $\omega_c = |e|B/m^*$. This problem resembles that of the one-dimensional quantum mechanical harmonic oscillator with a k_x-dependent center coordinate

$$y_0 = \frac{\hbar k_x}{|e|B_z}. \tag{1.33}$$

The energy eigenvalues are the discrete energy states given by

$$E_n = \hbar\omega_c\left(n + \frac{1}{2}\right) \tag{1.34}$$

which are independent of k_x and the gap between subbands n is given by $\hbar\omega_c$. This implies that all k_x quantum states with the same quantum number n are energetically degenerate. These degenerate states form the so-called Landau levels and the number of allowed k_x states per Landau level is

$$n_L = \frac{|e|B}{h}. \tag{1.35}$$

where h is Plank's constant [69]. In this case, the total number of occupied Landau levels at a given magnetic field (at zero temperature) is given by

$$\nu = \frac{n}{n_L} = \frac{hn}{|e|B} \tag{1.36}$$

and is called the filling factor. Now it is worth noting here that the reality of finite dimensions of any real sample significantly modifies the observation of Landau levels from what has been discussed so far. In reality, a sample must have edges and at the edge of a sample carriers are kept from simply escaping by an edge potential. In this case, the energy subbands increase in energy near the edges of the sample as depicted in Figure 1.3a,b and have a modified form

$$E_n(k_x) = \hbar\omega_c \left(n + \frac{1}{2}\right) + V_E(y_0(k_x)). \tag{1.37}$$

The potential $V_E(y_0(k_x))$ ensures that the center coordinate of the 1D harmonic oscillator (1.33) must reside within the width of the sample $0 < y_0 < w$. This modification means that the system is not gapped at the edges of the sample. Therefore, as the Fermi level passes between quantized Landau levels where there are no states available in the center of the sample, as in Figure 1.3a, there are states from lower energy Landau levels available for transport at the edges of the sample. The group velocity of carriers in edge states is given by the slope of the energy bands

$$v_x = \frac{1}{\hbar}\frac{\partial E_n(k_x)}{\partial k_x} = \frac{1}{\hbar}\frac{\partial E_n(k_x)}{\partial y_0}\frac{\partial y_0}{\partial k_x}. \tag{1.38}$$

Carriers at opposite edges traverse the sample in opposite directions. In other words, edge currents form in which carries have only positive (or only negative) momentum states and thus backscattering is suppressed.

Landau level broadening Furthermore, in a real system the Landau levels are also not perfectly degenerate, there is finite broadening in energy due to imperfections in the crystal that lead to spatial potential fluctuations. This broadening is often modeled by a

Lorentzian distribution in the DOS as depicted in Figure 1.3c,d with a width characterized by the quantum lifetime τ_q, also known as the single-particle relaxation time of the system. Therefore, when the Fermi level is aligned with a Landau level, as in Figure 1.3b, carriers can scatter into available states throughout the sample with differing group velocities due to impurity potential fluctuations, leading to a finite resistance.

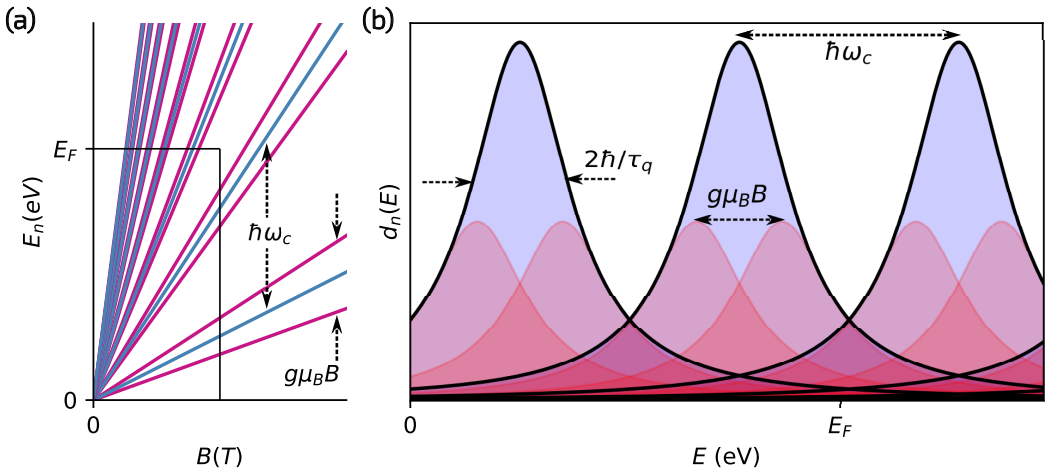

Figure 1.4: Spin Splitting. (a) Spin degenerate Landau levels are spin split according to $E_z = g\mu_B B$. (b) For large enough magnetic fields and sufficiently low disorder, spin degenerate Landau levels are observable in experiment.

Zeeman Energy For materials with large Landé g-factors, such as InAs and InSb, the Landau levels are further discretized by spin splitting according to

$$E_n^{\pm} = \hbar\omega_c \left(n + \frac{1}{2}\right) \pm \frac{1}{2} g^* \mu_B B_z \tag{1.39}$$

where g is the Landé g-factor, and μ_B is the Bohr magneton. The magnetic field dependence of the Landau level spacing $\hbar\omega_c$ and spin splitting due to the Zeeman energy $g\mu_B B$ are depicted in Figure 1.4a. The density of states for the magnetic field coordinate denoted in 1.4a is illustrated in Figure 1.4b where finite broadening due to scattering has been included. Spin splitting is observable in magnetotransport measurements when $g\mu_B B > \hbar/\tau_q$ and $g\mu_B B > k_B T$.

Spin-orbit interaction In previous sections, we approximated that electrons confined to a 2DEG have a spin-degenerate (independent of spin) parabolic dispersion relation with a curvature related to the effective mass. We now intend to modify this to account for the influence of spin-orbit coupling. Broadly speaking, spin-orbit interaction (SOI) is defined as the interaction of a particle's spin with its motion inside a potential. In a semiconductor heterostructure, spin-orbit effects can arise from bulk inversion asymmetry (BIA) of the crystal through Dresselhaus SOI or structural inversion asymmetry (SIA) of the confinement potential in a quantum well through Rashba SOI. In either case, it leads to a zero magnetic field spin splitting of the energy subbands. It can be accounted for when solving the Schrödinger equation by including the effective first-order Hamiltonians of the Rashba and Dresselhaus SOI

$$H_R = \frac{\alpha}{2}(\sigma_x p_y - \sigma_y p_x) \tag{1.40}$$

$$H_D = \frac{\beta}{2}(\sigma_x p_x - \sigma_y p_y) \tag{1.41}$$

where α is the Rashba coefficient, β is the linear Dresselhaus coefficient, and σ_x and σ_y are the Pauli spin matrices [101, 28]. Assuming a dominant Rashba contribution to the Hamiltonian, the energy dispersion of a 2DEG to the lowest order in $\mathbf{k}$ becomes

$$E_{\pm} = \frac{\hbar^2 k^2}{2m^*} \pm \alpha k \tag{1.42}$$

where $k = \sqrt{k_x^2 + k_y^2}$. We can see that the effect of SOI in semiconductor heterostructures is the spin splitting of the energy bands proportional to the parameter α along the axis k.

The strength of SOI in a 2DEG is determined by measuring two characteristic length scales: spin coherence length (l_{SO}) and phase coherence length (l_ϕ). In systems with strong SOI, the spin dynamics of the carriers is coupled to their orbital motion, leading to interference of time-reversed partial waves of the charge carriers. As the spin undergoes scattering events along its trajectory, its orientation is randomized over the spin-orbit scattering length l_{SO}. The smaller the value of l_{SO}, the stronger the SOI. In this scenario, the interference of time-reversed paths reduces the probability of backscattering below its classical value at zero magnetic field, resulting in the weak antilocalization effect (WAL) [42, 105, 106]. This effect can be observed when l_{SO} is much smaller than l_ϕ, and allows the experimental determination of the SOI strength in disordered systems using appropriate models [51, 55].

1.2.3 Shubnikov de Haas Oscillations

The changes discussed so far in the 2D density of states of a 2DEG due to the presence of a magnetic field can be observed through a phenomenon known as Shubnikov-de Haas oscillations at cryogenic temperatures and for small magnetic fields [109]. For small magnetic fields where the LL spacing is small and the number of occupied LLs is large, the total DOS D_{2D} approaches the constant $B = 0$ DOS of a 2DEG as depicted in Figure 1.5a.

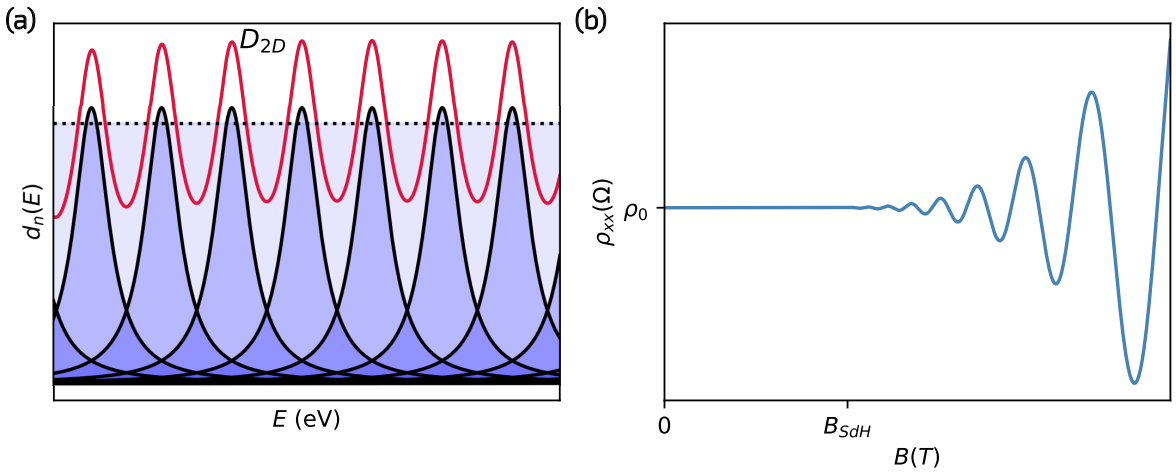

Figure 1.5: Density of states. (a) The total spin degenerate DOS D_{2D} shown in red is the sum over the DOS of each Landau level $d_n(E)$ shown in blue. As $B \to 0$, the discrete Landau levels approach the constant 2D density of states marked by the dotted line. (b) The effects of an oscillatory DOS are observable in a measurement of Shubnikov de Haas oscillations. The onset of observable oscillations B_{SdH} depends on the quantum lifetime and thermal damping and is smallest for high quality samples measured at low temperatures.

However, for larger magnetic fields, oscillations in ρ_{xx} are observed if the magnetic field-dependent spacing between landau levels $\hbar\omega_c$ is larger than the broadening due to scattering $\hbar/\tau_q$. The oscillatory behavior in ρ_{xx} corresponds to Landau levels in the density of states crossing the Fermi level, with a period related to the inverse magnetic field,

$$\Delta(1/B) = \frac{2e}{nh} \tag{1.43}$$

where the factor of 2 accounts for spin degeneracy at low fields and $\Delta(1/B)^{-1}$ is the frequency of oscillations as a function of inverse magnetic field. Oscillations in the resistivity

component ρ_{xx} are unlike the constant resistivity predicted by the Drude model. The resistivity reflects the DOS in this scenario. When an LL resides at the Fermi level, resistance peaks because the ratio of carriers to available states to scatter into is the highest. Similarly there is a minimum in resistance as current through the bulk is suppressed, and back-scattering is not possible for edge channel current. These oscillations are modeled by

$$\rho_{xx}(B,T) = \frac{m^*}{ne^2\tau_0}\left[1 - 2e^{-\pi/(\omega_c\tau_q)}\frac{\chi(T)}{\sinh\chi(T)}\cos 2\pi\frac{hn}{2eB}\right] \tag{1.44}$$

where T is temperature and

$$\chi(T) = \frac{2\pi^2 k_B T}{(\hbar\omega_c)}. \tag{1.45}$$

These oscillations are presented in Figure 1.5b where the onset of oscillations is related to the quantum lifetime [53, 26, 20]. Assuming the sample temperature is low enough for thermal damping to be neglected, the envelope of oscillations is described by τ_q according to

$$\frac{\Delta\rho_{xx}}{\bar{\rho}_{xx}} = \pm 2e^{-\pi/(\omega_c\tau_q)}\frac{\chi(T)}{\sinh\chi(T)}. \tag{1.46}$$

This method is used to determine the quantum lifetime of samples in later chapters [53].

1.2.4 Integer Quantum Hall Effect

The integer quantum Hall effect occurs for large magnetic fields where vanishing longitudinal resistivity in the SdH oscillations corresponds to a plateau in the Hall resistivity at

$$B_i = \frac{nh}{i|e|} \tag{1.47}$$

where $i = 1, 2, 3...$ is an integer and corresponds to the number of filled Landau levels at a given magnetic field. The plateaus in the integer quantum Hall effect therefore line up with the minima in the SdH oscillations. Remarkably, observation of this phenomenon is entirely dependent on the presence of edges in the Hall bar geometry. If it were not for edges, we would expect zero conductance and infinite resistance at large magnetic

fields where the LLs would be fully occupied. Instead, we find vanishing longitudinal resistance due to the presence of edge states from an additional confining potential caused by the edges of the samples as described in Equation (1.37) for the modified Landau-level subbands. Furthermore, unlike the linear magnetic field dependence of the Hall resistivity in the Drude model, the transverse resistivity will exhibit quantized resistance plateaus at magnetic fields corresponding to the minima in ρ_{xx}. In the 2x2 tensor notation of resistivity and conductivity in the presence of magnetic fields, Hall plateaus corresponds to $\rho_{xx} = 0$ and $\sigma_{xx} = 0$, while ρ_{xy} and σ_{xy} remain finite [54]. As it turns out, the plateaus are quantized at remarkably precise values corresponding to

$$\rho_{xy} = \frac{h}{\nu e^2} \tag{1.48}$$

where ν is the LL filling factor corresponding to the number of occupied edge channels. The value for $\nu = 1$ is known as the von Klitzing constant and has been measured to such precision that it is used as the metrology standard for resistance in the SI units [65].

1.3 Comparison of III-V material systems

Equipped with a basic theoretical understanding of two-dimensional quantum well systems in a crystalline material, we now introduce the specific III-V semiconductor material systems studied in this work and their relevant properties.

1.3.1 Bandgap Engineering

In materials science, Vegard's law is the rule of thumb for varying the electrical properties of an alloy through alteration of its chemical composition. Vegard's law for the bandgap energy E_g^{alloy} of a ternary alloy $A_{1-x}B_xC$ with alloy composition x is given by

$$E_g^{alloy}(x) = (1-x)E_g^{AC} + xE_g^{BC} \tag{1.49}$$

where E_g^{AC} and E_g^{BC} are the bangap energies of the binaries. The law states that the material parameters of the alloys, such as the lattice constant, the band gap, and the dielectric constant, vary linearly with the alloy composition x. Sometimes, the linear interpolation between the band gap energies is not accurate enough, and a second term to

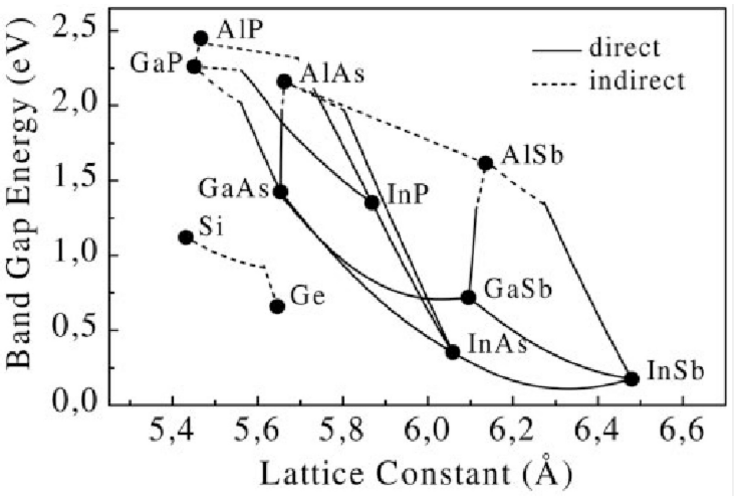

Figure 1.6: Bandgap energy versus lattice constant of III-V semiconductors measured at room temperature (Reprint from Schubert (adopted from Tien, 1988)[108].

account for the curvature of the band gap energies as a function of composition is added. This curvature correction is characterized by the bowing parameter:

$$E_g^{alloy}(x) = (1-x)E_g^{AC} + xE_g^{BC} - x(1-x)b \tag{1.50}$$

where b is the bowing parameter that accounts for the deviation from a linear interpolation between the bandgaps of the two binaries AC and BC. The band parameters including the bowing coefficients for a number III-V compound semiconductors and their ternary alloys have been determined [131, 134]. The variation in band gap as a function of lattice constant for common III-V materials is given in Figure 1.6. Through the art and science of molecular beam epitaxy, materials can be combined while maintaining the standard of a high-quality single crystal. If the bandgap alignment is chosen carefully, a quantum well potential profile can be achieved and carriers are confined to a 2DEG. This work studies quantum well heterostructures formed using the small band gap III-V semiconductors InAs and InSb. These two binary semiconductors have the narrowest energy band gaps, the smallest effective electron masses, the largest Landé g-factor, and the strongest spin-orbit interactions of all III-V compound semiconductors.

1.3.2 Origin of carriers

Charge carriers have traditionally been introduced to quantum wells through a method known as doping. In the case of III-V semiconductors, doping with either acceptor or donor atoms is achieved by introducing either group II, IV, or VI atoms as impurities during the crystal growth. A common method of doping is modulation doping, which introduces dopants outside the transport channel. Delta-doping is a form of modulation doping that introduces dopants in a single atomic plane of the growth that is located in a different layer some distance away from the quantum well. Modulation doping reduces ionized impurity scattering by spatially separating donated carriers in the quantum well from their ionized donor atoms and has historically led to records in carier mobilities measured in heterostructure quantum wells [97].

InAs/AlGaSb The staggered conduction band lineup of small band gap InAs and high band gap (Al, Ga)Sb leads to very deep quantum wells, which provide excellent electron confinement and generally high electron density in quantum well heterostructures without the need for modulation doping. The origin of carriers in this case varies. At InAs/(Al, Ga)Sb interfaces, both the cation and the anion change at the interface. This implies that there are two possible bonding configurations available at the interface, In on Sb or As on Al (or Ga). It has been shown that As on Al anti-site defects are attributed to the enhancement of electron concentration in InAs quantum wells similar to the method of modulation doping. Unfortunately, the lack of a spacer layer between the ions and donated electrons leads to enhanced ionized impurity scattering and the degradation of mobility. Fortunately, the In on Sb interface does not exhibit these deleterious effects and the type of interface can be controlled in MBE through proper shutter sequences.

Although even with In-on-Sb interfaces, InAs/AlGaSb heterostructures still exhibit large electron densities without doping. Remaining sources of free carriers include deep donors from background impurities, since the band offset between AlGaSb and InAs is large, and surface states from surface impurities if the quantum well is sufficiently close to the surface as in our case.

InSb/InAlSb Unlike the InAs system above, InSb/InAlSb is a far shallower quantum well and has a Schottky barrier at the surface which prevents conduction through surface states. Therefore, it is not conductive without intentional doping. As will be discussed in later chapters, it remains an open question as to why InSb heterostructures respond comparatively poorly to modulation doping.

1.4 Superconductivity

The Bardeen–Cooper–Schrieffer (BCS) theory is a microscopic theory of superconductivity that explains the behavior of superconducting materials at very low temperatures [7]. It is based on the idea that electrons of opposite wave vector and spin (**k**, -**k**) in a superconductor form pairs, called Cooper pairs, which are bound together by a pair–forming potential mediated by the electron–phonon interaction. These pairs condense to a lower ground state energy of the system, leaving a gap Δ in the superconducting density of states. Cooper pairs move through the material at $E = 0$ (midgap) without resistance, allowing for the flow of electricity without any energy loss [124, 8, 82].

Excitations in the condensate of Cooper pairs are described by the Bogoliubov-de Gennes (BdG) equation

$$\begin{bmatrix} H(\mathbf{r}) & \Delta_0 \\ \Delta_0^* & H(\mathbf{r}) \end{bmatrix} \Psi_k(\mathbf{r}) = E\Psi_k(\mathbf{r}) \tag{1.51}$$

where a homogeneous superconductor $\Delta(\mathbf{r}) = \Delta_0$ was assumed [24]. The two-component wavefunction $\Psi_k(\mathbf{r})$ includes the electron (v_k) and hole (u_k) character of the state. At $\Delta = 0$ the free particle solutions would be real electron and hole states described by the single particle Hamiltonian

$$H(\mathbf{r}) = -\frac{\hbar^2}{2m^*}\nabla^2 + V(\mathbf{r}) - \mu_c \tag{1.52}$$

where $V(\mathbf{r})$ is a scalar potential and μ_c is the chemical potential. Nonzero Δ changes the character of the solutions which become coupled electron-like and hole-like states. A simplified solution is obtained for $V(\mathbf{r}) = 0$ with

$$\Psi(\mathbf{r}) = e^{i\mathbf{k}\cdot\mathbf{r}} \begin{pmatrix} u_0 \\ v_0 \end{pmatrix}. \tag{1.53}$$

In this case, the BCS coherence factors are expressed as

$$u_0^2 = \frac{1}{2}\left(1 + \frac{\sqrt{E^2 - \Delta_0^2}}{E}\right) \tag{1.54}$$

$$v_0^2 = 1 - u_0^2 \tag{1.55}$$

with energy eigenvalue solutions

$$E = \pm\sqrt{\left(\frac{\hbar^2 k^2}{2m^*} - \mu_c\right)^2 + |\Delta_0|^2}. \tag{1.56}$$

Noticeably, the energy dispersion for a superconductor ($\Delta > 0$) in Equation (1.56) evolves to the energy dispersion of a normal metal for $\Delta = 0$. The induced gap in a superconductor energy dispersion is the difference between the energy of the highest occupied single-particle state and the lowest unoccupied single-particle state. This gap is caused by the pairing of electrons in the superconductor, which creates a gap in the energy dispersion of the material. Although there are no single particle states available within the gap, transport for $E < 0$ can occur through Cooper pairs that condense into a highly correlated, energetically favorable ground state pinned midgap at E = 0.

From Equation (1.56), the superconducting density of states can be inferred. A superconductor can be thought of simply as a metal with a gap around E_F, allowing comparison of the DOS of the superconductor with the DOS in a normal metal, while remembering to account for the gap. In this way, we can write the density of states according to

$$d_{SC}(E) = \begin{cases} \frac{E}{\sqrt{E^2-\Delta^2}} & E > \Delta \\ 0 & E < \Delta. \end{cases} \tag{1.57}$$

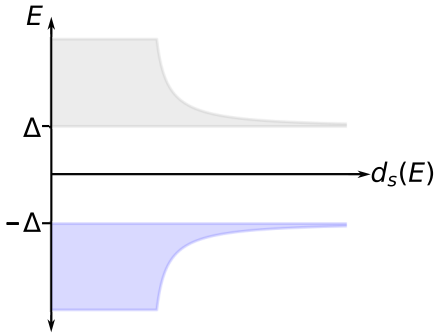

Figure 1.7: The density of states $d_{SC}(E)$ in a superconductor. The states with $E < |\Delta|$ have been pushed out of the gap.

In Figure 1.7, the density of states of quasiparticles in the superconductor is plotted as a function of energy, illustrating the appearance of an energy gap of magnitude Δ around E_F. For $E > \Delta$ there is immediately an enhanced density of states available for single-particle transport due to states that have been pushed out of the gap due to the superconductive pairing. However, in the following section, we will see the interesting implications that arise for a particle attempting to enter a superconductor with energy $E < \Delta$.

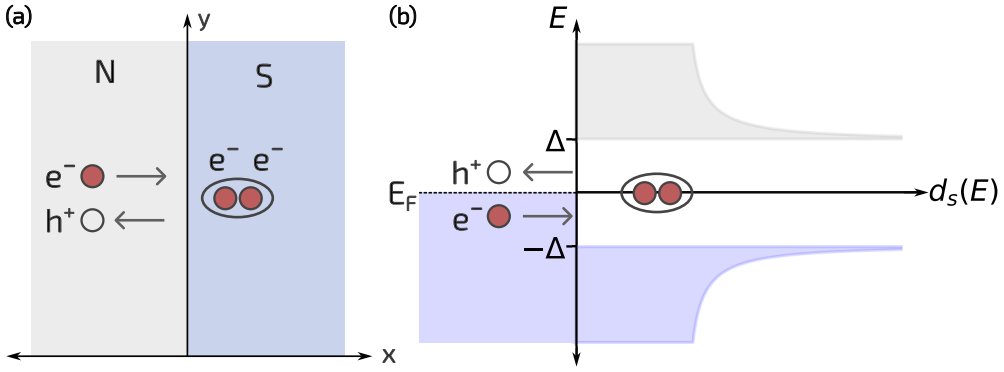

Figure 1.8: Andreev Reflection. (a) Spatial representation where a hole retroreflects along the same path as the incident electron in the semiconductor and a Cooper pair is transmitted into the superconductor. (b) Energy representation where an incedent electron with energy less than $|\Delta|$ at the NS interface retroreflects a hole symmetrically about the Fermi energy in the seminconductor and a Cooper pair is transmitted into the SC.

1.5 Hybrid structures

For an ideal superconductor/normal conductor interface, a single electron in the normal metal with energy $E < \Delta$ cannot transmit into the superconductor if there are no available single-particle states. The electron also cannot normal reflect without a barrier present at the interface. Therefore, the only way for an electron to "transmit" into a superconductor is via a Cooper pair. In this case, the process known as Andreev reflection occurs at the interface. For an electron incident on an NS interface at $E < \Delta$, the process of Andreev reflection transmits a Cooper pair into the superconductor by retro-reflecting a hole. The hole retro-reflects because a Cooper pair is made of electrons of opposite spin and wavevector ($\mathbf{k} \uparrow$, $\text{-}\mathbf{k} \downarrow$). Therefore, the hole must have the same wavevector as the incident electron, and since holes have a group velocity opposite to the wavevector, we deem this "retro-reflection". The conductance is double that of ideal normal transmission, because the Andreev reflection process produces a net charge transfer of $2|e|$ across the interface [107].

Hybrid superconductor/semiconductor devices exhibiting evidence of the Andreev reflection process have been realized in a number of device architectures including semiconductor surface inversion layers, buried quantum well heterostructures, and semiconductor nanowires [107, 39, 90, 57]. The hybrid surface quantum well structures that are the subject of this dissertation offer a more scalable platform for future large-scale networks of

hybrid devices. With this platform, a superconductor deposited directly on the surface and therefore in proximity to the quantum well, makes contact to a high-quality 2DEG therein [140]. The exceptional quality of hybrid devices in this platform is evidenced by a growing interest in topological quantum computing with Majorana fermions in this architecture [103, 142, 143].

1.6 Structure of this dissertation

In this thesis, the chapters are structured around the development of two III-V quantum well material systems, InSb and InAs. The first two experimental chapters are dedicated to InSb heterostructure development. Chapter 2 covers the long road to optimizing heterostructure growth in standard quantum wells where we show that the transport properties of nominally identical growths can differ significantly. Our work on InSb heterostructure growth culminates in Chapter 3, based on our published manuscript, where we report on the growth, fabrication, and transport characteristics of high-quality, gate-tunable InSb *surface* quantum wells (SQW).

In Chapter 4 we move to the second material system of this thesis and present the first report of a SQW in the InAs/AlGaSb material system on GaSb substrates. Our results show that the carrier density is greatly enhanced in a SQW compared to deeper structures and is compatible with the fabrication of superconducting devices which is the subject of Chapter 5. The fabrication process achieves ex-situ high-transparency superconducting contacts to semiconductors in league with reports of epitaxial systems. In Chapter 6 we report the observation of induced superconductivity in undoped InAs SQWs from 4 using this fabrication process.

Chapter 2

Developing InSb heterostructures

The most apparent challenge in the growth of InSb heterostructures concerns the lack of lattice matched, semi-insulating III-V substrates. InSb heterostructures are therefore primarily reported on readily available GaAs or GaSb substrates which have large lattice mismatches of 14.6% and 6.3%, respectively, to InSb. In heteroepitaxial growth, lattice mismatch will lead to the generation and propagation of strain relaxing dislocations especially in highly-mismatched systems. Among the types of generated dislocations, *threading* dislocations are particularly detrimental to device performance as they are capable of propagating in the growth direction and into the active region of the heterostructure. Introducing *metamorphic buffer* systems, one or more layers of intermediate materials between the substrate and active region, are common practice for impeding the propagation of dislocations. Standard InSb heterostructures grown on GaAs substrates are investigated in this chapter with metamorphic buffers consisting of AlSb or GaSb as the first intermediate buffer and ternary $Al_xIn_{1-x}Sb$ as the second-stage buffer to bring the lattice constant of the material structure from that of the GaAs substrate to that of the InSb QW. We investigate first and second intermediate buffers for their electrical isolation and threading dislocation densities (TDD) and achieve InSb QW structures with a TDD of 1×10^8 cm^{-2}.

Near the active region, ternary $Al_xIn_{1-x}Sb$ barriers are generally employed but the mismatch introduces a trade-off in barrier composition between minimizing strain in the crystal lattice and providing sufficient confinement of charge carriers in the quantum well. The absence of a lattice matched, high band gap III-V material to InSb means quantum well confinement is limited by reduced barrier heights compared to other III-V systems. To this end, ternary $Al_xIn_{1-x}Sb$ barriers with $0.09 \leq x \leq 0.12$ are employed in this chapter to balance lattice mismatch with sufficient confinement of carriers. Modulation-doped InSb/AlInSb heterostructures are also frequently reported with unintentional parallel con-

duction channels [76, 100, 68, 77]. The parallel channel can in some cases prevent full depletion of a device by the field-effect, preventing applications towards quantum devices. Such channels are often attributed to insufficient isolation of the metamorphic buffer or too high a modulation doping density. The influence of doping density, buffer choice, growth parameters and alloy composition on observed parallel conduction in standard quantum well heterostructures is explored in this chapter. Fabrication and measurement of a top-gated Hall-bar further reveals the influence of the field effect on total carrier density in the heterostructure. However, in foresight of eventual proximity-superconducting devices, the use of standard quantum well heterostructure with modulation doping located between the 2DEG and the surface would be detrimental. In this regard, inverted structures are required. The issues with inconsistency of parallel conduction studied here would, however, persist. In that regard, we propose next the use of back-gating as a solution to parallel conduction in inverted heterostructures.

Back-gate designs involve contacting a metallic (degenerately-doped) layer beneath the quantum well that can be used to apply the field effect. Back-gates are previously reported in InAs and GaAs heterostructures, but are proposed here as a novel solution to the parallel conduction problem discussed above that would persist in inverted InSb heterostructures. Applying a negative voltage on a back-gate would deplete the parallel channel in an inverted InSb heterostructure, eliminating issues with inconsistent tuning of the doping layer. Combination with a top-gate for tuning of the quantum well carrier density, ensures the back-gate operates only in the depletion regime where barrier confinement is not at risk. Both n-$Al_xIn_{1-x}Sb$ and n-GaAs are investigated for their potential in forming back-gates in the present buffer structures. Fabrication is a significant challenge since InSb is typically grown below 400 °C, a temperature approached or even exceeded by a number of standard fabrication processes. It is generally accepted that adhering to a thermal budget below 200°C is necessary to avoid degradation of electron transport in InSb quantum well heterostructures . We survey conventional methods of making contacts to n-GaAs without the use of high temperature anneals for applications at cryogenic temperatures which to our knowledge remains unreported in the literature.

2.1 Nucleation buffer layer growth

The first step in understanding the challenges of InSb heterostructure growth is evaluating the implications of lattice mismatch. In a system with large lattice mismatch, it is energetically favorable for the crystal to relieve strain through the formation of *misfit* dislocations at the interface. In lattice mismatched heterostructures like InSb on GaAs, it is necessary

to include an intermediate layer that can systematically transition the lattice from that of the substrate to that of the quantum well material in a way that reduces the density of dislocations formed from relaxation of the crystal. This layer is known as a *metamorphic* buffer layer and is an essential component for reducing strain relieving misfit dislocations and preventing propagation of defects to the quantum well.

The structures described here are composed of a first and second intermediate buffer to reduce the density of dislocations. Our choices for a first intermediate buffer, AlSb or GaSb, belong to the 6.1Å family of materials that reside halfway between the lattice constants of GaAs and InSb. Although AlSb has a longer history of use in InSb heterostructures and is reported more frequently, it has been shown that GaSb buffers can achieve comparatively lower dislocation densities [52, 9]. We therefore tested the use of both materials. The growth parameters of AlSb and GaSb buffers that were varied in this section are provided in Table 2.1. We characterize the buffers by their four-terminal resistance and dislocation density. The dislocation densities were quantified by the density of propagating *threading* dislocations (TDD) that are visible by scanning electron microscopy (electron channeling contrast imaging) at the surface of the crystal. Our AlSb first intermediate buffer is electrically isolating on the order of GΩ but exhibits a dislocation density of 2.6×10^9 cm^2. For GaSb, we noticed an inverse relationship between dislocation density and resistance as a function of growth temperature. Our GaSb first intermediate buffer is only insulating on the order of GΩ for a growth temperature of 400 °C but has a comparable dislocation density to AlSb. For higher growth temperatures up to 510 °C, the dislocation density improves but the buffer reduces to only MΩ of resistance. Having previously observed parallel conduction in buffers below GΩ of resistance, the poor buffer isolation of GaSb grown at 510 °C makes it a poor choice for quantum well heterostructure growth despite the improved dislocation density. Given these results, our chosen quantum well heterostructure design in the following sections maintains an AlSb first intermediate buffer since GaSb buffers were unable to provide substantial improvement in dislocation density while maintaining sufficient electrical isolation, a parameter often neglected in reports focused on crystal growth. For further details on the growth conditions of the GaSb intermediate buffers described here, the reader is directed to the dissertation by Yinqiu Shi [115].

2.2 Standard InSb Quantum Wells

Optimization of growth parameters for InSb quantum well heterostructures began with "standard" quantum well heterostructures where the quantum well is protected from the surface by a barrier layer composed of a high band-gap material. Standard as opposed to

Sample ID	Material	Growth T (°C)	ρ	TDD (cm^{-2})
G152	1 μm AlSb/5 nm GaSb	550	> GΩ	2.6e9
G671	600 nm GaSb	510	0.9 MΩ	8.1e8
G673	600 nm GaSb	450-510	1.3 MΩ	8.4e8
G672	600 nm GaSb	450	25 MΩ	8.8e8
G682	600 nm GaSb	400	> GΩ	1.2e9

Table 2.1: First intermediate buffers on GaAs substrates. The growth of GaSb buffers is varied only by the reported substrate growth temperatures. The four terminal resistances were measured in the Van der Pauw geometry at a base temperature of T = 1.5 K. Threading dislocation densities provided by Yinqiu Shi were characterized using scanning electron microscopy- electron channeling contrast imaging.

surface quantum wells allow us to diagnose the effect of growth conditions on the quality of electronic transport without the added implications of surface effects. In an effort to minimize the vast parameter space of possible combinations of both heterostructure design choices and MBE growth conditions, we settled on the heterostructure presented in Figure 2.1a which reduced the scope of our investigation to specific changes in buffer elements, growth temperatures, V/III ratio, and aluminum alloy composition x in the barrier and buffer layers.

The heterostructure design begins with a semi-insulating GaAs (001) substrate followed by a 120 nm GaAs smoothing layer, a 100 nm AlSb first intermediate buffer and a 4 μm thick single composition $Al_{0.1}In_{0.9}Sb$ second-stage buffer layer. In addition to being a metamorphic buffer which reduces the density of dislocations through strain relief at the interface, this buffer also relies on the method of thickness dependent dislocation filtering wherein dislocations are allowed to self-annihilate before growth of the active region. A single composition buffer structure also allows for an easier optimization of growth conditions as compared to more intricate buffer layer structures where discerning which layers are contributing to undesirable transport becomes difficult [74]. Following growth of the buffer, the active region of the heterostructure begins with a 30 nm thick InSb quantum well followed by a 20 nm thick $Al_{0.1}In_{0.9}Sb$ spacer layer. The spacer layer separates the quantum well from a silicon δ-doping layer of density N_d. The growth is then completed with a 50 nm thick $Al_{0.1}In_{0.9}Sb$ upper barrier layer.

Most of the samples in this section were measured in the Van der Pauw geometry depicted in Figure 2.1b, unless noted to be a Hall bar [129]. In this method, the Ohmic contacts are prepared by gently scribing the sample surface to expose the buried quantum well and soldering a drop of pure indium onto the scribe to improve electrical contact with

the 2DEG in the quantum well. The simpler preparation of a Van der Pauw sample compared to a fabricated Hall bar minimizes fabrication related discrepancies between samples and provides a faster feedback loop between transport measurements and heterostructure growth.

Using standard ac lock-in measurement techniques, I performed four terminal magnetotransport experiments in a magnetic field up to $B = 5.5$ T in a pumped ^{4}He cryostat with a base temperature of 1.6 K. The measured mobility and density of the active region of the quantum well together with the characteristic features of the Shubnikov de Haas oscillations and integer quantum Hall effect will be used extensively to determine the effects of small changes in growth conditions on the quality of electron transport.

2.2.1 Tuning the doping density

The method of modulation doping introduces charge carriers to a quantum well that are spatially separated from their ionized donor atoms by an undoped "spacer" layer. In our case, silicon is introduced during the growth of the AlInSb barrier where it will have one spare electron per atom. The spare electrons will preferentially populate the smaller band energy region of the quantum well thereby becoming spatially separated from their now ionized parent atoms [40, 95, 138]. However, the silicon atoms will also bend the conduction band in the AlInSb layer towards the Fermi level and, if increased enough, will give rise to a parallel (and often considered parasitic) conducting channel to the quantum well. Precise tuning of the doping density of a modulation layer is therefore essential in determining the transport properties of a quantum well heterostructure.

Sample ID	δ (cm^{-2})	μ (cm^2/Vs)	n_{2D} (cm^{-2})	$n_{\|\|}$ (cm^{-2})
G617 (HB)	1×10^{12}	D.N.C	D.N.C	0
G637	1.5×10^{12}	5.3×10^4	1.66×10^{11}	0.2×10^{11}
G602 (HB)	2×10^{12}	4.4×10^4	2.3×10^{11}	5.1×10^{11}

Table 2.2: Comparison of InSb quantum well growths G617, G637, and G602 in order of increasing δ-doping density. Mobility, 2D carrier density, and parallel conduction of all samples were measured at 1.6 K. As denoted, G617 and G602 were measured in the Hall bar geometry (not VDP). Samples that did not conduct are denoted D.N.C.

In our first series of growths, we optimized the delta doping density of the heterostructure presented in Figure 2.1a for observation of single channel conduction. Three samples were grown by Peyton Shi with delta doping densities N_d corresponding to 1×10^{12} cm^{-2},

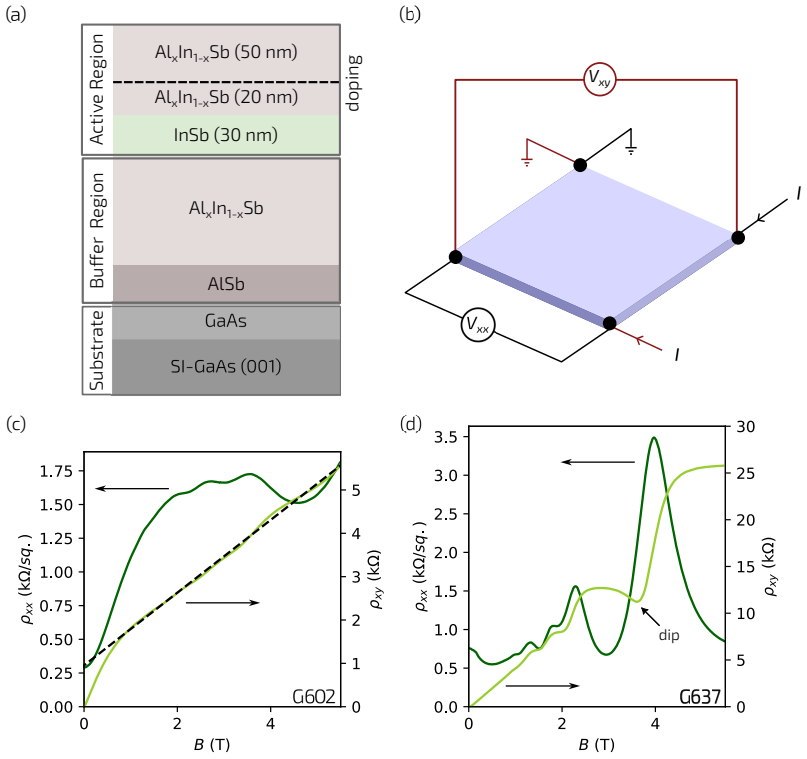

Figure 2.1: (a) Standard (deep) QW heterostructure with modulation δ-doping. The heterostructure is composed of a SI-GaAs substrate with an epitaxial GaAs smoothing layer followed by a buffer structure composed of an AlSb first intermediate (nucleation) buffer and a single composition AlInSb second intermediate buffer. The active region includes the InSb QW and an AlInSb upper barrier. Modulation δ-doping is introduced in the upper barrier at a distance of 20 nm from the quantum well. (b) Illustration of a VDP sample depicting two measurement configurations used non-simultaneously. The longitudinal resistivity (black) is measured with current and voltage probes oriented parallel to each other. The transverse Hall resistivity (red) is measured with the current and voltage probes oriented perpendicular to each other. The SdH oscillations in longitudinal resistivity and the IQHE of wafers (c) G602 and (d) G637 are plotted with arrows indicating the dual axes. G602 exhibits the typical characteristics of "major" parallel conduction and G637 exhibits characteristics of "minor" parallel conduction. In the event of no parallel conduction, the minima of the SdH oscillations would hit zero resistivity at magnetic fields corresponding to plateaus in the IQHE. The dip denoted in the quantum Hall data is characteristic of measurements in the VDP geometry.

1.5×10^{12} cm^{-2}, and 2×10^{12} cm^{-2}, as summarized in Table 2.2. Measurement of G617 with $N_d = 1\times10^{12}$ cm^{-2} revealed the sample did not conduct, indicating an insufficient amount of doping to populate a conducting channel. Alternatively, magnetotransport measurements of G602 with $N_d = 2\times10^{12}$ cm^{-2} in Figure 2.1c confirmed the doping was sufficient enough to populate a 2DEG as well as a parasitic channel of conduction. Clear indication of parallel conduction is the nonlinear behavior of R_{xy} which lowers the Hall plateaus from their expected quantized values dictated by filling factor. Also observed in this figure is a steep rising background resistance in ρ_{xx} from parallel conduction upon which small oscillations from a 2DEG are observed [102, 41]. Since voltages are the quantity experimentally measured, we must consider that the total series resistance is finite even when $R = 0$ for the 2DEG channel and a small current will pass through the parallel channel leading to the obvservation of a background resistance in the SdH oscillations.

As reported in Table 2.2, the quantum well density determined from the Shubnikov de Haas oscillations is 2.3×10^{11} cm^{-2}. as shown in Figure 2.1c, the total carrier density is determined from the slope of the high field Hall resistance, bisecting quantum Hall plateaus where they exist. The resulting density determined from the slope by $\rho_{xy} = B/(en_{tot})$ is 7.4×10^{11} cm^{-2} indicating a substantial carrier occupation of a parallel channel with density $n_{||} = n_{tot} - n_{2D}$ where n_{2D} is the 2DEG carrier density in the quantum well.

A near optimal doping density $N_d = 1.5\times10^{12}$ cm^{-2} was confirmed in G637 in Figure 2.1d where the Shubnikov de Haas oscillations and integer quantum Hall effect are characteristic of single channel conduction. The transverse resistance exhibits well-defined quantized quantum Hall plateaus $R_{xy} = h/\nu e^2$ at filling factors $\nu = hn_{2D}/eB = 1, 2, 3, 4$. The "dip" feature in the quantum Hall plateaus is a known artifact of the Van der Pauw geometry and should not be a cause for concern [117, 118]. It has been explained as a collapse and reconstruction of incompressible stripes by screening theory of the quantized Hall effect [43]. The absence of dips in measurements of narrow Hall bar samples supports this explanation [76].

In the longitudinal resistance, the population of a single subband is evidenced by the observation of single frequency Shubnikov de Haas oscillations. The oscillations, however, are not vanishing ($\rho_{xx} = 0$) and are instead lifted from zero at integer filling factors indicating some parallel conduction. The 2DEG density determined from the periodicity of Shubnikov de Haas oscillations versus inverse field and the total density determined from the Hall effect are 1.6×10^{11} cm^{-2} and 1.8×10^{11} cm^{-2} respectively. Therefore I estimate a parallel occupied channel with $n_{||} = 0.2\times10^{11}$ cm^{-2}. Having spanned the doping range from non-conductive to parallel conducting, the optimal doping density lies within the range $1.0\times10^{12} < N_d < 1.5\times10^{12}$ cm^{-2}. As will be discussed in the following sections, this ideal doping density is highly sensitive to the specifics of the growth. To

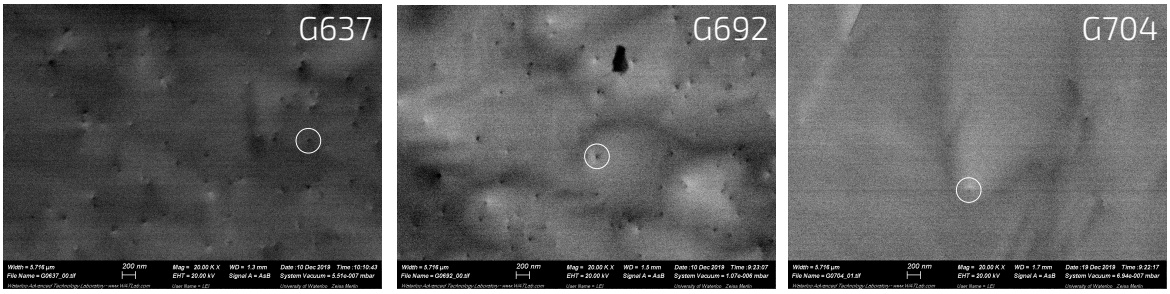

Figure 2.2: The characterization of TDD using scanning electron microscopy-electron channeling contrast imaging (SEM-ECCI) for wafers G637, G692, and G704 as indicated in the figure. White circles indicate a representative threading dislocation defect at the surface of each wafer. Details of the heterostructures are given in Table 2.3. Images and TDD characterization performed by Yinqiu Shi.

study the influence of various parameter changes in the growth, G637 was chosen as the control structure.

2.2.2 Influence of the buffer layers

Sample ID	buffer	μ (cm^2/Vs)	n_{2D} (cm^{-2})	$n_{\|\|}$	TDD (cm^{-2})
G637	A+S	5.3×10^4	1.66×10^{11}	Minor	4.5×10^8
G692	G+S	5.1×10^4	2.3×10^{11}	Major	$\sim 4.5 \times 10^8$
G704	A+I	9.3×10^4	2.0×10^{11}	Major	1.5×10^8

Table 2.3: Comparision of InSb QW growths with different buffers. G692 deviates from the control (G637) by a GaSb nucleation buffer only (G) and is combined with a single composition buffer (S). G704 deviates from the control by an AlSb nucleation buffer (A) and an interlayer buffer (I). The mobility, carrier density and parallel conduction of all samples were determined at 1.6 K. Threading dislocation densities (TDD) provided by Yinqiu Shi were characterized using scanning electron microscopy-electron channeling contrast imaging [115].

The influence of buffer layer design on the transport properties was tested by varying the nucleation buffer and the second-stage buffer. In G692 the 100 nm AlSb first intermediate buffer of the control (G637) structure was replaced by a 600 nm GaSb layer. In G704 the 4 μm single composition buffer of the control (G637) was changed to an inter-

layer buffer consisting of four repetitions of $Al_{0.1}In_{0.9}Sb/Al_{0.2}In_{0.8}Sb$ interlayers. Interlayer buffers have been shown to be more effective at eliminating propagating defects than thick single composition buffers [86]. Figure 2.2 depicts the surface of the control (G637) with AlSb first and single composition second intermediate buffers, G692 with GaSb first and single composition second intermediate buffers, and G704 with AlSb first and interlayer second intermediate buffers. As shown, the interlayer structure substantially reduced the density of threading dislocations at the surface. Though GaSb nucleation layers were shown to have lower threading dislocation densities at the buffer surface than AlSb layers, this change did not persist to the surface of the active region; the surface of G692 had comparable dislocation densities as the control (G637). Dislocation density in G704 with the interlayer buffer was reduced by a factor of 3 and is reflected in the improved sample mobility compared to G692. The carrier density and mobility of these growths are summarized in Table 2.3. In either case, the act of changing the buffer led to parallel conducting magneto-transport behavior despite all other parameters remaining equivalent to the control (G637). Though it was reported that interlayer buffers reduce parallel conduction, it has also been shown that single composition $Al_{0.1}In_{0.9}Sb$ buffers are sufficient. Given our results, we conclude that the role of the buffer is, at least in our case, not directly related to the source of parallel conduction and return to single composition $Al_{0.1}In_{0.9}Sb$ buffers in the following sections to continue comparison to our control (G637).

2.2.3 Influence of growth temperature and V/III ratio

Lack of reproducibility in electron transport characteristics between nominally identical growths led to the hypothesis that sub-optimal growth conditions might be to blame. Towards this goal we grew wafers G729 and G730 to study the effect of substrate growth temperature on the transport behavior of the quantum well as summarized in Table 2.4. The substrate temperature during growth of the $Al_{0.1}In_{0.9}Sb$ buffer was reduced from 380 °C in the control (G637) to 350 °C in G730 and to 330 °C in G729. Additionally, the InSb QW active regions were all grown at slightly lower substrate temperatures. The designated temperatures for the control (G637), G730 and G729 were 420 °C, 380 °C, and 350 °C respectively.

The mobility and carrier concentration both increase as growth temperature decreases in G730 and G729. Furthermore, the magnetotransport behavior of both samples indicates obvious parallel conduction with parallel densities on the order of 1×10^{11} cm^{-2} which may be due to enhanced electron doping efficiency of Si atoms in the doping layer at lower growth temperatures. To test the delta-doping density, an additional growth G736 was grown with the same temperature conditions as G730 but with a reduced delta doping

Sample ID	T_s (° C)	V/III	μ (cm$^2/Vs$)	n_{2D} (cm^{-2})	$n_{\|\|}$
G637	420/380	1.5	5.3×10^4	1.66×10^{11}	Minor
G729	350/330	1.5	11.0×10^4	4.2×10^{11}	Major
G730	380/350	1.5	8.4×10^4	3.0×10^{11}	Major
G736*	380/350	1.5	7.8×10^4	3.7×10^{11}	Major
G721**	420/380	1.5	3.1×10^4	1.1×10^{11}	Major
G735	380/350	2	6.6×10^4	1.8×10^{11}	None
G742	380/350	2	5.9×10^4	1.9×10^{11}	Minor

Table 2.4: Comparison of InSb quantum well growths with different substrate temperatures T_s in the QW and buffer (QW/Buffer) and different V/III ratios. The mobility, carrier density, and parallel conduction of all samples were measured at 1.6 K. * indicates G736 was uniquely grown with a lower doping density of 1.2×10^{11} cm^{-2}. ** indicates that G721 was uniquely grown as a full 3" substrate. All others were grown on quarter 3" substrates.

density of 1.2×10^{12} cm^{-2} in hopes of recovering the low density transport behavior of the control (G637). The resulting carrier density of G736 increased from 3.0×10^{11} cm^{-2} in G730 to 3.7×10^{11} cm^{-2}. It is clear from these results that changes in temperature on the order of 10 °C can change the quantum well carrier density by 0.4×10^{11} cm^{-2}. For the systems studied here that are near percolation regime at 1.0×10^{11} cm^{-2} and have onset parallel conduction near 2×10^{11} cm^{-2}, this sensitivity to temperature is substantial.

As a more sensitive test of temperature dependence, a repeat of the control (G637) was grown on a full three inch substrate as opposed to a quarter three inch substrate as all other samples in this section. When switching substrate sizes, the substrate holder in the MBE is changed. The differences between the two holders as well as the difference in size between the two substrates can lead to differences in the heating environment during the growth despite nominally identical readings from MBE system thermometry. The carrier density and mobility of G721 from magentrotransport measurements are listed in Table 2.4. With a carriers density of 1.1×10^{11} cm^{-2}, G721 has a lower carrier density by 0.6×10^{11} cm^{-2} than the control (G637) despite both samples having the same growth recipe. Our data suggests that accurate monitoring of the growth temperature as well as a consistent heating environment is essential for reproducible growths of modulation doped InSb quantum well heterostructures.

The relationship between temperature and antimony overpressure was investigated by two repeated growths at low temperature with an increased V/III ratio of 2. The carrier density of the new growths, G735 and G742, in Table 2.4 were only slightly higher than the

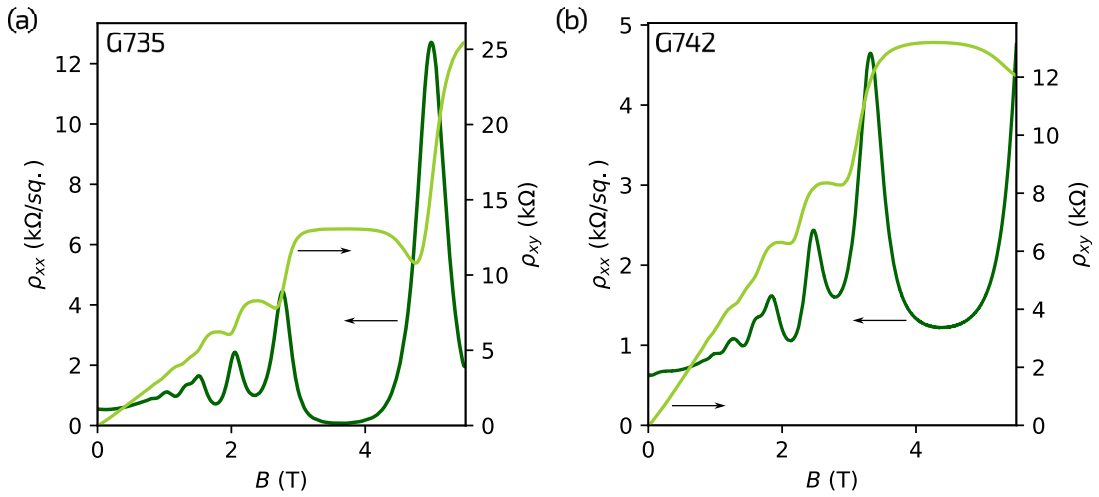

Figure 2.3: Magnetotransport behavior of (a) G735 and (b) G742 which were grown with nominally identical conditions. G735 exhibits no parallel conduction and G742 exhibits minor parallel conduction despite identical growth recipes. Arrows indicate axes for SdH oscillation and the IQHE. All data taken at 1.6 K.

control (G637) with 1.8×10^{11}, 1.9×10^{11}, and 1.7×10^{11}, respectively. This is in contrast to the high carrier densities of wafers G730 and G729, 3.0×10^{11} and 4.2×10^{11} cm^{-2}, respectively, which were grown at lower substrate temperatures but had the same antimony over-pressure of 1.5 as the control (G637). As shown in Figure 2.3, the magnetotransport data of both low temperature growths with increased antimony over-pressure resemble the behavior of the control (G637) with slightly higher carrier density. For example, we see the quantum Hall plateaus are positioned at slightly higher magnetic field values in this sample. Therefore, we do not see the start of the $\nu = 1$ plateau in this magnetic field range as we do for the control (G637) (fig. 2.1b). However, G735 has clear quantized quantum Hall plateaus up to $\nu = 1$ and vanishing longitudinal resistivity indicating clearly the absence of parallel conduction. This result shows that the increased Sb over-pressure eliminated parallel conduction without adversely lowering the number of carriers in the quantum well. Though the reason for this effect is still unknown, it has been suggested that the higher Sb flux compensates for undesirable extra free carriers in the material structure [115].

The second growth in this section, G742 which was grown with nominally identical conditions as G735, exhibited minor parallel conduction. As shown in Figure 2.3b, background conductance appears in the sample preventing the minima in the Shubnikov de Haas oscillations from reaching zero resistivity. Similar to the analysis used for the con-

trol (G637), the density of the parallel channel was determined from the difference in the total carrier density and quantum well carrier density. As expected, a parallel channel of density $n_{||} = 0.2 \times 10^{11}$ cm^{-2} is contributing in transport. Again, we observe that slight deviations between nominally identical growths can lead to irreproducibility in transport characteristics. However, we conclude that the source of parallel conduction that has so far plagued samples of this section, is greatly reduced by the incorporation of increased Sb overpressure in the growth.

2.2.4 Influence of alloy composition

So far it has been observed that there is a narrow acceptable doping range of $1.0 \times 10^{12} < N_d < 1.5 \times 10^{12}$ cm^{-2} for single channel conduction in our heterostructures, deviation from which can cause a complete lack of conduction or parasitic parallel conduction. The density of carriers is highly influenced by growth conditions independent of the intentional doping density N_d of the modulation doped layer during the growth. Furthermore, the deviations in conditions do not need to be intentional or substantial considering we observed that the transport of nominally identical growths can differ by parasitic conduction.

Sample ID	x	T_s (° C)	V/III	μ (cm^{-2}/Vs)	n_{2D} (cm^{-2})	$n_{||}$
G637	0.10/0.10	360/360	1.5	5.3×10^4	1.66×10^{11}	Minor
G746	0.12/0.09	380/350	2	9.8×10^4	2.5×10^{11}	Major
G747	0.11/0.11	380/350	2	8.5×10^4	2.8×10^{11}	Major

Table 2.5: Comparison of InSb quantum well growths with differing alloy composition in the buffer and/or barrier layers. G746 deviates from the control (G637) by a change to $x = 0.12$ ($x = 0.09$) in the buffer (barrier) and G747 by an increase in the barrier to $x = 0.11$. All samples were measured at 1.6 K.

In this section we investigate carrier density dependence on changes in aluminum composition of the buffer and barrier layers. It was found that the aluminum composition x can vary by $\pm 0.1\%$ between the target composition and the actual growth. Two structures were grown to test if changes in composition could explain the irreproducibility between wafers studied so far. The control (G637) and all other growths of this chapter had a target composition of $x = 10\%$ aluminum in the buffer and barrier layers. G746 and G747 were instead grown with $x = 9\%$ and $x = 11\%$ respectively in the barrier layers. G746 also included an increased aluminum composition of $x = 12\%$ in the 4 μm buffer, which increases the resistivity in the buffer. The results are summarized in Table 2.5. Apart

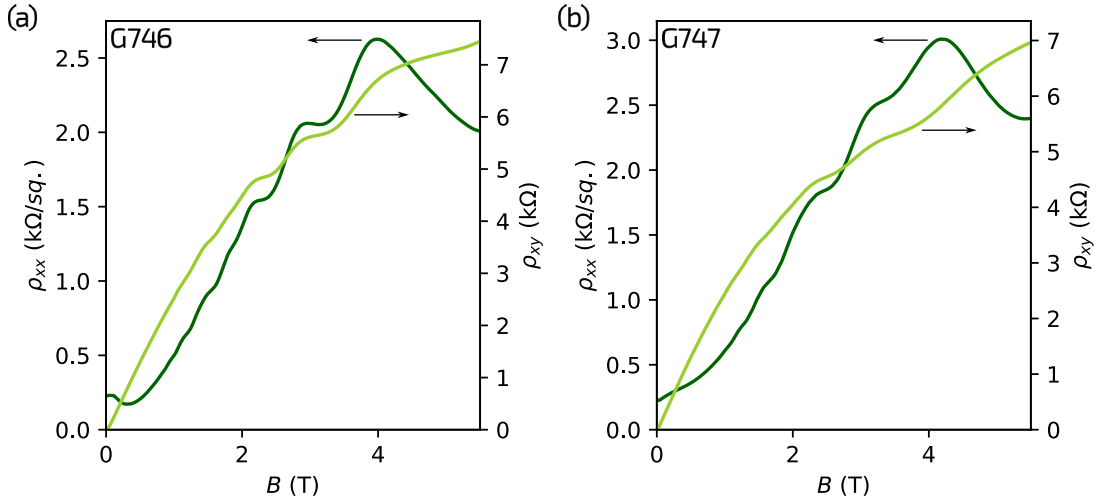

Figure 2.4: Magnetotransport behavior of (a) G746 and (b) G747 with differing alloy composition in the buffer and/or barrier layers. G746 deviates from the control (G637) by a change to $x = 0.12$ ($x = 0.09$) in the buffer (barrier) and G747 by an increase in the barrier to $x = 0.11$. Both exhibit major parallel conduction despite identical growth recipes. All data taken at 1.6 K.

from aluminum composition, both growths were grown with the same parameters as G735 which exhibited no parallel conduction. In contrast, G746 and G747 both exhibited parallel conduction as shown in Figure 2.4. The expectation of increasing the band gap in the region of modulation dopants is reduced sensitivity to parallel conduction by requiring a larger net charge of dopants to bend the band below the Fermi level; yet the parallel conduction is worse than similar growths (G735 and G742 from Figure 2.3a,b). Therefore is it unlikely that small 0.1% deviations in the aluminum target composition are responsible for the parallel conduction.

The study presented here on issues of reproducibility in modulation doped InSb quantum wells has revealed the interplay between several parameters in the heterostructure and in doing so emphasized the complexity of the InSb/AlInSb systems.

2.3 Top-gating

Field effect gating can be used alone or in combination with modulation doping to control the carrier density of a quantum well by shifting the Fermi energy level. In the standard

structures discussed so far, the modulation doped layer is closer to the surface of the growth than the quantum well. In a parallel conducting layer, any electric field from the surface will affect that layer more effectively than the quantum well density. The parallel conducting layer may also partially screen the electric field from the quantum well. A top-gated Hall bar device was fabricated in G742 to study the effect of gating on the parallel channel density $n_{||}$ and quantum well density n_{2D}. For reference to the gated structure, the as-grown electron densities of G742 were given in section 2.2.3 for a Van der Pauw sample. I fabricated the gated Hall bar using standard optical lithography and wet-etching techniques, keeping all processes at or below a temperature of 150 °C to prevent deterioration of device characteristics. The Hall bar was gated using a 30 nm thick hafnium dioxide dielectric deposited by atomic layer deposition at 150 °C and a Ti/Au global top-gate.

The carrier density and mobility of the gated Hall bar with no voltage on the top-gate, $V_g = 0$, was 2.3×10^{11} cm^{-2} and 160,000 cm^2/Vs. Inclusion of the gate-oxide at the surface of the growth increased the density of carriers in the structure as compared to the as-grown density in the VDP sample. As seen in the magnetotransport data of Figure 2.5a, increased background resistance in ρ_{xx} and nonlinearity in ρ_{xy} as compared to the VDP sample indicates that the gate dielectric enhanced the source of parallel conduction. Applying a gate voltage is however highly influential over the parasitic channel of conductance. Figure 2.5 shows the magnetotransport data of G742 at $V_g = -300$ mV achieves single channel conduction. The background resistance is greatly reduced with pronounced oscillations appearing in ρ_{xx} and reaching vanishing resistance at magnetic fields corresponding to $\nu = 2$. The inset of 2.5b shows a pinch-off curve in a two-terminal conductance measurement indicating that we can successfully deplete the parallel conduction channel as well as the quantum well. The pinch-off curves are stable and reproducible, overlapping when V_g is swept in the same direction and showing minimal hysteresis when V_g is swept in opposite directions. The dependence of the carrier density as a function of gate voltage is shown in Figure 2.5c. Two regions of differing slope are indicated by shaded regions in the plot. The gate voltage where the slope changes corresponds to depletion of parallel channels at low densities as observed in the magnetotransport behavior. Our ability to deplete the parallel channel before depletion of the 2DEG by a top-gate, is consistent with the parallel channel residing closer to the top-gate than the 2DEG. We therefore conclude that the source of parallel conduction in this growth is the delta-doped layer.

The dependence of the transport mobility μ on quantum well density is shown in Figure 2.5d and also includes shading to mark the density range corresponding to parallel conduction in Figure 2.5c. The mobility increases in both directions about the density corresponding to occupation of the parallel channel. In the parallel conducting (shaded)

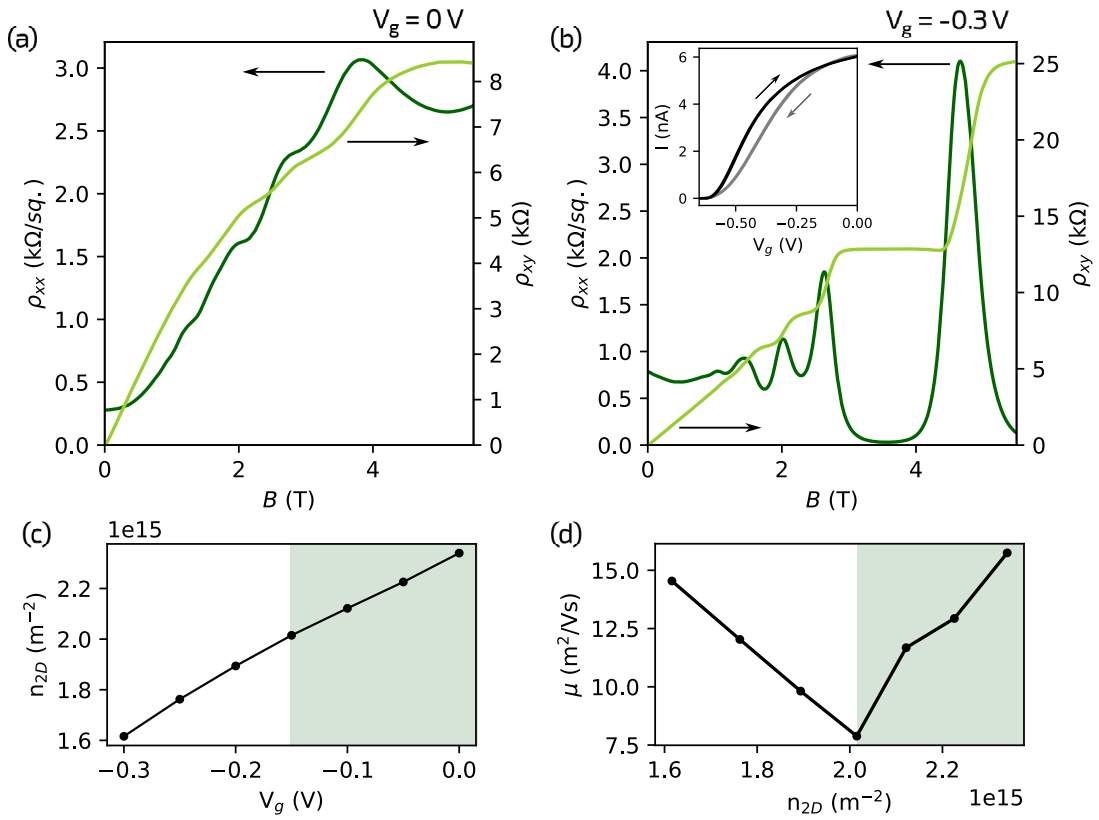

Figure 2.5: Top gated Hall bar geometry. SdH oscillations and the quantum Hall effect at $T = 1.6$ K for G742 at (a) $V_g = 0$ V and (b) $V_g = -0.3$ V. (inset) Two-terminal pinchoff curves exhibiting quality of the top gate. Characterisitc changes in the SdH oscillations and QHE indicate a change from parallel conduction to single subband occupation as a function of the gate voltage. The voltage and density range corresponding to occupation of a second subband, is indicated by a shaded region in figure (c) the 2DEG density versus gate voltage and (d) the mobility versus 2DEG density.

region, mobility increases as the parallel channel gains carriers which electrically screen the ionized atoms of the silicon dopants thereby reducing remote ionized impurity scattering in the quantum well [98, 99]. At lower density (unshaded), where only the quantum well is occupied, increased interface roughness scattering with increasing density occurs as the wave-function is pulled closer to the wafer surface. The top-side single side doping used in this heterostructure means the wavefunction will preferentially reside nearer the top interface of the quantum well due to band bending. As the 2DEG is depleted via a negative gate voltage, the band structure will tilt in the opposite direction as the electric field induced by modulation doping and the wavefuction will move away from this interface towards the center of the well where reduced interface roughness scattering improves mobility at low densities.

Apart from the initial calibration of delta-doping density, all growths were grown with a doping density of 1.5×10^{12}. We've shown that nominally identical growths can differ by the occupation of a parallel conduction channel. We have therefore observed that the window of modulation δ-doping density in AlInSb/InSb quantum well heterostructures for single channel conduction is smaller than the observed deviation in calibrated doping density between growths. This explains the prevalence of reports on AlInSb/InSb quantum wells with parallel conduction. Though we were able to deplete the parallel channel in this structure using a top-gate, this would not be the case in our pursuit of surface quantum wells where the delta-doping would have to reside beneath the quantum well. In these "inverted" structures an opposite relationship with the top-gate would occur, where the 2DEG would pinch-off before the parallel channel. Therefore the inability to reproduce a desired delta-doping density is a substantial problem. In the next section, we propose a solution to this problem: back-gates.

2.4 Back-gate structures

Challenges associated with modulation doping, studied extensively in the preceding sections, inspired the decision to explore the possibility of back-gating in InSb heterostructures. With no previous reports in InSb, we chose three different back-gate designs which considered the quality of the growth as well as the outlook for successful fabrication of devices. Structures chosen are presented in Figure 2.6. A properly structured back-gate must behave like a metal, be electrically isolated from the active region, and balance coupling between layers (required voltages to gate effectively) with breakdown voltage of the dielectric layer. Furthermore, a reliable contact fabrication method is required for operation of devices. An n-AlInSb layer was studied for ease of electrical contact with established fab-

rication processes for InSb quantum well heterostructures but was ultimately unsuccessful due to poor electrical isolation. Taking advantage of the GaAs substrates already incorporated in our heterostructure design and established literature on GaAs back-gates in GaAs quantum wells, additional designs included a n-GaAs epitaxial layer and an n-GaAs substrate. Unfortunately traditional methods of contacting n-GaAs requires high temperature annealing not compatible with the thermal budget of InSb heterostructures. A survey of attempted low-temperature fabrication processes for contacting GaAs at cryogenic temperatures is presented given a lack of literature on this topic. This work is ongoing.

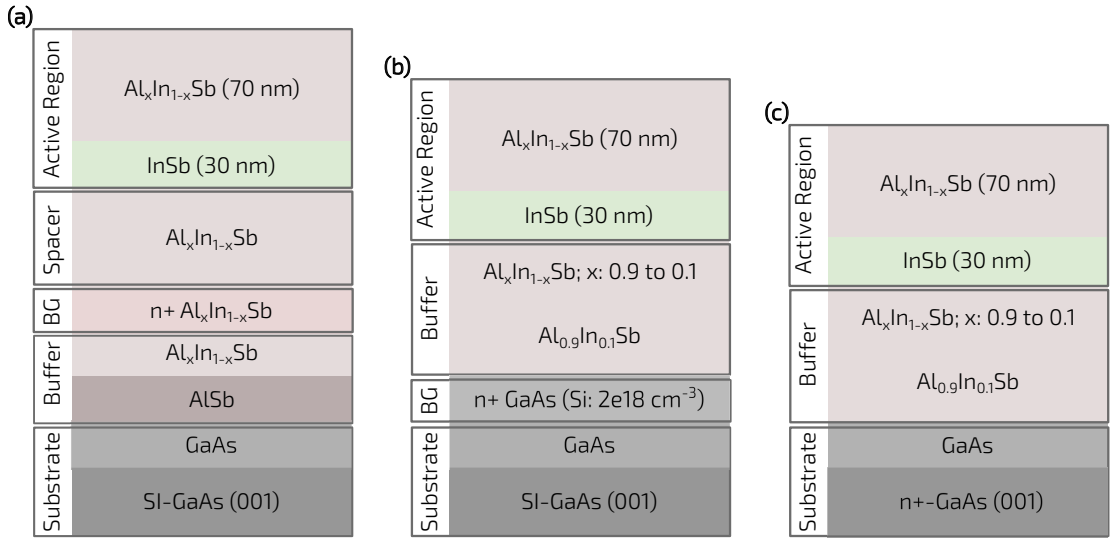

Figure 2.6: Standard quantum well heterostructure with a back gate composed of (a) a 50 nm degenerately doped AlInSb layer separated from the active region by a single composition AlInSb barrier, (b) a 500 nm degenerately doped GaAs layer separated from the quantum well by a single composition buffer of $x = 0.9$ and a linearly graded AlInSb buffer down to $x = 0.1$, and (c) an n+ GaAs substrate separated from the active region by the same buffer as in (b).

2.4.1 AlInSb back-gating

The first back gate design was chosen to minimize changes in the heterostructure that was studied extensively in the preceding section. We exchanged silicon modulation doping for a degenerately bulk doped AlInSb layer beneath the quantum well. This structure was thought to be ideal for fabrication of devices since we observed little trouble in making

electrical contact to modulation doping in previous structures. The structure, depicted in Figure 2.6a, places the back-gate on top of the current single composition AlInSb buffer and is separated from the active region by an additional AlInSb spacer layer of thickness t_{bs}.

Three growths G787, G797, and G817 were used to test isolation of the back-gate for various doping densities. Results are summarized in Table 2.6. In G787 the back-gate was severely shorted to the quantum well with <10 Ω of resistance. To improve isolation, the back-gate spacer was increased from 500 nm to 1 μm in G797 and G817. Additionally, the doping was decreased to 5×10^{18} cm^{-3} in G797 and further to 5×10^{17} cm^{-3} in G817. Though isolation resistance was improving, the 2DEG remained severely shorted to the back-gate with a maximally achieved resistance of 114 Ω at a doping density of 5×10^{17} cm^{-3}. Reducing doping by another order of magnitude would cross a threshold where flux becomes difficult to monitor in the MBE system. The persisting leakage between the back-gate and quantum well is not well understood but signifies the conduction band offsets are too small. Significant segregation of silicon from the degenerately doped layer was suspected but ruled out by secondary ion mass spectrometry. The behavior of doped AlInSb is examined further in the next chapter.

Growth	x	t_{bs} (μm)	N_d (cm^{-3})	ρ_{BG} (Ω/sq.)	d_{BG} (nm)	R_{QW-BG} (Ω)
G787	0.10	0.5	2e19	74 (4T)	50	< 10
G797	0.12	1.0	5e18	58 (4T)	50	30
G817	0.12	1.0	5e17	4000 (2T)	50	114

Table 2.6: n-AlInSb back-gates. Three back-gate growths with aluminum composition x, back-gate spacer thickness t_{bs}, bulk-doping density N_d, back-gate resistivity ρ_{BG}, and isolation resistance between the QW and back gate R_{QW-BG} are summarized.

2.4.2 n+ GaAs back-gating

Given InSb heterostructures are commonly grown on GaAs substrates and GaAs back-gates are more widely implemented, we studied two styles of GaAs back-gates. The first style included a 500 nm n+ GaAs layer that was grown immediately following the GaAs substrate smoothing layer and the second style used a n+ GaAs substrate. The first style was chosen to avoid switching substrates which can cause changes in temperature control and heat distribution during growth requiring significant changes in the current growth procedures.

Growth	t_{bs1} (μm)	t_{bs2} (μm)	N_d (cm^{-3})	d_{BG} (nm)	V_{leak} (Ω)
G851	0.1	2	2e18	500	13V
G915	0.6	1.5	2e18	500	16V
G975	0.6	1.5	N/A	substrate	12V

Table 2.7: GaAs back-gates. Parameters of three growths with single composition buffer thickness t_{bs1}, linearly graded buffer thickness t_{bs2}, doping density N_d, doping layer thickness d_{BG} and maximum voltage prior to observation of leakage current V_{leak} are summarized.

Growths G851, 915 and G975 incorporated n-GaAs back-gates and are summarized in Table 2.7. Previous challenges with growing sufficiently insulating buffers motivated redesigning the buffer to prevent leakage. The new buffers are composed of a single composition $Al_xIn_{1-x}Sb$ buffer with a large alloy composition $x = 0.9$ of thickness t_{bs1} followed by a linearly graded $Al_xIn_{1-x}Sb$ buffer of thickness t_{bs2} with alloy concentration ranging from $x = 0.9$ to $x = 0.1$ at the boundary of the active region to maintain crystal quality in the active region. All three growths were electrically isolated from the quantum well up to a gate voltage of 14 V on average. As shown in the next section, difficulty in reliably contacting the n-GaAs layer without annealing ultimately motivated the use of n-GaAs substrates over an epitaxial layer as a back-gate.

2.4.3 Low temperature contacts to n+ GaAs

Low resistance, Ohmic contacts to n-GaAs are generally achieved through contact structures requiring high temperature annealing, readily exceeding the thermal budget of InSb heterostructures. The conventional Au/Ge/n-GaAs contact structure principally relies on the alloying of Au:Ge at temperatures exceeding the Au:Ge eutectic temperature of 361°C but produces reliable Ohmic contacts at cryogenic temperatures. The Ge/Pd/n-GaAs contact structure alternatively relies on the process of solid phase regrowth that produces low resistance contacts for annealing temperatures as low as 250-350°C but depends sensitively on material thickness, especially at cryogenic temperatures where excess germanium will become highly resistive. The problem of excess Germanium is however most prevalent when annealed closer to the low end (250°C) of the annealing temperature range. Through a process of Au:Ge indiffusion that occurs near 175°C, a modified Au/Ge/Pd/n-GaAs contact structure has been shown to produce low resistance contacts at annealing temperatures below 200°C. Contact resistance measurements of this structure annealed below 200°C have, however, only been reported at room temperature.

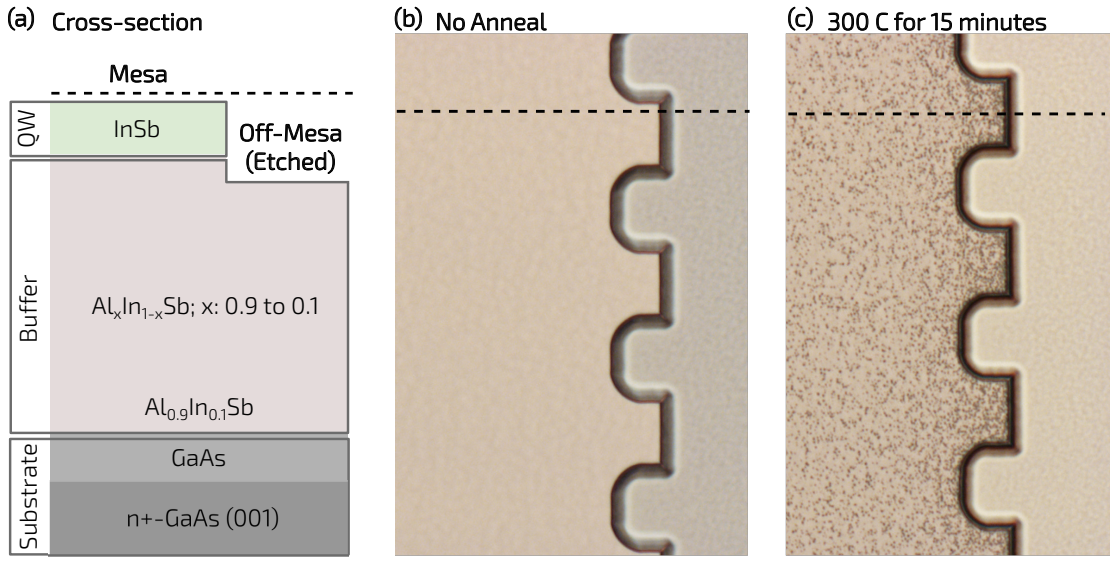

Figure 2.7: Annealing InSb heterostructures. (a) Cross-sectional schematic of the etch profile pictured from above in (b) and (c) illustrating that the mess etch is terminated in the buffer. An optical image of the as-grown surface of the mesa is shown in (b) prior to annealing. In (c) the InSb quantum well surface is visibly damaged post a 300 °C anneal for 15 minutes.

In the following, I demonstrate the effectiveness of low temperature annealing on various contact schemes to the silicon-doped n-GaAs back-gates of the previous section (G915 and G975). Contacts were deposited on the different samples listed in Tables 2.8 - 2.12 using an electron beam evaporator at pressures near 2×10^{-6} Torr during deposition. Prior to deposition, the native surface oxide was removed in Buffered Oxide Etchant (BOE) (1:10) for 10 seconds followed by a rinse in deionized water and blow-dry with nitrogen. Samples were quickly loaded into the evaporation chamber, spending less than 5 minutes in air. To remove any subsequent oxide regrowth from exposure to air, the samples were ion-milled in-situ prior to deposition. Deposition thicknesses were varied as part of the study and are reported where relevant. Following deposition, contacts were annealed in an oven under a mild vacuum for temperatures below 300 °C and in a rapid thermal annealing system for higher temperatures, the details of which are provided in the respective tables. Both the temperature and time of the anneals were varied to determine an adequate thermal dose for low resistance contacts which were assessed using two terminal resistance measurements.

500 nm n+ GaAs back-gate

Test	Anneal T (C)	Anneal Time (Hr)	R_C	T (K)
1	154	1	$>$ GΩ	1.5
1	154	3	70 MΩ	1.5
2	180	3	10 MΩ	1.5

Table 2.8: Ni/Ge/Au contacts of thicknesses 10/60/120 on G851

Two styles of the Ge/Pd/n-GaAs contact system based on a solid-phase regrowth principle were examined. An annealing temperature of 250 °C lends this system more favorably towards adaptation to lower temperatures than the Au/Ge/Ni/n-GaAs system. As summarized in Table 2.9, the contact resistances of Pd/Ge/Pd contacts of thickness 25/100/25 nm were measured at annealing temperatures spanning 154 - 300°C with annealing times ranging from 15 minutes to 48 hours. The palladium capping layer was incorporated to improve wire-bonding of devices. Below an annealing temperature of 160°C samples remained highly resistive at room temperature with 2 MΩ of resistance persisting after 48 hours of annealing. These samples were therefore not measured at cryogenic temperatures. For all other samples in Table 2.9, the specific contact resistivities at 1.5 K are given. As a control sample, a 15 minute anneal at 300°C in a rapid thermal annealer was conducted to confirm typical Ohmic contact formation and yielded a contact resistance of 300 Ω. As

Test	Anneal T (C)	Anneal Time (Hr)	R_C	T (K)
1	154	36	$>$ 10 MΩ	RT
1	154	48	$>$ 2 MΩ	RT
2	162	12	$>$ GΩ	1.5
2	162	24	20-160 KΩ	1.5
3	180	12	7-50 MΩ	1.5
4	200	1.3	$>$ GΩ	1.5
4	200	4.3	$<$ 3500 Ω	1.5
4	200	12	$<$ 3500 Ω	1.5
5	300	0.25	$<$ 300 Ω	1.5

Table 2.9: Pd/Ge/Pd contacts of thicknesses 25/100/25 on G851

Test	Anneal T (C)	Anneal Time (Hr)	R_C	T (K)
1	162	12	7 MΩ	RT
1	162	24	3 MΩ	RT
2	200	4	140 kΩ	RT

Table 2.10: Pd/Ge/Pd contacts of thicknesses 7/50/20 on G851

presented in Figure 2.7, this annealing temperature is however outside the thermal budge of our InSb heterostructures and is therefore not useful outside of this context.

Test	Anneal T (C)	Anneal Time (Hr)	R_C	T (K)
1	157	15	2MΩ	RT
1	157	40	10-80 KΩ	RT
2	175	1	5 MΩ	RT
2	175	4	0.25-1.5 MΩ	RT
3	183	19	0.7 kΩ	RT
3	183	19	70 kΩ	77
3	183	38	1 kΩ	RT
3	183	38	0.5 MΩ	77

Table 2.11: Pd/Ge/Au contacts of thicknesses 10/50/120 nm on G915

Discounting the control sample at 300 °C, we observed that the lowest resistivities were

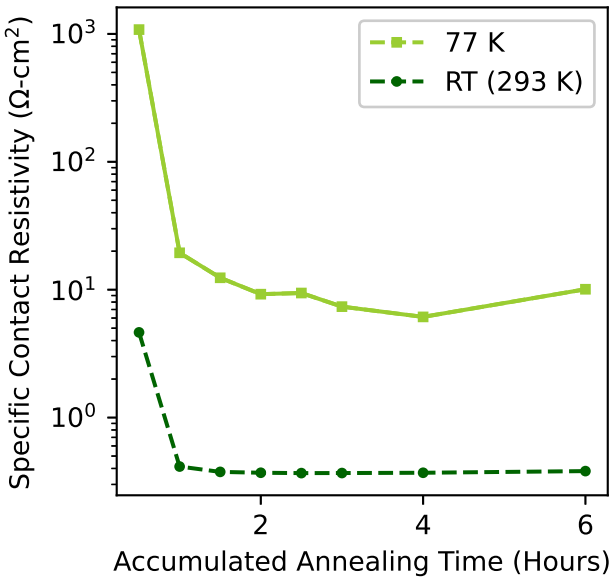

Figure 2.8: The relationship between contact resistivity and cumulative annealing time at 200°C of Au/Ge/Pd/n-GaAs contacts. Resistance measurements were conducted at room temperature and 77 K.

obtained at 200°C for annealing times longer than 4 hours (confirmed up to 12 hours total). We also observed that contacts on the order of 10 kΩ could be achieved near 160°C but required a anneal of 24 hours. We suspected that excess Germanium might be causing unnecessarily long annealing times at low temperatures. The solid phase regrowth process is a kinetics controlled process which means that thicker layers will require relatively longer anneals or higher temperatures to reach completion. These two temperatures were tested in a second batch of samples with thinner contacts of 7/50/20 nm aimed at reducing the required annealing times. The anneal parameters and contact resistances are summarized in Table 2.10 but the contact resistances were not improved and are reported solely at room temperature.

We explore next the Au/Ge/Pd/n-GaAs system which was shown to exhibit Ohmic behavior (at room temperature) for annealing temperatures as low as 160°C [133, 46]. The contact resistivities of Au/Ge/Pd contacts of thickness 10/50/120nm on G915 are given in Table 2.11 for anneals below 200°C. Compared to the literature, I observed room temperature contact resistances >MΩ for temperatures below 200°C unless annealed for far longer than a couple hours. The relationship between contact resistivity and cumulative anneal-

ing time for 200°C is plotted in Figure 2.8 for resistance measurements conducted at room temperature and 77 K. Low resistances (∼1 kΩ) were measured at room temperature for ≥1 hour of annealing at 200°C. However, the contact resistance increases with decreasing measurement temperature and reaches ∼40 kΩ at 77 K.

Ohmic contacts to n+ GaAs substrates

Disagreement of contact resistance at room temperature with previous reports, is likely due to differences in base deposition pressure. Contacts resistivites on the order of 10×10^{-6} Ω·cm^2 were achieved for deposition pressures on the order of 1×10^{-8} Torr [136]. To confirm the role of base deposition pressure I fabricated two samples on an n+ GaAs substrate (G303), G303-1 and G303-2, where the base-pressure of the deposition chamber was the only intentional difference. Deposition of Au/Ge/Pd contacts on sample G303-2 was conducted at a pressure of 3×10^{-6} Torr, the minimum required deposition pressure as per standard operating procedures. Deposition of G303-1 was run at a base pressure of (4×10^{-7}) Torr which requires a 10 hour pump to reach the minimum base pressure of the deposition chamber. As summarized in Table 2.12, sample G303-1 was annealed at 200° for 30 min, 1 hr, and 2 hr cumulative annealing times. Sample G303-2 was also annealed at 200° for 30 min for comparison to G303-1. The contact resistance at base pressure is improved by an order of magnitude.

Test	Anneal T (C)	Anneal Time (min)	R_C (Ω cm^2)	T (K)
1	0	0	22	RT
1	0	0	8100	77
1	0	0	47000	1.6
1	200	30	810	1.6
1	200	60	400	1.6
1	200	120	110	1.6
2	200	30	4.5	RT
2	200	30	860	1.6

Table 2.12: Contact resistance of Pd/Ge/Au contacts of thicknesses 10/50/120 nm deposited on the back of an n+ GaAs substrate. The contact deposition of G303-1 (G303-2) was carried out at a chamber pressure of 4×10^{-7} (3×10^{-6}) Torr. Contact resistance measurements were conducted at various measurement temperatures for different anneal temperatures and anneal times.

Clearly, the base deposition pressure was relevant but not the limiting factor in achieving low-resistance Ohmic contacts to n+ GaAs at cryogenic temperature. In this event, we again suspected the role of excess Germanium and proceeded with a final batch of devices with Pd only contacts. Figure 2.9 presents a 2-terminal IV measurement measured at 1.6 K that demonstrates the Ohmic behavior of our device with annealed Pd contacts. The contacts were annealed for 2 hours at 200°C yielding a total resistance of $2R_C + R_L + R_{GaAs} = 325\ \Omega$ where R_C is the contact resistance, R_L is the line resistance of the measurement circuit and R_{GaAs} is the resistance of the semiconducting region between contacts. From this measurement, an upper bound on our contact resistance is given by $R_C \sim 80\ \Omega$ - $R_{GaAs}/2$.

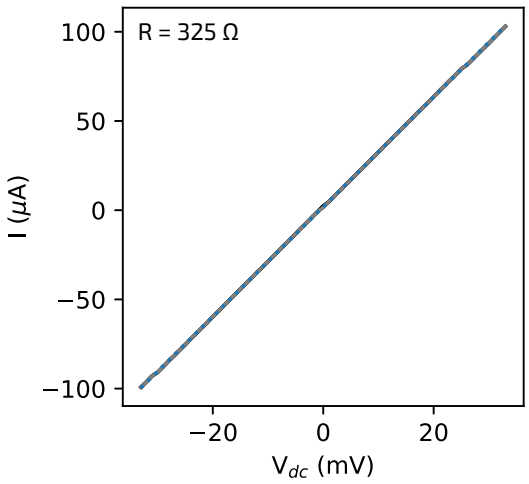

Figure 2.9: Two-terminal IV measurement of sample G303-3 with Pd only contacts annealed for 2 hours at 200°C. Data taken at T = 1.6 K.

In conclusion, we investigated the effect of doping density, growth parameters, and alloy composition on parallel conduction in modulation doped InSb standard QW heterostructures grown on GaAs substrates. Our results suggest that InSb heterostructures require precise tuning of modulation dopants to avoid parasitic parallel conduction, which is so precise that it is often beyond the ability to reproduce in MBE. Data from a top-gated Hall bar device highlighted the influence of the field effect on the total carrier density in a standard QW heterostructure. A sufficiently negative top-gate voltage is capable of depleting the parallel conducting channel from the modulation doping layer while maintaining a conductive quantum well. Looking towards surface quantum wells, where modulation doping must reside beneath the quantum well, the same method of top-gating would deplete the QW before the parallel channel and thus require a back-gate. We explored the growth of back-gated InSb QW heterostructures and tested common fabrication methods for low-temperature annealed contacts to n+ GaAs. Resistivities of such contacts have been reported only at room temperature and not at cryogenic temperatures which are of interest in this work. We achieve Ohmic Pd contacts to n+ GaAs substrates measured at T = 1.6 K which were annealed at 200°C for 2 hours. We believe that this chapter represents a necessary stepping stone in the pursuit of back-gated InSb heterostructures, applicable for high-density surface quantum well structures required for proximity superconducting devices.

Chapter 3

Field effect two-dimensional electron gases in modulation-doped InSb surface quantum wells

Confining potentials in electrostatically-defined nanoscale devices, such as single electron transistors or single electron pumps, are strongly enhanced in two-dimensional electron gases (2DEGs) hosted at the surface or near the surface of semiconductor heterostructures [15]. Furthermore, surface or near-surface quantum well (QW) heterostructures in III-V semiconductors are compatible with proximitized superconductivity and offer a scalable planar platform for superconductor-semiconductor systems, such as those suggested for topological quantum computation [110, 56] and those suitable for topological phase transitions involving Majorana zero modes [89, 72, 57]. Amongst III-V binary semiconductors, Indium Antimonide (InSb) has the smallest electron effective mass, highest spin orbit coupling [59, 58], and largest Landé g-factor. Such material properties makes the pursuit of InSb QWs desirable for a number of quantum device applications, including quantum sensing, quantum metrology, and quantum computing.

High quality two-dimensional electron gases (2DEGs) in InSb QWs are difficult to realize partly due to the highly mismatched lattice constants between the quantum well and barrier materials [73], the available purity of the required base elements (In, Sb) [1], and the lack of wafer-to-wafer reproducibility with doping schemes [74, 116]. InSb QWs have generally relied on the use of modulation-doping for 2DEG formation, but these structures have frequently reported issues with parasitic parallel conduction and unstable carrier densities [76, 100, 68, 77]. This is especially true of InSb surface QWs, which must

contend with a Schottky barrier at the surface. Dopant-free field-effect 2DEGs avoid these issues and have recently been reported in undoped InSb QWs [75]. However, as reported in GaAs systems, achieving good Ohmic contacts is challenging in completely undoped heterostructures, especially near the surface [88].

In this chapter, we report on the use of an n-InSb capping layer to promote the formation of reliable, low resistance Ohmic contacts to a surface InSb QW. We compare two InSb surface QW heterostructures, one with and one without a modulation-doped InAlSb layer, and demonstrate the influence of modulation doping on gating characteristics, magnetotransport behavior, and spin-orbit interaction. We overcome issues of parallel conduction in both heterostructures and present magnetotransport behavior of a high quality, single-subband 2DEG up to 18 T. The effective mass, transport and quantum lifetimes, and g-factor are determined from magnetoresistance measurements. The strength of spin-orbit interaction is characterized using weak anti-localization measurements.

3.1 Fabrication methods

Two wafers, G839 and G849, were grown by molecular beam epitaxy (MBE) by Yinqiu Shi. Wafer G839 had the following sequence of layers (see Figure 3.1), starting from a 3" semi-insulating (SI) GaAs (001) substrate: a 120 nm GaAs smoothing layer, 100 nm AlSb nucleation layer, a 4 µm $Al_{0.1}In_{0.9}Sb$ metamorphic filter buffer, a 25 nm InSb quantum well, and a 5 nm InSb cap layer doped with Si at a doping density of 2×10^{18} cm^{-3}. Wafer G849 is identical to wafer G839, except for an additional Si delta-doped layer (with sheet doping density 1.5×10^{11} cm^{-2}) located 10 nm below the InSb quantum well. In both wafers, the doped n-InSb cap layer facilitates the low-temperature formation of low-resistance Ohmic contacts to the 2DEG. The purpose of the delta-doped layer below the InSb quantum well in G849 is to pull the 2DEG wavefunction further away from the surface than in G839.

I fabricated eight gated Hall bars (see Table 3.1 and Figure 3.1) using optical lithography and wet-etching techniques, keeping all processes at or below a temperature of 150°C to prevent the deterioration of device characteristics [127, 138, 68], and preventing the InSb surface from coming into contact with photoresist developer. To begin processing, samples are cleaned prior to lithography by sonication in acetone and subsequently propanol for 5 minutes each before a final blow dry with nitrogen. Mesa regions are defined with optical lithography using Shipley S1811 photoresist. The resist is spun at 5000 rpm for 60 seconds and baked at 120 °C for 90 seconds. Following exposure, the photoresist is developed in MF319 developer for one minute. In order to ensure no unintentional thin film of photoresist remains in the exposed regions, samples are ashed in an oxygen plasma

Wafer G839		Wafer G849	
Hall bar ID	peak mobility (cm^2/Vs)	Hall bar ID	peak mobility (cm^2/Vs)
G839-1	18,000	G849-1	21,800
G839-2	22,200	G849-2	24,400
G839-3	21,200	G849-3	24,600
G839-4	23,100	G849-4	24,100

Table 3.1: Peak transport mobilities μ of all samples reported in this Chapter.

at 50 W for twenty seconds prior to wet etching to remove any residual photoresist in the exposed (off-mesa) regions. Wet etching proceeds with a ten second dip in buffered oxide etch (BOE) (1:10) to remove any native oxide on the surface of the sample caused by ashing and exposure to air. The mesa is etched with a solution of H_2O_2:H_3PO_4:$C_6H_8O_7$:H_2O mixed 3:4:9:44 by volume for approximately 30 seconds or until an etch depth of at least 100 nm has been reached. After etching, the photoresist etch mask is removed by sonication in acetone and isopropanol.

Optical lithography for definition of Ohmic contacts uses a bilayer resist recipe of MMA/Shipley. First the MMA (methyl methacrylate) is spun at 5000 rpm for 60 seconds and baked at 150 °C for 5 minutes. Next the Shipley is spun in the same manner with a bake at 120 °C for 90 seconds. Optical exposure and development of the sample in MF319 succesfully removes Shipley in regions where Ohmic contacts are to be formed. This exposure and development does not remove the MMA which protects the surface from being etched by the MF319 developer. MMA is subsequently removed by a fifteen minute exposure and development in a solution of isopropanol:H_2O at a 7:3 concentration. The now exposed surfaces are sulphur passivated in a solution of ammonium polysulfide $(NH_4)_2S_x$ for 20 minutes under illumination and at room temperature. Loading the sample into the deposition chamber proceeds immediately after passivation to minimize exposure to air. An angled 45° deposition of 20/60 nm of Ti/Au directly on the doped n-InSb layer is performed in a thermal evaporator. For the Ti/Au Ohmic contacts described here, the passivation is designed to etch away native oxides, prevent further surface oxidation during transfer in air to the deposition chamber, and possibly dope the surface [121, 71, 13]. Combined with the presence of Si dopants at the surface of the InSb quantum well, Ohmic contacts with an average resistance of less than 1 kΩ were achieved in zero magnetic field, and 12 kΩ at $B = 18$ T. Finally, the 60 nm thick HfO_2 dielectric layer which isolates the

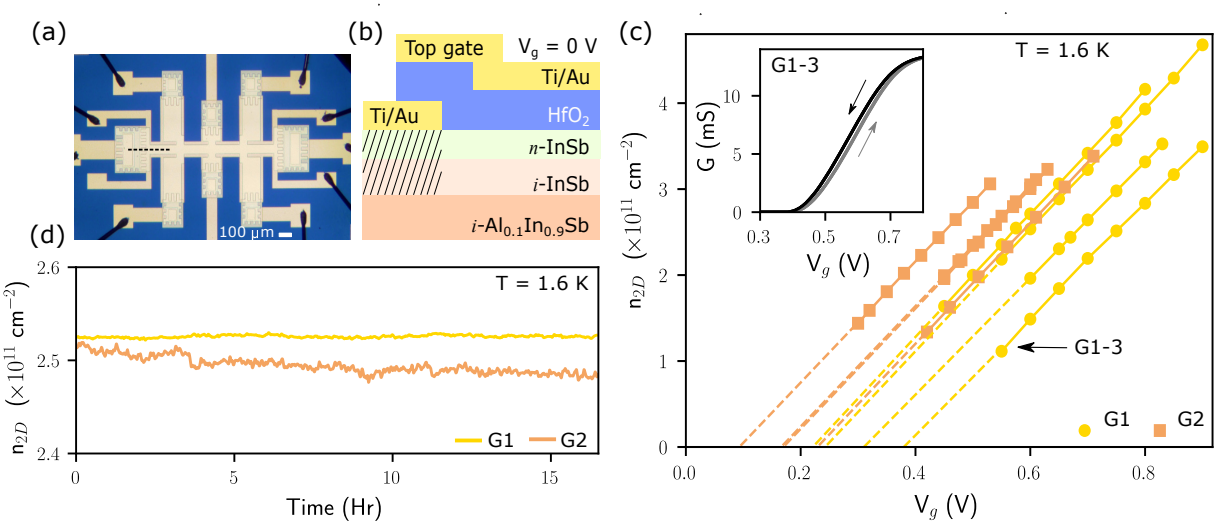

Figure 3.1: (a) Optical image of a representative gated Hall bar. The global top-gate overlaps the Ohmic contacts in order to induce a 2DEG between contacts. (b) Schematic of the cross section along the dotted line in (a). The 30 nm InSb quantum well is populated by electrons beneath Ti/Au Ohmic contacts (hashed region), unlike regions directly underneath HfO_2. (c) Hall density versus top-gate voltage of all eight Hall bars from G839 and G849. The 2DEG density increases linearly with V_g in all samples, and is reproducible along the linear traces. (inset) Two-terminal differential conductance $G(V_g) = dI/dV_{sd}$ (using 100 μV ac excitation) showing the turn-on voltage of a gated Hall bar on G839. Eight traces are shown, four while increasing V_g (grey) and four while decreasing V_g (black). (d) The Hall density in G839 remains stable for 16 hours, whereas it drifts with time in G849.

top gate from the quantum well and Ohmic contacts in a gated Hallbar is deposited using atomic layer deposition at 150 °C; the dielectric breakdown field is ∼1.5 MV/cm at $T = 1.6$ K. Following deposition, optical lithography with Shipley is used to define vias above the Ohmic contacts. The HfO_2 in the exposed vias is etched in BOE at a concentration of 1:10. Following etching, via resist is removed and processing proceeds with optical lithography of the top-gate and bond pads to metallic contacts. A bilayer of MMA/Shipley as discussed for the Ohmic contacts is again used and the Ti/Au (20/60 nm) top-gate and bond pads are similarly deposited in a thermal evaporator at an angle of 45°.

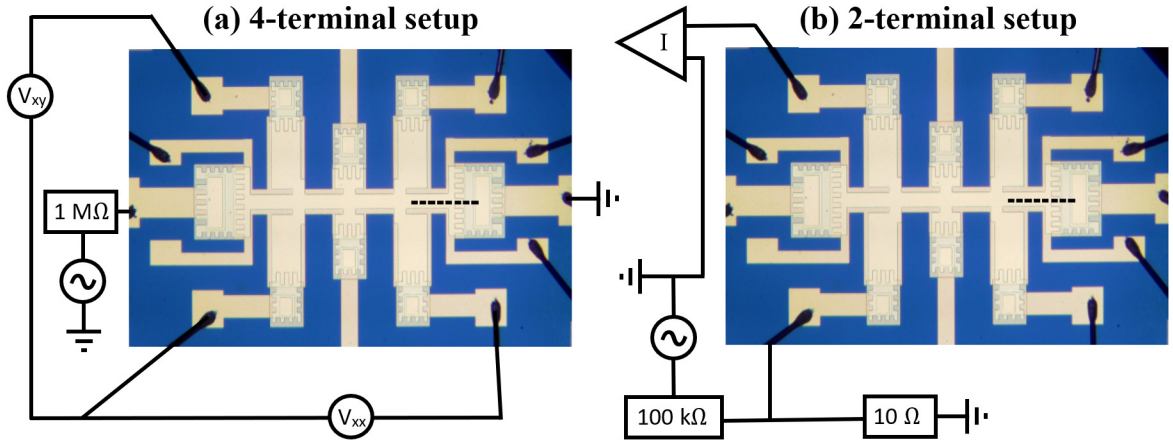

Figure 3.2: Electrical circuits for: (a) constant-current four-terminal setup with voltage preamplifiers (◯) for measuring V_{xx} and V_{xy}, and (b) constant-voltage two-terminal setup with a current preamplifier (▷) for measuring differential conductance $G = dI/dV$. The ac oscillator (∼) outputs a signal ranging from 10 mV to 1 Volt at low frequencies (10−20 Hz).

3.2 Characterization

Using standard ac lock-in measurement techniques, four-terminal and two-terminal transport experiments were performed in a pumped-^{4}He cryostat and a ^{3}He/^{4}He dilution refrigerator, with a base temperature of 1.6 K and 11 mK respectively. Figure 3.2 shows the electrical circuits used in experiments. The typical "constant" ac voltage excitation in 2-terminal measurements was 100 µV. The typical "constant" ac current in 4-terminal measurements was 100 nA for $T > 1.5$ K and 10 nA for $T < 100$ mK.

During Hall density and mobility constant-current 4-terminal measurements (Fig.3.1c and Fig. 3.3c), the carrier density n_{2D} was kept above 1×10^{11} cm^{-2} at all times. Otherwise, as the sample becomes more resistive, an increasingly significant fraction of the ac signal applied to the 1 MΩ resistor is dropped across the 2DEG. At pinch-off, the ac signal is entirely applied across the 2DEG rather than across the 1 MΩ resistor. Such voltages, which can be larger than the Fermi energy and even the confinement potential of the 2DEG in the InSb quantum well, can cause charging effects that last for the remainder of the cooldown (a thermal cycle to room temperature "resets" the device to its original characteristics).

3.2.1 Electrostatic gating

In ungated Hall bars, the as-grown electron densities of G839 and G849 were 3.0×10^{11} cm^{-2} and 3.5×10^{11} cm^{-2}, respectively. However, in all gated Hall bars, the quantum well in both wafers is completely depleted of electrons at top-gate voltage $V_g = 0$, most likely due to significant trapped charges associated with HfO_2 [138, 6]. A positive top-gate voltage is needed for a 2DEG to form. The 2DEG turn-on threshold voltage is the intercept of the electron density $n_{2D}(V_g)$ on the top-gate voltage axis in Figure 3.1c, obtained from the linear extrapolation of the data for each Hall bar to $n_{2D} = 0$. This definition removes any ambiguity in the turn-on threshold due to the transition from the Boltzmann transport regime to the percolation regime at low electron densities. The average 2DEG turn-on threshold is $V_g = (0.29 \pm 0.06)$ V for wafer G839 and $V_g = (0.17 \pm 0.05)$ V for wafer G849. The lower threshold in wafer G849 is consistent with the additional doping provided by its delta-doped layer, which brings the conduction band closer to the Fermi level in wafer G849 than in wafer G839.

The inset of Figure 3.1c shows a typical pinch-off curve for a gated Hall bar from wafer G839 in a two-terminal conductance measurement. Agreement between the pinch-off voltage ($V_g = 0.38$ V) from the two-terminal measurement and the extrapolated 2DEG turn-on threshold ($V_g = 0.38$ V) from the four-terminal measurement, both obtained from the same Hall bar, strongly indicates that there is no significant tunnel barrier within the Ohmic contacts themselves [37]. Indeed, the electron density in the InSb quantum well directly underneath the Ohmic contact metal should be the same as or very similar to the as-grown electron density, because the HfO_2 dielectric is not in direct contact with n-InSb (*i.e.*, there is not a large trapped charge density). The pinch-off curves are stable and reproducible, overlapping perfectly when V_g is swept in the same direction and showing minimal hysteresis when V_g is swept in opposite directions. After pinch-off, the 2DEG does not turn itself back on with time [75, 100, 77]. To further illustrate this time stability, Figure 3.1d shows the carrier density measured over a period of 16 hours, where it essentially stays constant. This is not however the case with devices from G849, where the electron density can drift with time. We speculate this could be due to the presence of dopants in the InAlSb layer. Indeed, quantum dots fabricated in InSb 2DEGs with modulation-doped InAlSb have recently been reported where device characteristics drift in time [100, 68].

3.2.2 Mobility and Density

Figure 3.3a shows the transverse (Hall) resistance R_{xy} and longitudinal resistivity ρ_{xx} in a magnetic field up to $B = 18$ T at the highest accessible carrier density 3.4×10^{11} cm^{-2}

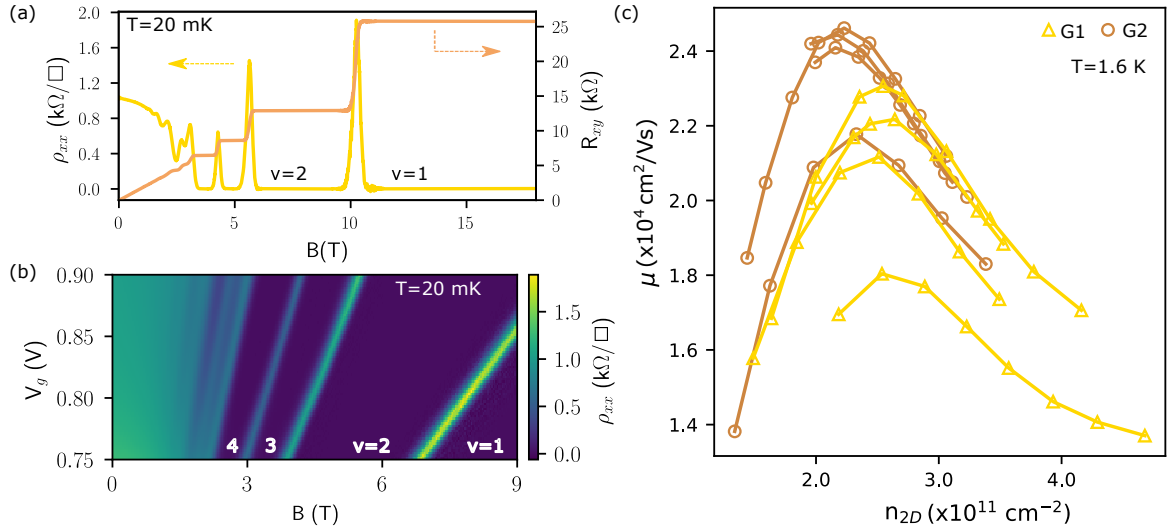

Figure 3.3: (a) Longitudinal resistivity ρ_{xx} and Hall resistance R_{xy} vs. magnetic field at $n_{2D} = 3.4{\times}10^{11}$ cm^{-2}. (b) Landau fan diagram. Integer quantum Hall states from $\nu = 1$ to 4 are labeled. (c) Mobility vs. Hall density of all Hall bars from G839 (triangles) and G849 (circle).

for sample G839-3. The transverse resistance exhibits well-defined quantized quantum Hall plateaus $R_{xy} = h/\nu e^2$ at filling factors $\nu = hn_{2D}/eB = 1, 2, 3$, and 4, where h is the Planck constant and e is the single electron charge. The population of a single subband is evidenced by the observation of single-frequency Shubnikov-de-Haas oscillations in combination with vanishing $\rho_{xx} = 0$ at $\nu = 1, 2, 3, 4$. Furthermore, the 2DEG density determined from the periodicity of Shubnikov-de-Haas oscillations versus inverse field, given by $n_{2D} = \frac{2e}{h}\left(\frac{1}{B_{\nu+1}} - \frac{1}{B_\nu}\right)^{-1}$, matches the total carrier density n_{tot} determined via the classical Hall effect $n_{tot} = B/eR_{xy}$. No signs of parallel conduction from either a second subband or another conductive layer is discernible. The absence of Landau level crossings in the Landau fan diagram shown in Figure 3.3b indicates the single subband behavior persists over the entire measured density range. The Landau fan, obtained by sweeping the top-gate at magnetic field increments on sample G839-3, showcases the reproducibility and stability of gating characteristics.

The dependence of the transport mobility μ on 2DEG density is shown in Figure 3.3c which shows an average peak mobility of $(2.1{\pm}0.2){\times}10^4$ cm^2/Vs near $n_{2D} = 2.5{\times}10^{11}$ cm^{-2}

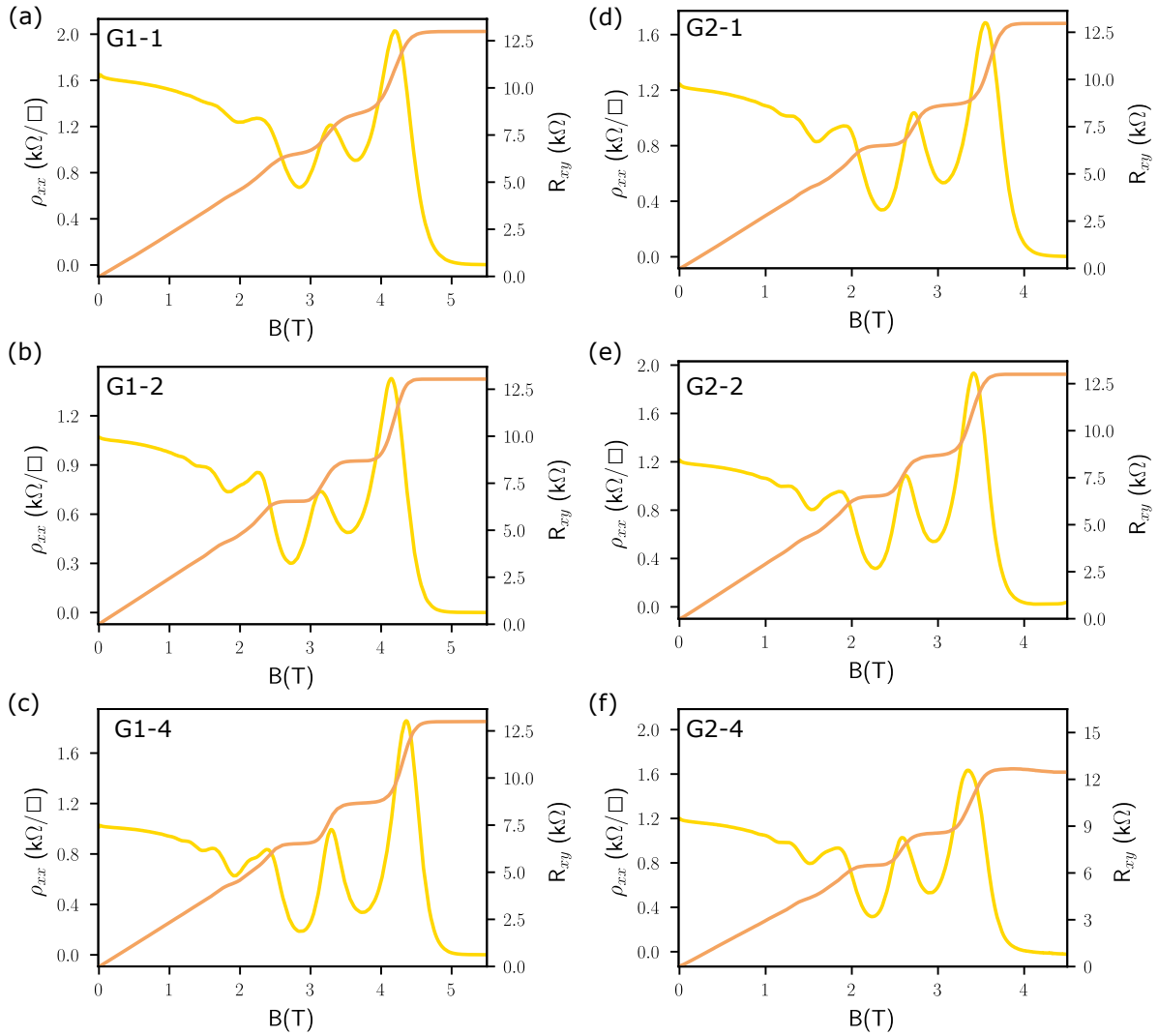

Figure 3.4: Longitudinal resistivity ρ_{xx} (yellow) and Hall resistance R_{xy} (orange) at 1.6 K of additional samples in G839 near 2.7×10^{11} cm^{-2} (a, b, c) and G849 near 2.2×10^{11} cm^{-2} (d, e, f). We observe the oscillation in ρ_{xx} corresponding to $\nu = 2$ hit zero resistance, indicating the absence of parasitic conduction. Furthermore, the absence of a second oscillation frequency in all figures is indicative of single-subband occupation.

in G839. The decrease in mobility at higher densities is attributed to increasing interface roughness scattering [3, 111] as the electron wavefunction is pulled closer to the surface by the increasing electric field of the top-gate. Increased scattering from a populating second subband is ruled out, since there is only one subband populated over that range of density. Alloy scattering (typically only observed in ternary alloys) is also ruled out, since the 2DEG wavefunction lies almost entirely within the InSb quantum well. The higher average peak mobility of $(2.4 \pm 0.1) \times 10^4$ cm^2/Vs near $n_{2D} = 2.2 \times 10^{11}$ cm^{-2} in G849 is consistent with its 2DEG being pulled further away from the surface by the delta-doped layer, relative to G839. The greater device-to-device reproducibility in G849 than in G839 is also consistent with this picture. Variability between nominally identical devices may be mostly due to surface treatment during sample fabrication. The mobilities reported here could perhaps be improved further [73] by reducing the density of threading dislocations [114, 113, 87] and hillocks [112, 18]. Magnetotransport data of additional Hallbar devices fabricated in G839 and G849 is provided in Figure 3.4. Magnetotransport characteristics between Hallbars are quite reproducible indicating the quality of growth and fabrication. Furthermore, as discussed in the earlier, there are no signs of parasitic parallel conduction or second subband occupation.

3.2.3 Effective mass

Figure 3.5a shows the temperature dependence of the amplitude of low-field SdH oscillations $\Delta\rho_{xx}$ in sample G849-4, obtained by subtracting a polynomial background from ρ_{xx}. The data was taken at a density of 3×10^{11} cm^{-2}, determined from the periodicity of SdH oscillations versus inverse magnetic field shown in the inset. The temperature-dependent amplitude $\mathrm{A}_{SdH}(T)$ of the $\nu = 8$ minimum at $B = 1.56$ T, normalized by the base temperature value A_{SdH} ($T = 1.6$ K), is plotted in Figure 3.5b, and fit to the thermal damping term

$$X(T) = \frac{2\pi^2 k_B T/\hbar\omega_c}{\sinh(2\pi^2 k_B T/\hbar\omega_c)} \tag{3.1}$$

where k_B is the Boltzmann constant, T is temperature, and ω_c is the cyclotron frequency [53]. The effective mass, appearing in the cyclotron frequency, is determined from a least squares fitting of $X(T)$ to the temperature dependent amplitude of an oscillation at a given filling factor. A representative fit is presented in Figure 3.5b for the oscillation corresponding to $\nu = 8$ at $B = 1.56$ T. The envelope of SdH oscillations is described by

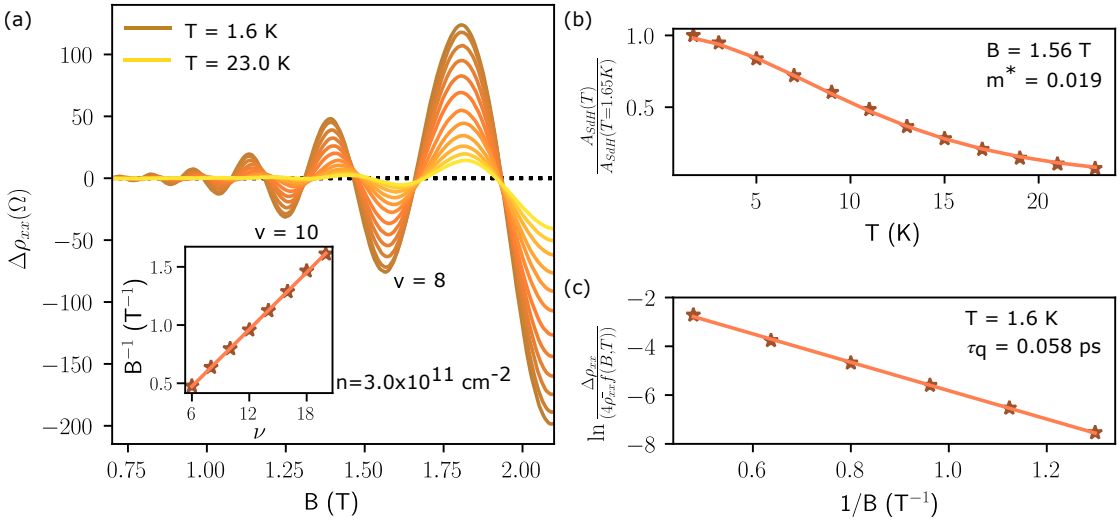

Figure 3.5: (a) Temperature-dependent amplitudes of SdH oscillations at fixed $n_{2D} = 3 \times 10^{11}$ cm^{-2} in G849 where $\Delta\rho_{xx}$ is obtained by subtracting a polynomial background from ρ_{xx}. (inset) The 1/B values of the minima in ρ_{xx} are plotted versus ν. The 2DEG density, determined from the periodicity of SdH oscillations, is given by the slope of the line $|e|/hn_{2D}$. (b) The temperature dependent amplitude of the $\nu = 8$ minima at $B = 1.56$ T in (a), normalized by its value at $T = 1.6$ K. The line is a fit to a temperature dependent factor, discussed in the main text, to determine the effective mass. A value of m$^* = 0.0189 \pm 0.0001$ at 1.56 T is found for a 2DEG density of 3×10^{11} cm^{-2}. (d) The effective mass is used to determine the the quantum lifetime from a Dingle plot given by $\ln(\Delta\rho_{xx}/4\bar{\rho}_{xx}f(B,T))$ vs. inverse magentic field. Data points corresponding to the minima in the oscillations of the $T = 1.6$ K trace in (a) are plotted versus $1/B$. A quantum lifetime of 0.58 ps is determined from the slope of the resulting straight line $-\pi m^*/|e|\tau_q$.

$$\Delta\rho_{xx} = 4\rho_0 X(T) e^{-\pi/\omega_c\tau_q} \tag{3.2}$$

where ρ_0 is the zero field resistivity, ω_c is the cyclotron frequency, and $X(T)$ is the thermal dampening term given previously [26, 20]. At low enough temperatures where thermal damping can be neglected, the amplitude of oscillations is described by the Dingle term $e^{-\pi/\omega_c\tau_q}$. Using a so-called Dingle plot, as shown in Figure 3.5c, the quantum lifetime τ_q is given by the slope of $\ln \Delta\rho_{xx}/4\rho_0 X(T)$ as a function of $1/B$. A value of $m^* = (0.0189 \pm 0.0001)m_e$ is obtained, which is higher than $0.014m_e$ found in bulk InSb. This larger value for the QW is found to agree quite well with the predictions of an 8-band $\mathbf{k}\cdot\mathbf{p}$ calculation for a symmetric InSb/$In_{0.9}Al_{0.1}$Sb QW, as presented in the following section. Although our QW is not symmetrical, the contribution due to wave function penetration of the barrier layers is shown to be quite small. The most dominant contributions to the mass increase appear to come from enlargement of the QW band gap due to confinement and strain, and from the strong non-parabolicity of the electron dispersion. It should be noted that our experimental fit gives an average parabolic mass that matches the number of states in the filled Landau levels to the number of states in the real non-parabolic dispersion.

Using the $T = 1.6$ K trace in Figure 3.5a, a quantum lifetime $\tau_q = 0.058$ ps, also known as the single-particle relaxation time, is extracted from the Dingle plot shown in Figure 3.5c. In comparison, the mean transport lifetime derived from the Drude model $\tau_t = \mu m^*/e$ is 0.21 ps. The ratio of transport to quantum lifetimes is thus $\tau_t/\tau_q \approx 4$. Since τ_t is weighted by the scattering angle whereas τ_q is related to total scattering, the ratio τ_t/τ_q provides insight into the nature of scattering affecting transport [21]. For transport mobilities limited by large angle scattering (as is the case here due to interface roughness), the ratio approaches unity. In other binary QW heterostructures, large ratios of ~ 40 have been reported in samples where small angle scattering from long range potentials (e.g., remote ionized impurities) was the dominant scattering mechanism, leading to high mobilities and long transport lifetimes [72]. Although our transport lifetime differs by more than a factor of ten from these reports, the quantum lifetimes are comparable and justify our use of dopants in the QW.

3.2.4 8-Band k·p model of InSb/$Al_{0.1}In_{0.9}$Sb quantum well

This subsection was written by Dr. Phillip Klipstein and included in this thesis to give context to our experimental results. This section can also be found in the supplementary information of our Applied Physics Letters [10].

Parameter	InSb	$Al_{0.1}In_{0.9}Sb$
a_0 (Å)	6.4794	6.44501
m_e^*/m_0	0.014	0.023
VBO (eV)	-0.053	-0.1021
E_0 (eV)	0.237	0.4066
Δ_0 (eV)	0.81	0.771
E_0' (eV)	3.4	3.43
Δ_0' (eV)	0.4	0.39
E_P (eV)	22.8	22.3
γ_1	35.0800	21.2858
γ_2	15.6400	8.7492
γ_3	16.6306	9.7356
a_c (eV)	-6.94	-6.757
a_v (eV)	-0.36	-0.245
b (eV)	-2	-1.935
c_{11} (Gdyne/cm^2)	684.7	704.2
c_{12} (Gdyne/cm^2)	373.5	379.6

Table 3.2: Material parameters used in the calculation, based on standard notation [79].

The 8 band $\mathbf{k}\cdot\mathbf{p}$ model of Livneh *et al.* is used with the parameters listed in Table 3.2 to estimate the effect of strain and quantum confinement on the in-plane effective mass of InSb [79, 80]. The model has been shown in the past to give very good agreement with the band gaps and absorption spectra of InAs/GaSb, InAs/AlSb and InAs/$InAs_{1-x}Sb_x$ type II superlattices (T2SLs) [64]. Using Eq. C1 of Ref. [79], γ_3 of the well material, and the three Luttinger parameters, γ_1, γ_2 and γ_3, of the barrier material, are calculated from γ_1 and γ_2 of the well, whose values we take from the work of Lawaetz [70]. This reduces systematic errors introduced when Luttinger parameters are taken from more than one source, and is well suited to quantum wells (QWs) with a ternary barrier material since it properly takes band bowing into account. The model also includes interface parameters which are quite significant in the case of the binary/binary T2SLs, but which are negligible in the present case due to the low aluminium concentration in the barriers, whose major constituent is the same as the binary quantum well material.

Figure 3.6 compares the in-plane band structures, $E\left(k_{||}\right)$, close to the band gap for relaxed and strained InSb and for a strained InSb/$In_{0.9}Al_{0.1}Sb$ superlattice with layer thicknesses of 93 ML / 70 ML (ML = monolayer $\approx$ 3Å), where the strain of -0.53% is provided by pseudomorphic growth on relaxed $In_{0.9}Al_{0.1}Sb$. Because the superlattice layers

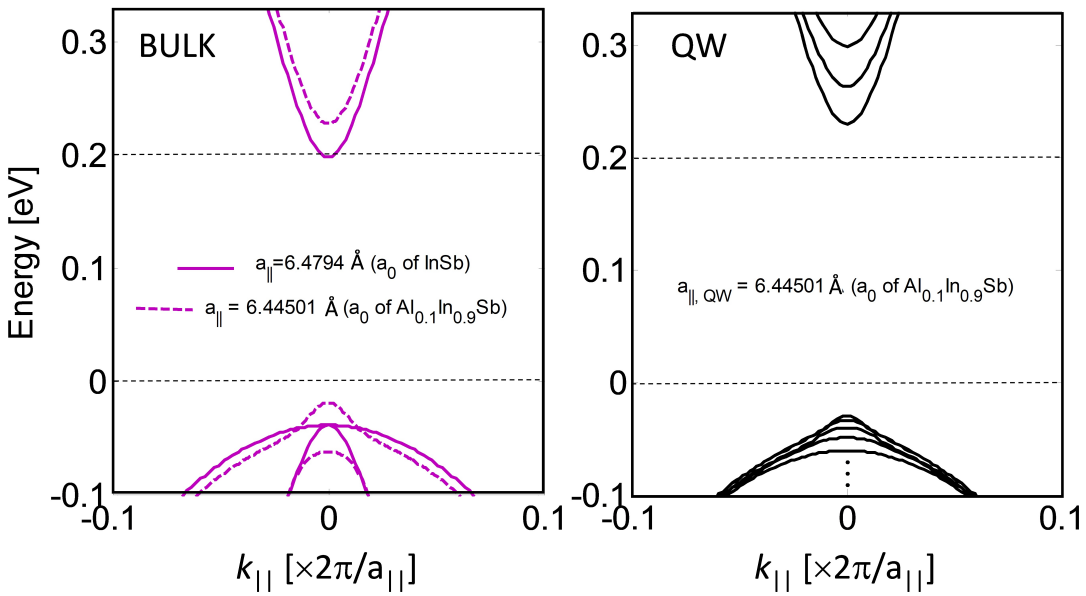

Figure 3.6: Comparison of the band structure in the in-plane [100] direction, for relaxed and strained InSb and for a strained 93 ML / 70 ML MQW. For bulk InSb, the bands have been shifted in each case so that the edges of the conduction bands are identical with those of a 93 ML / 70 ML MQW with the same in-plane lattice parameter. For the strained cases, the in-plane lattice parameter is that of relaxed $In_{0.9}Al_{0.1}Sb$. Only the first 3 conduction sub-bands and the first 5 valence sub-bands are shown for the MQW. In the legends, a_0 is the cubic lattice parameter.

are quite thick, there is negligible dispersion in the growth direction for the conduction and valence bands shown in Fig. 3.6, so the superlattice can be viewed as a multiple quantum well (MQW), where the in plane dispersion is the same as for a single QW.

When in-plane compressive strain is applied to bulk InSb, as shown in Fig. 3.6, the hydrostatic component tends to increase the band gap while the uniaxial component tends to reduce it, by splitting the valence band so that the heavy-hole (HH) is uppermost. Hence the band gap exhibits only a small net increase and the HH in-plane dispersion shows a clear anti-crossing with the light-hole (LH). Note that "heavy" and "light" refer to masses in the growth- or z-direction. This behaviour is reflected in the QW, where the valence band edge is HH-like, with a series of closely spaced HH sub-bands whose in-plane

dispersions anti-cross with the first LH sub-band. The main difference for the strained QW is that it has a band gap that is 11.3 meV (or 4.6%) larger than that of the strained InSb, due to the additional contribution of quantum confinement. The band gap is 20.9 meV (or 8.8%) larger than that of relaxed InSb.

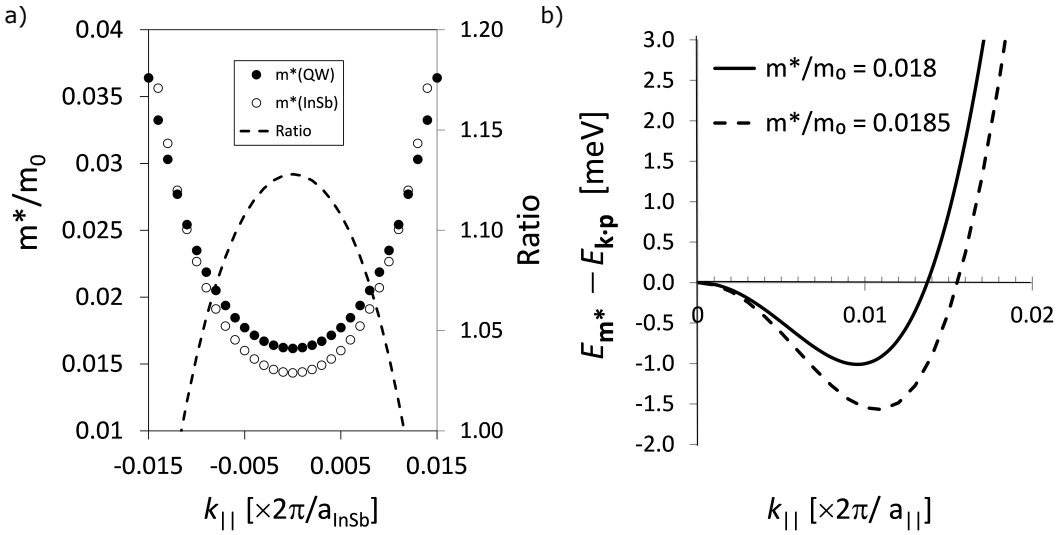

Figure 3.7: (a) Calculated band curvature effective masses in terms of the free electron value, m_0, and their ratio for relaxed InSb and the strained MQW ($a_{InSb} = a_0$ of InSb) (b) Difference between a parabollic dispersion and the $\mathbf{k} \cdot \mathbf{p}$ dispersion of the QW shown in Fig. 3.6, for different values of the effective mass, m^*.

In Figure 3.7a the electron effective masses and their ratio are shown for relaxed InSb and the strained QW. They are found by applying the formula,

$$m^* = \frac{\hbar^2}{|\partial^2 E/\partial k_{||}^2|}, \tag{3.3}$$

to a sixth order polynomial that provides a very good fit to the $\mathbf{k} \cdot \mathbf{p}$ dispersions in Fig. 3.6 over the range, $|k_{||} < 0.022 \times 2\pi/a_{InSb}$.Based on a simple two band QW Hamiltonian [12, 63],

$$H = A\left(\sigma_x k_x - \sigma_y k_y\right) + \sigma_z \left(\frac{E_0}{2} + B k_{||}^2\right) + I_0 D k_{||}^2, \tag{3.4}$$

the in-plane dispersion of the conduction band edge varies as $A^2k_{||}^2/E_0$ with an effective mass, $m^* = \hbar^2 E_0/2A^2$ (σ_i are the Pauli spin matrices, I_0 is the identity matrix, A is the electron-hole hybridization parameter, E_0 is the QW band gap, and B, D represent interactions with remote bands which are small and have been ignored). In the limit of infinite well width, $E_0 \to E_G$, where E_G is the bulk band gap. Since A scales inversely with the lattice parameter [38, 63], the electron band edge effective mass in the QW is decreased by 1.06% due to electron-hole hybridization, and increased by 8.8% due to the change in the band gap, giving an overall up shift of 7.7%. This is fairly close to the plotted value of 12.7% in Fig. 3.7a, suggesting that the two band model captures the essential physics of the band edge effective mass fairly well, but there may be a small additional contribution due to electron penetration of the barriers.

The rapid increase of the band curvature effective mass with wave vector in Fig. 3.7a shows that strong non-parabolicity exists in the conduction band of both bulk InSb and the QW. For the 2DEG density of $3 \times 10^{11}\,\mathrm{cm}^{-2}$ in Fig. 3.5a, the electron Fermi wave vector of $k_\mathrm{F} = 0.014 \times 2\pi/\mathrm{a}_\mathrm{InSb}$, corresponds to a band curvature effective mass in the QW of $0.033\,m_0$. This value does not agree with $0.019\,m_0$ measured at $B = 1.56\,\mathrm{T}$ in Fig. 3(b), because the magneto-transport assumes a parabollic model, whose mass is used to determine the Landau energies:

$$E_{N\uparrow,\downarrow} = (N + \frac{1}{2})\frac{\hbar e B}{m^*} \pm \frac{1}{2} g \mu_B B. \tag{3.5}$$

This parabolic mass value is fitted to the temperature dependent amplitude of the SdH oscillations, where electrons are thermally excited from nearly filled to nearly empty Landau levels [120]. Therefore we need to find a parabolic dispersion that intersects the $\mathbf{k}\cdot\mathbf{p}$ dispersion close to the Fermi wave vector. At this wave vector, the number of states within the zero field $\mathbf{k}\cdot\mathbf{p}$ Fermi circle matches the number of filled Landau states. Figure 3.7b shows that the difference between the parabolic and $\mathbf{k}\cdot\mathbf{p}$ dispersion energies vanishes at $k_F = 0.0137 \times 2\pi/a_{||}$[1] when the parabolic mass is $0.018\,m_0$. If we add the number of states in the next (empty) Landau level at 1.56 T for both spin directions, to take into account their role in the temperature dependence of the SdH oscillations, the wave vector for the circle that includes all of these states increases to $k_\mathrm{F}^* = 0.0157 \times 2\pi/\mathrm{a}_{||}$. Figure 3.7b shows that the effective mass corresponding to this circle increases to $0.0185\,m_0$. Thus an average value close to $0.0183\,m_0$, is expected to correspond to the measured SdH mass. Since the latter was found to be $0.019\,m_0$, the agreement between the $\mathbf{k}\cdot\mathbf{p}$ model and experiment appears to be quite reasonable.

[1]Note that $\mathrm{a}_{||}$ is used here for the QW while a_InSb at $k_\mathrm{F} = 0.0137 \times 2\pi/\mathrm{a}_{||}$ was used earlier, but the difference is small enough to yield the same prefactor close to 0.014.

3.2.5 Coincidence Measurement

The Landé g-factor g^* was measured in sample G839-3 at $\nu = 4$ for two different carrier densities, using a tilted magnetic field approach [33] to identify coincidences between the Zeeman and cyclotron energies $g^*\mu_B B_{\text{tot}} = \hbar e B_\perp / m^*$, where μ_B is the Bohr magneton, B_{tot} is the total magnetic field, and $B_\perp$ is the component of B_{tot} that is perpendicular to the 2DEG plane. By modeling the evolution of spin-split Landau energy levels, the effective g-factors $g^* = 33 \pm 2$ at 2.8×10^{11} cm^{-2} and $g^* = 41 \pm 2$ at 3.6×10^{11} cm^{-2} were obtained, in agreement with other reports of the effective g-factor in InSb [78, 75, 91, 137].

In Figures 3.8a and 3.8b the longitudinal resistivity ρ_{xx} as a function of the perpendicular magnetic field $B_\perp$ for different tilt angles θ is shown for G839 at densities corresponding to (a) $2.8{\times}10^{11}$ cm^{-2} and (b) $3.6{\times}10^{11}$ cm^{-2}. At $\theta = 0°$, we observe the onset of spin splitting at $\nu = 5$ around 2 T followed by both even and odd filling factors corresponding to $\nu = 4, 3, 2$ at higher fields. As the tilt angle is increased, the width of the minima in ρ_{xx} decreases for even integer filling factors ($\nu = 2, 4$) and increases for odd integer filling factors ($\nu = 3, 5$). Eventually, peaks will coalesce at even integer filling factors as minima in ρ_{xx} at odd integer filling factors approach their largest widths. The coalescing of peaks in this case corresponds to the crossing of spin split Landau levels of different spin polarizations and is used to determine the effective g-factor.

Figures 3.8c and 3.8d show the $B_\perp$ values of the peaks in the SdH oscillations shown in Figs. 3.8a and 3.8b respectively as a function of tilt angle θ. Peaks corresponding to the observed crossing at $\nu = 4$ in Figs. 3.8a and 3.8b are presented in 3.8c and 3.8d respectively. The evolution of peaks in ρ_{xx} as a function of θ is described by the evolution of the Landau level energy spacing described by

$$E_N = \hbar\omega_c(\theta)(N + 1/2) \pm \frac{1}{2} g^* \mu_B B_{\text{tot}} \tag{3.6}$$

where $\hbar$ is the reduced Planck constant, $\omega_c(\theta) = eB_\perp(\theta)/m^*$ is the cyclotron frequency, $N = 0, 1, 2, ...$ is an integer, g^* is the effective g-factor, μ_B is the Bohr magneton, and B_{tot} is the total magnetic field. All scans were taken at two fixed gate voltages ($V_g = 0.75$ V and $V_g = 0.85$ V), which in this case did not correspond to a fixed density. Operating the piezo-electric rotator stage over the duration of the experiment was observed to change the relation of n_{2D} to (V_g). This particular sample, G839-3, had otherwise been very stable in many cooldowns in two other cryostats. For example, the stable pinch-off curves in Figure 3.1c, the stable Landau fan in Figure 3.3b, and the temperature dependence of the WAL peak in Figure 3.10 were performed on sample G839-3, with the density remaining

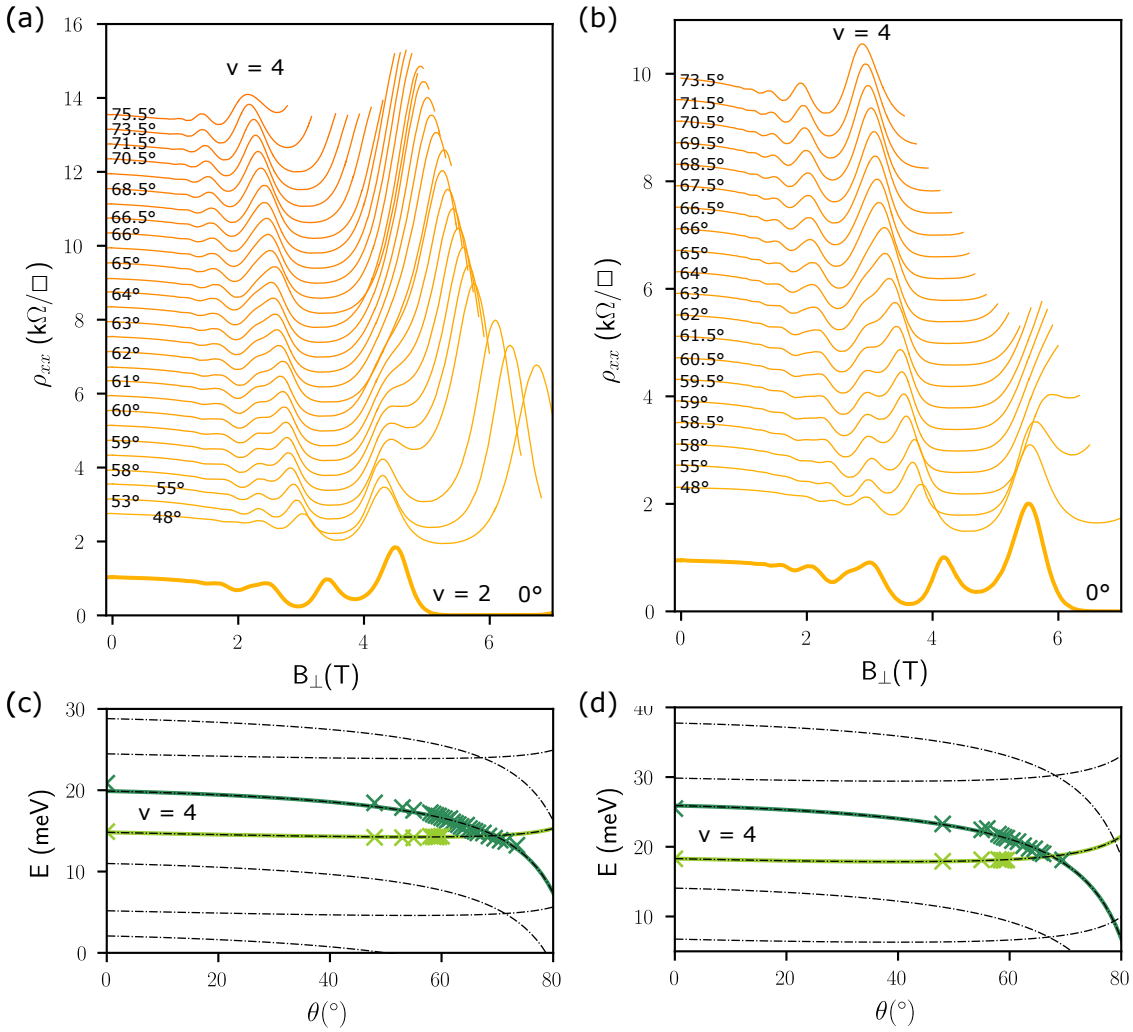

Figure 3.8: Coincidence measurement. (a) Longitudinal resistivity versus magnetic field at (a) $V_g = 0.75$ V and (b) $V_g = 0.85$ V is taken at various tilt angles θ with respect to normal vector of the sample surface. The perpendicular field values $B_\perp$ of peaks in resistivity surround $\nu = 4$ in (a) and (b) are plotted versus tilt angle θ in (c) and (d) respectively.

stable and reproducible for weeks at a time. Therefore, we cannot explain the density instability between scans at different tilt angles (during the scan, the density remains stable throughout), other than perhaps due to the heat pulse generated while the rotator moved to a different angle θ between scans. In any case, having measured the carrier density of each $B_\perp$ scan via the Hall effect, we modeled the density-driven change in the Landau level energy for each scan by using $\omega_c = eB_\perp/m^*$ and $\nu = hn_{2D}/eB_\perp$ for a given filling factor ν. With this correction, a best fit of the spin split energy levels (solid lines) to the data (crosses) yielded an effective g-factor of 33 ± 2 at $\nu = 4$ in (c) and 41 ± 2 at $\nu = 4$ in (d).

3.2.6 Weak anti-localization

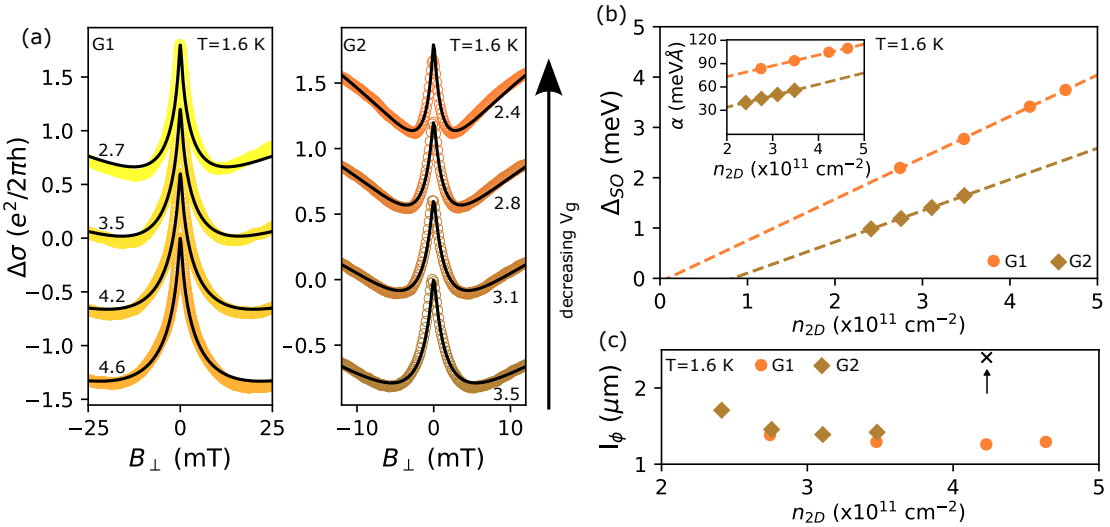

Figure 3.9: (a) Density dependence of weak anti-localization in G839 (left) and G849 (right). Experimental points are displayed as colored open circles and fits to the HLN model are shown as black lines. Curves are offset for clarity and labeled with the corresponding 2DEG density in units of 1×10^{11} cm^{-2}. (b) Spin orbit splitting Δ_{SO} vs density extracted from HLN fits to data in (a). A linear increase in Δ_{SO} is observed with increasing density in both wafers. (inset) Spin orbit coeficient $\alpha = \Delta_{SO}/2k_F$ (c) Phase coherence length l_ϕ vs. density acquired from HLN fits to data in (a). Also shown and indicated by a black arrow is the phase coherence in G839 measured at a temperature of 22 mK.

Wafers G839 and G849 are characterized by a strong and tunable spin orbit interaction

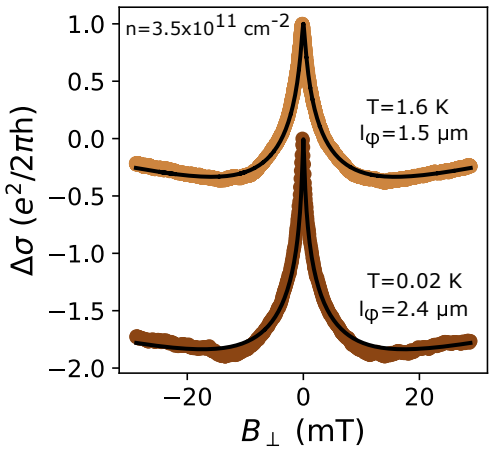

Figure 3.10: Weak antilocalization measurements of sample G839-3 taken at $T = 20$ mK and $T = 1.6$ K.

(SOI), as demonstrated by the weak anti-localization (WAL) conductivity peak observed in all Hall bars. The strength of SOI was determined from fits to $\Delta\sigma_{xx}$ using the Hikami-Larkin-Nagaoka (HLN) model,[51] where $\Delta\sigma_{xx} = \sigma_{xx}(B) - \sigma_{xx}(0)$, $\sigma_{xx}(B)$ is the field-dependent conductivity, and $\sigma_{xx}(0)$ is a constant background conductivity.

In systems with strong spin-orbit interaction, the longitudinal conductivity in small magnetic fields exhibits a pronounced peak at B = 0 due to the suppression of coherent backscattering. In our measurement, the longitudinal conductivity $\sigma_{xx}(B)$ is determined from simultaneous measurements of the longitudinal and transverse resistances. As shown in Figure 3.9, the conductivity correction $\Delta\sigma_{xx}(B) = \sigma_{xx}(B) - \sigma_{xx}(0)$ exhibits a peak in both G839 and G849 for various densities. The strength of SOI is quantified from fits of the conductivity correction to the Hikami Larkin Nagaoka model [51]. The conductivity correction of the HLN models reads:

$$\begin{aligned}\Delta\sigma_{xx}(B) = \frac{e^2}{2\pi^2\hbar}\Bigg(&\Psi\Big(\frac{1}{2}+\frac{H_\phi}{B}+\frac{H_{SO}}{B}\Big)+\frac{1}{2}\Psi\Big(\frac{1}{2}+\frac{H_\phi}{B}+\frac{2H_{SO}}{B}\Big)\\&-\frac{1}{2}\Psi\Big(\frac{1}{2}+\frac{H_\phi}{B}\Big)-ln\Big(\frac{H_\phi+H_{SO}}{B}\Big)-\frac{1}{2}ln\Big(\frac{H_\phi+2H_{SO}}{B}\Big)\\&+\frac{1}{2}ln\Big(\frac{H_\phi}{B}\Big)\Bigg).\end{aligned} \tag{3.7}$$

The fit parameters H_ϕ and H_{SO} correspond respectively to the phase coherence and spin-

orbit effective fields and Ψ is the Digamma function. The fit parameters can be converted to their corresponding lengths using $l_\phi = \frac{\hbar}{4eH_\phi}$ and $l_{SO} = \sqrt{\tau_{SO} D}$ where D is the diffusion constant.

Figure 3.9b shows the density dependence of the spin-orbit strength in samples G839-1 and G849-1, obtained from fits presented in Figure 3.9a. The Rashba parameter α_{SO} is related to spin orbit length via $\alpha_{SO} = \Delta_{SO}/2k_F$ and $\Delta_{SO} = \sqrt{2\hbar^2/\tau_D\tau_{SO}}$ where Δ_{SO} is the energy gap, k_F is the Fermi wave vector, τ_D is the diffusion time, and τ_{SO} is the spin orbit time. The Rashba parameter α_{SO} reaches a maximum of nearly 130 meV·Å at the highest density in G839: being related to structural asymmetry, α_{SO} is enhanced by the asymmetry of the wavefunction in the QW at high electric fields. Comparing wafers G839 and G849, α_{SO} is weakened in G849 by nearly a factor of two for all devices measured. The delta-doped InAlSb layer in G849 is responsible for this behavior: it causes band bending that pulls the 2DEG wavefunction towards the center of the QW, thereby reducing the structural asymmetry and Rashba component of the SOI. Figure 3.9c shows the phase coherence lengths l_ϕ determined from the fits to the HLN model are slightly larger in G849 than those in G839 at $T = 1.6$ K. Within the same wafer, l_ϕ reaches a maximum at the same density as the peak mobility. The phase coherence in G839 increases to 2.4 µm at 22 mK from 1.5 µm at 1.6 K in the same device at a similar carrier density (see Figure 3.10). In contrast, α_{SO} remains constant from 22 mK to 1.6 K.

3.2.7 Band structure profiles

Figure 3.11 shows band structure profiles calculated from self-consistent simulations solving both the Poisson and Schrodinger equations. The only structural difference between G839 and G849 is the delta-doped layer in G849, all other parameters are the same for both wafers.

Three observations can be made. At $V_g = 0$ ($n_{2D} = 0$), Figures 3.11a and 3.11b show the (empty) lowest 2D subband energy level in G849 is closer to the Fermi energy than in G839, predicting a lower turn-on threshold gate voltage for G849 than in G839. This is experimentally observed in Figure 3.1c. At the same electron density $n_{2D} = 2 \times 10^{11}$ cm^{-2} ($V_g > 0$, above turn-on threshold), Figures 3.11c and 3.11d show the 2DEG wavefunction peak in G849 is approximately 3.5 nm further away than that of G839 from the Si dopants in the n-InSb layer, predicting a slightly higher mobility in G849 than in G839. This is experimentally observed in Figure 3.3c. Figures 3.11c and 3.11d also show that the electric field across the 2DEG is more tilted in G839 than in G849, predicting a larger Rashba spin orbit coefficient in G839 than in G849. This is experimentally observed in Figure 3.9b.

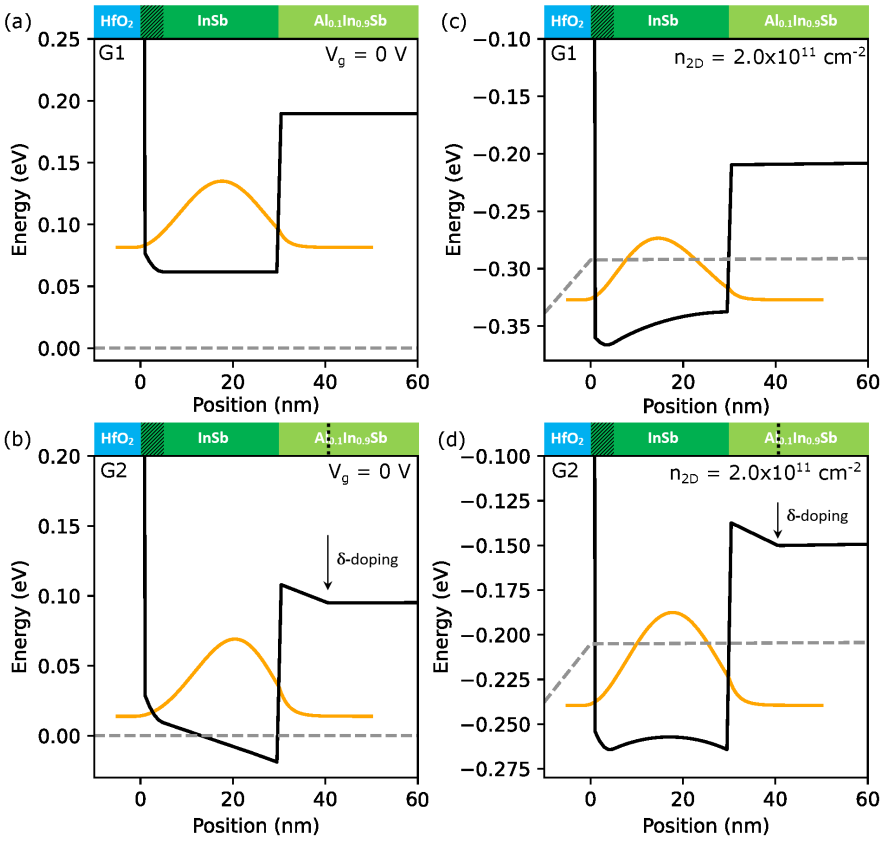

Figure 3.11: Calculated band structure profiles in the MBE growth direction of gated Hall bars fabricated from wafers G839 and G849.The corresponding MBE heterostructure is overlaid at the top of each panel, where "0 nm" corresponds to the HfO_2/InSb interface. The 5 nm thick n-InSb layer is indicated by the hatched area within the 30 nm InSb quantum well (dark green). For G849, the delta-doped layer in $Al_{0.1}In_{0.9}Sb$ is indicated by a dotted line. Band structure profile of depleted 2DEGS at $V_g = 0$ ($n_{2D} = 0$) for: (a) G839 and (b) G849. Band structure profile of populated 2DEGs at $n_{2D} = 2 \times 10^{11}$ cm^{-2} ($V_g > 0$) for: (c) G839 and (d) G849. In all four panels, the trapped charges associated with HfO_2, responsible for depleting the 2DEG after the dielectric deposition, are modeled by a delta-doped layer at the InSb/HfO_2 interface with a sheet density $N_{it} = 1 \times 10^{12}$ cm^{-2}, consistent with previously published reports. The 2DEG wavefunction (Ψ) is represented by a solid orange line, the conduction band edge by a solid black line, and the Fermi level by a dashed grey line.

In conclusion, we presented the growth, fabrication, and transport characteristics of high-quality, gate-tunable InSb 2DEGs in surface quantum wells grown on (001) SI-GaAs substrates. An n-InSb capping layer was used to realize reliable, low-resistance Ohmic contacts. Magnetoresistance measurements confirmed that intentional dopants in InSb are compatible with high-quality and reproducible transport characteristics, without parasitic parallel conduction or unstable carrier densities. Preliminary evidence suggests intentional dopants in InAlSb might be responsible for the time drift of transport characteristics. This could be further tested in an InSb 2DEG heterostructure with a short-period InSb/InAlSb superlattice doping scheme, where only the thin InSb layer is doped.

Chapter 4

Two-dimensional electron gases in undoped InAs/AlGaSb surface quantum wells

The last decade has seen spectacular progress in InAs/AlGaSb two-dimensional electron gases (2DEGs). The highest mobilities reported for this material system, near 2×10^6 cm^2/Vs, [125, 122] are the second highest values of *any* material system (the highest are near 4×10^7 cm^2/Vs in GaAs 2DEGs[128, 19]). InAs/AlGaSb has become the third material system only where the fractional quantum Hall effect can be routinely observed,[81, 66] in addition to 2DEGs in GaAs/AlGaAs [96, 62] and in ZnO/MgZnO.[32] The combination of high, strong spin-orbit interactions, pinning of the Fermi level in the conduction band, small effective mass, and large Landé g-factor makes InAs/AlGaSb a strong candidate material system for topological quantum computing with Majorana zero modes.

In the last decade, most efforts towards realizing Majorana fermions in a scalable platform have focused on near-surface quantum wells in the In(Ga)As/$In_{0.8}Al_{0.2}$As material systems where mobilities have significantly improved from 10,000 cm^2/Vs initially to more than 100,000 cm^2/Vs recently. However, in the context of topological quantum computing, the InAs/$Al_{0.9}Ga_{0.1}$Sb material system could offer possible advantages over the In(Ga)As/$In_{0.8}Al_{0.2}$As system, including better strain engineering, higher electron densities, higher mobilities, and stronger spin-orbit interactions [119].

Our InAs-based structures were grown on undoped GaSb (100) substrates by molecular beam epitaxy following the publication by C. Thomas *et al.* whose structures were designed to address parasitic parallel conduction through the substrate and the inability to fully

deplete a buried 2DEG with surface gates [123]. However, the details of the active region have been modified in this work for the study of surface quantum wells. Our surface quantum well structure sandwiches a 24 nm InAs quantum well between a 20 nm AlGaSb bottom barrier and a 6 nm InGaAs top barrier [30]. It represents the first "thick" InAs surface quantum well for use in our study of proximitized devices.

In this chapter, we demonstrate gated 2DEGs in $InAs/Al_{0.8}Ga_{0.2}Sb$ near-surface quantum wells, without parallel conduction in magnetic fields up to 18 T and electron densities up to 4×10^{12} cm^{-2}. Using SiO_2 as a dielectric yielded stable and reproducible gating operations all the way down to pinch-off. Rashba spin-orbit coefficients up to 50 meV·Å in the single subband regime are obtained through weak anti-localization (WAL) measurements

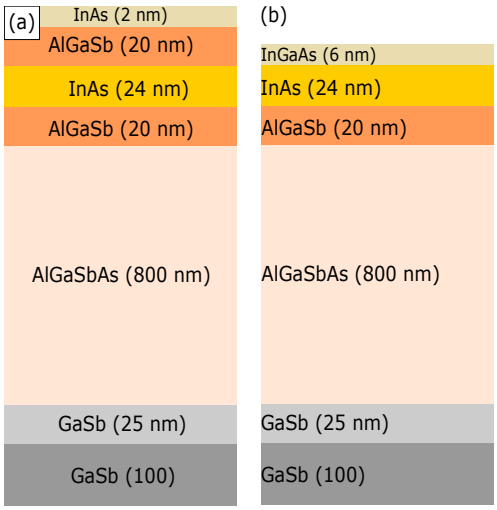

Figure 4.1: Schematic layer structure of (a) a buried InAs quantum well and (b) a surface InAs quantum well.

4.1 Growth of InAs quantum wells

All wafers were grown by molecular beam epitaxy (MBE) by Ahmed Elbaroudy with the following sequence of layers (see Figure 4.1), starting from a semi-insulating (SI) GaSb (001) substrate: a 25 nm GaSb smoothing layer, an 800 nm lattice matched $Al_{0.8}Ga_{0.2}Sb_{0.93}As_{0.07}$ dislocation filtering quaternary buffer, a 20 nm $Al_{0.8}Ga_{0.2}Sb$ bottom barrier and a 24 nm InAs quantum well. For buried quantum wells, the InAs layer is followed by a 20 nm $Al_{0.8}Ga_{0.2}Sb$ upper barrier and a 2 nm InAs cap as illustrated in figure 4.1a. For surface quantum wells, illustrated in figure 4.1b, the InAs quantum well is followed only by a 6 nm $In_{0.75}Ga_{0.25}As$ cap layer. There is no intentional doping anywhere in the heterostructures. The two series of growths studied here are summarized in Table 4.1 for buried quantum wells and table 4.2 for surface quantum wells.

4.2 Characterization of deep quantum wells

The preliminary series of buried quantum well heterostructures was grown to optimize control of the As composition in the quaternary buffer. I fabricated Hallbar devices from wafers in the first series to measure the as-grown carrier density and transport mobility of each wafer. The dependence of mobility and density on arsenic composition (As (%)) is presented in figure 4.2a,b together with data from the second series of surface quantum well heterostructure growths. The standard quantum well heterostructure presents a mobility dependence with peak mobilities occurring below 6% arsenic and degrading with increasing arsenic concentration. For a decrease in arsenic concentration, one growth (G585) with 2.3% exhibited parallel conduction (unique to this series) in the magnetotransport behavior attributed to conduction through the buffer or substrate. For the carrier density, a slight trend of increasing the carrier density with arsenic composition is observed in standard quantum wells with densities ranging from 4.4×10^{11} to 1×10^{12} cm^{-2}. The results of the standard quantum well series suggest that an optimal arsenic composition in the buffer is close to 5.3%, below the lattice-matched value of 7%.

Sample ID	μ (cm^2/Vs)	n$_{2D}$ (cm^{-2})	As (%)
G585	44,200	5.84×10^{11}	2.3
G681	122,000	5.23×10^{11}	5.3
G679	92,000	4.38×10^{11}	5.5
G600	97,000	6.3×10^{11}	6.1
G603	73,000	8.82×10^{11}	7.6
G661	100	1.0×10^{12}	12
G703*	1,700	2.4×10^{11}	6.4
G702*	20,000	1.8×10^{11}	7.3

Table 4.1: Buried InAs/AlGaSb quantum wells: Transport mobility μ and carrier density n_{2D} of growths in order of increasing percentage of As in the quaternary buffer. The $*$ denotes growths with InSb-like transitions at the quantum well and barrier layer interfaces.

In InAs/AlGaSb quantum wells, both the group III and group V elements change across the interface between layers. As such, the "type" of interface is determined by the elements that terminate the AlGaSb barrier growth and begin the InAs quantum well growth. An AlAs-like interface occurs when the AlGaSb layer is ended with aluminum, a group III element, and the InAs layer begins with arsenic, a group V element. The $Al_{0.8}Ga_{0.2}Sb$ barrier in our heterostructures is more likely to terminate with Al than with Ga due to the small amount of Ga in the barrier layer. Alternatively, an InSb-like interface occurs

Sample ID	μ (cm^2/Vs)	n$_{2D}$ (cm^{-2})	As (%)
G807	10300	1.3×10^{12}	6.0
G782	11700	1.6×10^{12}	6.4
G780	4800	1.6×10^{12}	6.6
G743	7500	2.0×10^{12}	7.0
G774	11300	1.3×10^{12}	7.5
G800	11800	2.0×10^{12}	8.0
G832*	11000	1.0×10^{12}	6.7
G837*	12400	1.2×10^{12}	6.8

Table 4.2: Surface InAs/AlGaSb quantum wells: Transport mobility μ and carrier density n_{2D} of growths in order of increasing percentage of As in the quaternary buffer. The $*$ denotes growths with InSb-like transitions at the quantum well and barrier layer interfaces.

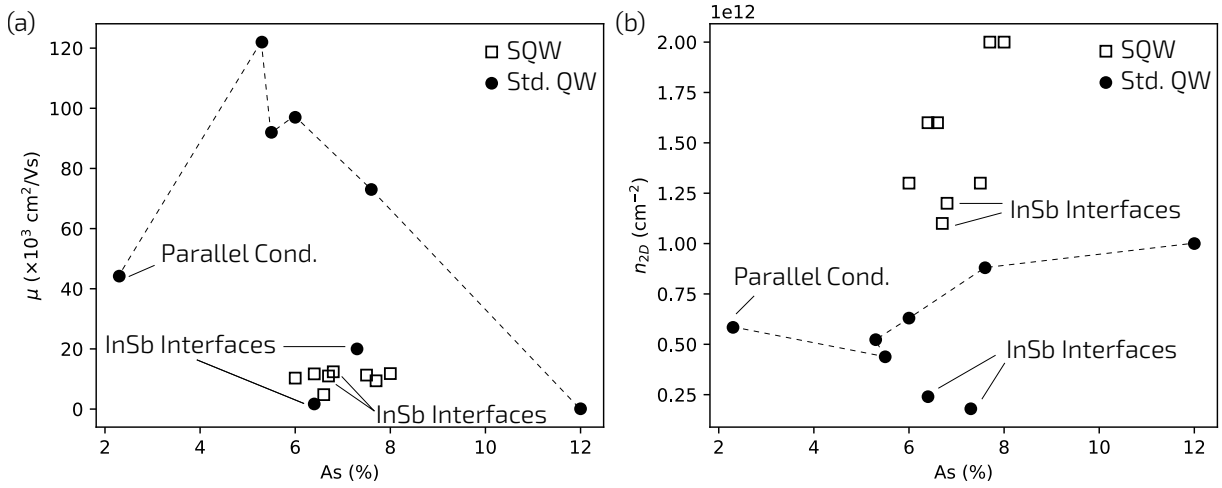

Figure 4.2: Arsenic composition: (a) Mobility and (b) density versus arsenic composition in the quaternary buffer for buried (circles) and surface (squares) quantum wells. Wafers grown with unique shutter sequence for InSb interfaces are denoted.

when the AlGaSb barrier is finished with antimony and the InAs quantum well begins with indium. With an optimized shutter sequence in MBE, a particular transition can be forced. It was found by Tuttle et al. that AlAs-like interfaces behave similarly to modulation-doped layers due to Al_{As} antisite defects appearing when the AlGaSb barrier surface is exposed to arsenic flux, allowing As atoms to replace Al atoms in the lattice [126]. Similar to modulation doping, these antisite defects act as charged impurities when they become ionized as a result of the large band offset. They may increase electron densities, but significantly decrease electron mobilities since they are located immediately adjacent to the quantum well. Alternatively, InSb-like interfaces do not exhibit enhanced carrier densities and were reported to greatly improve mobility; consistent with reduced interface roughness compared to the AlAs-like interfaces.

In each series, two quantum well heterostructures were grown with modified InSb interfaces as indicated in Figure 4.2. For these growths, a unique shutter sequence is used to saturate the surface with indium prior to growth of the InAs quantum well layer. The remaining wafers were grown with AlAs interfaces for increased electron densities compatible with proximity superconducting devices discussed in Chapter 6. As indicated in figure 4.2b, wafers with an indium interface from both series have reduced densities. Magnetrotransport data from a buried quantum well with and without InSb interface are shown in figure 4.3. The high-density sample (G603, Fig. 4.3a) exhibits well-defined quantized quantum Hall plateaus at Landau levels corresponding to vanishing resistance $\rho_{xx} = 0$ in longitudinal resistivity. The sample with InSb interfaces (G702, Fig. 4.3b) exhibits very few oscillations due to extremely low density with $\nu = 2$ occurring near 3 T and signs of possible percolation occurring at higher fields. Unlike buried wells, the surface quantum well series remains above 1×10^{12} cm^{-2} with InSb interfaces.

The increase in density with proximity to the surface is consistent with an enhanced contribution of carriers from surface effects, including surface Fermi-level pinning. For the surface quantum well series, all wafers were grown within 1% of the target arsenic composition. As shown in Figure 4.2a, moving the quantum well to the surface lowered the mobility by an order of magnitude compared to the buried quantum wells. Furthermore, the carrier density increases with a measured range of 1.3×10^{12} to 2.1×10^{12} cm^{-2} between the fabricated samples. The increase in carrier density is consistent with a reduction in the spatial separation of the quantum with surface states.

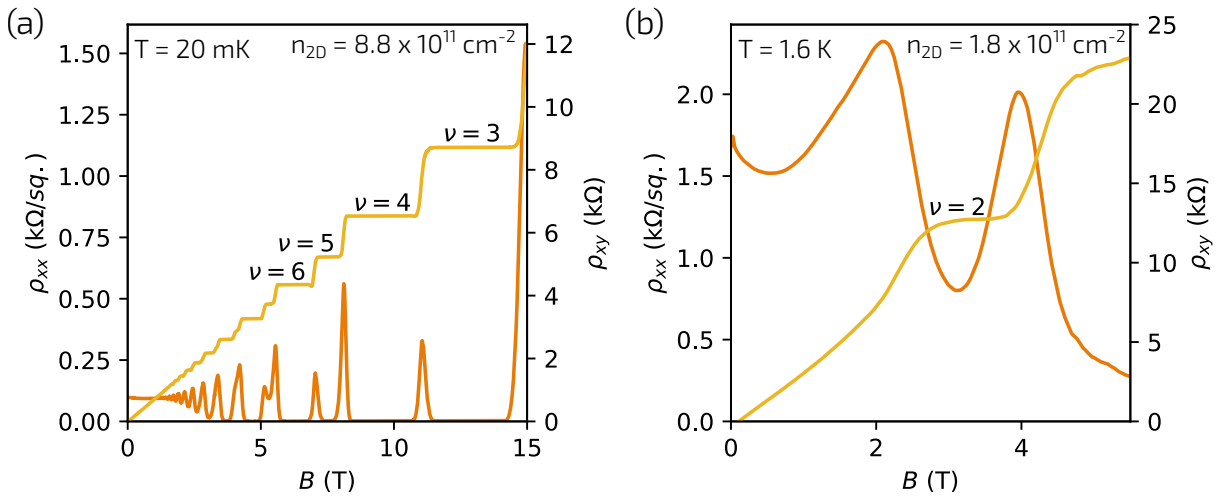

Figure 4.3: Magnetotransport behavior of (a) wafer G603 with AlAs interfaces and (b) wafer G702 with InSb interfaces at the bottom barrier interface with the quantum well. Both longitudinal resistivity (left axis) and Hall resistance (right axis) are plotted with filling factors denoted for convenience. Carrier density is significantly reduced from 8.8×10^{11} cm^{-2} to 1.8×10^{11} cm^{-2} by the change in type of interface.

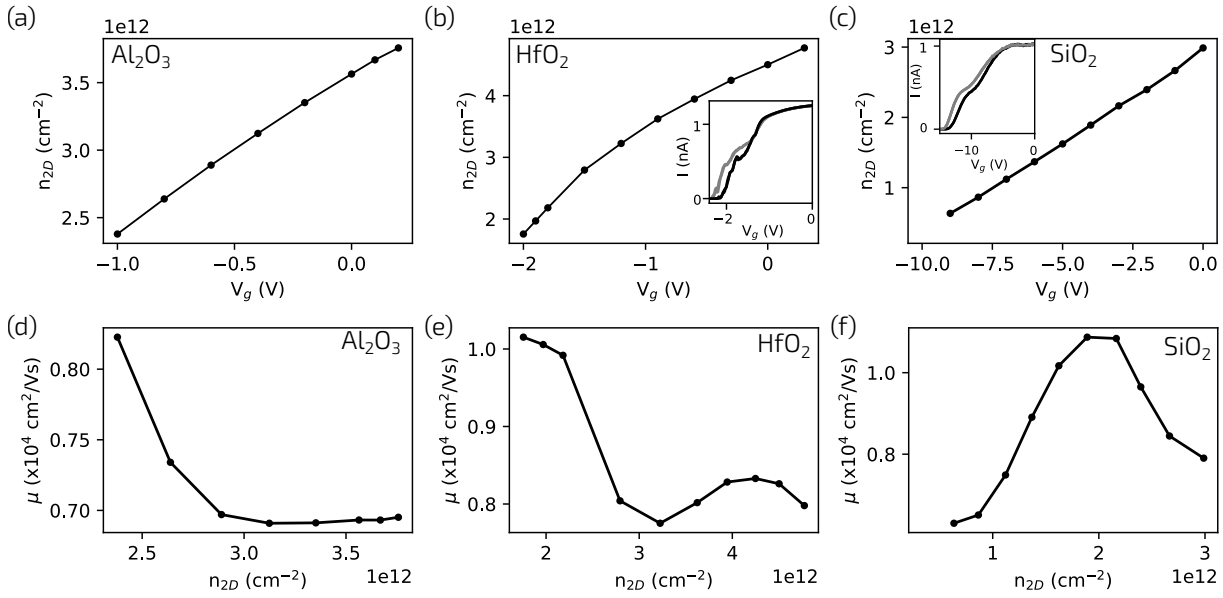

Figure 4.4: 4-Terminal Hall density versus top-gate voltage for gated Hallbars fabricated in wafer G782 with an (a) Al_2O_3, (b) HfO_2 or (c) SiO_2 gate dielectric. The density of 2DEG decreases with negative V_g in all samples, and is reproducible along the linear traces. (Insets) 2-terminal pinch-off curves exhibiting complete depletion of the conducting channels (I = 0) as a function of gate voltage. The pinch-off curves are stable and reproducible, perfectly overlapping when V_g is swept in the same direction and showing minimal hysteresis when V_g is swept in opposite directions. Eight traces are shown, four increasing V_g (gray) and four decreasing V_g (black). The peak transport mobility μ occurs near the same 2DEG density for Hallbars fabricated with (d) Al_2O_3 (e) HfO_2 and (f) SiO_2 gate dielectrics.

4.3 Characterization of surface quantum wells

Hall bars were fabricated using standard optical lithography and wet etching techniques. Mesa etching was terminated at a depth of ∼100 nm, in the quaternary buffer. The Ti/Au Ohmic contacts were deposited directly on the InGaAs cap with typical resistances of 400-500 Ω in magnetic field B = 0, and 10 kΩ in B = 18 T. For top-gated devices, a 60 nm thick gate dielectric (SiO_2, HfO_2, or Al_2O_3) was deposited by atomic layer deposition (ALD) at 150 °C, followed by the deposition of a global Ti/Au top-gate. Similarly to the InSb surface quantum wells of Chapter 3, the InAs surface quantum wells were fabricated with lithography techniques designed to protect the surface of the quantum well from unnecessary chemical exposure during fabrication. Additional details of fabrication are provided in Appendix A. Using standard ac lock-in measurement techniques, four-terminal and two-terminal transport experiments were performed in a pumped-4He cryostat and a 3He/4He dilution refrigerator, with a base temperature of 1.6 K and 11 mK respectively.

4.3.1 Electrostatic gating

In ungated Hall bars, the as-grown electron densities are reported in Table 4.2. The addition of a top-gate dielectric in proximity to the surface quantum well enhances the carrier density of the quantum well up to a factor of three (at $V_g = 0$) as reported here for wafer G782. The typical electron density function $n_{2D}(V_g)$ is presented in Figure 4.4a,b,c for top-gated Hall bars with different gate dielectrics. The tripling of the electron density after the dielectric deposition is most likely due to the significant change in surface pinning energy associated with the dielectric/InGaAs interfaces, where there is a high density of charge traps. The investigated oxides include Al_2O_3, HfO_2, and SiO_2 deposited by atomic layer deposition at 150°C. All dielectrics performed well in the high density regime with stable / reproducible gate characteristics, but only devices with SiO_2 gate dielectrics performed well in the low density regime. Hall density measurements of devices fabricated with Al_2O_3 and HfO_2 gate dielectrics were limited by substantial noise at low densities, as demonstrated by the pinch-off curves for HfO_2 in the inset of Figure 4.4b. Furthermore, noise and instability in devices with Al_2O_3 resulted in a failure to reach pinch-off. In contrast, 4-terminal Hall density and mobility measurements with SiO_2 gate dielectrics were reproducible in the low-density regime as presented in Figure 4.4c down to 0.2×10^{12} cm^{-2}. As shown in the inset of Figure 4.4c, the devices reach the pinch-off point for a sufficiently negative gate voltage, which demonstrates the ability to deplete all carriers in the quantum well. The pinch-off curve for SiO_2 is reproducible, overlapping perfectly

when V_g is swept in the same direction and showing minimal hysteresis when V_g is swept in opposite directions.

The dependence of transport mobility μ on 2DEG density is shown in Figure 4.4d,e,f for each gate dielectric. A peak mobility of ~11,000 cm^2/Vs near $n_{2D} = 2 \times 10^{12}$ cm^{-2} is observed in all traces. Data for the Al_2O_3 dielectric 4.4d did not reach the peak due to noise/instability in the device in this density range. Above the mobility peak, the decrease of mobility with increasing densities is attributed to either interface roughness scattering or alloy scattering, as the electron wavefunction is pulled closer to the surface by the increasing electric field of the top-gate [2, 111]. Devices with a HfO_2 dielectric exhibited the highest densities at $V_g = 0$ with a second (smaller) mobility peak appearing near 4×10^{12} cm^{-2} in 4.4e. At this density, the population of an additional subband is evident from the beating pattern observed in the SdH oscillations corresponding to multiple frequencies as shown in Figure 4.5. Through application of a negative voltage to the top gate, the quantum well can be tuned to single frequency SdH oscillations.

Figure 4.6 shows traces of longitudinal resistivity ρ_{xx} and transverse resistance (Hall) ρ_{xy} in a magnetic field up to B = 18 T for carrier densities ranging from 0.7×10^{12} to 3×10^{12} cm^{-2}. For decreasing densities, the slope of the Hall traces steepens and minimum in ρ_{xx} corresponding to a specific Landau level in the Hall trace moves to lower magnetic fields. Therefore, we are easily able to reach $\nu = 2$ at lower densities for a magnetic field range of 18 T.

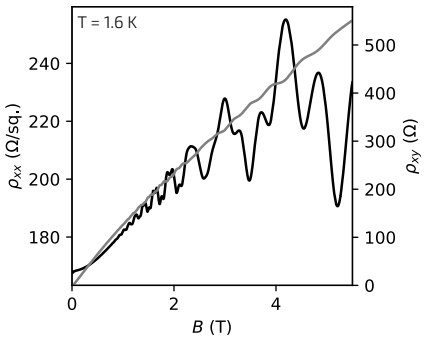

Figure 4.5: SdH oscillations (black) and quantum Hall (grey) of a G782 Hall bar with a HfO_2 gate dielectric at $V_g = 0$ V at a carrier density of $\sim 4 \times 10^{12}$ cm^{-2}. The carrier density is increased compared to that of the as-grown wafer as a result of the gate dielectric. A beating pattern in the SdH oscillations is observed as the result of multiple subband occupation in the quantum well at this density.

At all densities, the transverse resistance exhibits well-defined quantized Hall plateaus at Landau levels corresponding to the vanishing resistance $\rho_{xx} = 0$ in the longitudinal resistivity. We therefore rule out parasitic parallel conduction from a channel other than a 2DEG at all gate voltages. However, we observe an unusual ordering of the Landau levels at densities above 1×10^{12} cm^{-2}. As observed in Figure 4.6b, the $\nu = 3, 5$ plateaus strengthen with increasing magnetic field, whereas the $\nu = 4$ plateau disappears at high magnetic field. Furthermore, the 2DEG density determined from the periodicity of the Shubnikov-de-Haas oscillations ver-

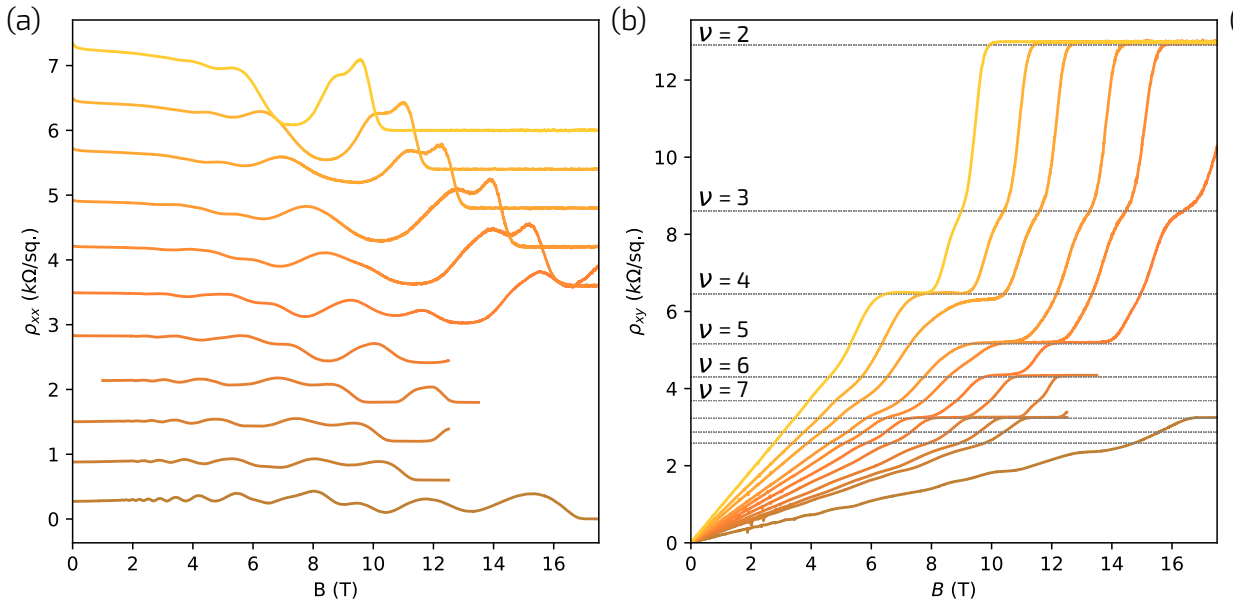

Figure 4.6: Magnetotransport data of sample G782 taken at 20 mK for a magnetic field up to 18 T. (a) SdH traces (offset for clarity) taken from V_g = -0.5 V (Bottom) to V_g = -8.5 V (Top). The corresponding Hall traces are provided in (b) with filling factors denoted for convenience.

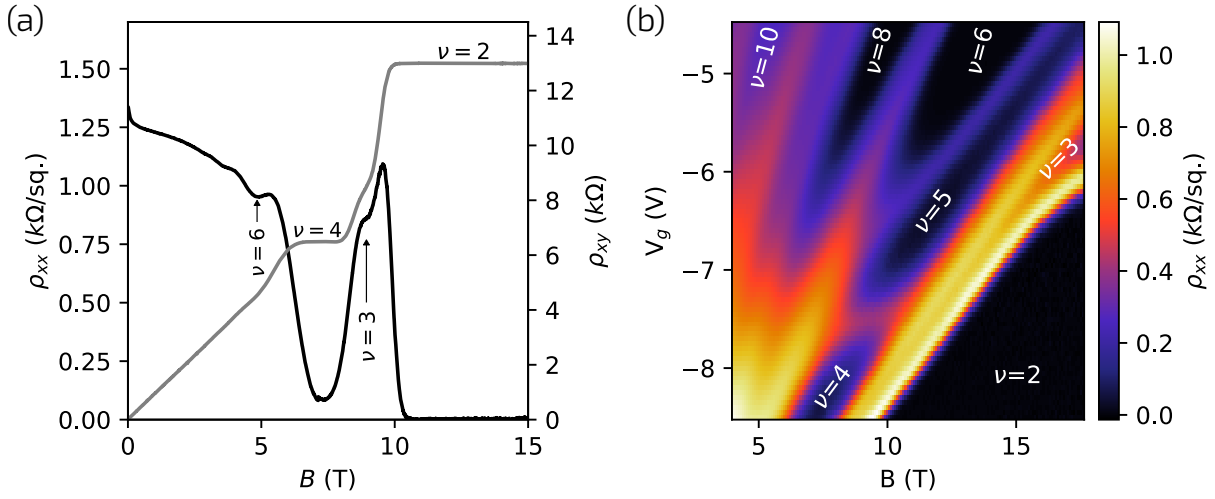

Figure 4.7: Magnetotransport data of sample G782 taken at T = 20 mK. (a) SdH oscillations (black) and integer quantum Hall (grey) up to filling factor $\nu = 2$ at $V_g = -9.0V$. (b)Landau fan diagram. Integer quantum Hall states from $\nu = 2$ to 10 are labeled.

sus the inverse field does not match the total carrier density n_{tot} determined by the classical Hall effect.

4.3.2 Landau Fan

Figure 4.7 shows Hall resistance ρ_{xy} and longitudinal resistivity ρ_{xx}, with well-defined quantum Hall plateaus at filling factors $\nu = 2$ and $\nu = 4$. The presence of quantized Hall plateaus is an absolute proof of the formation of a 2DEG. Despite a very large g factor ($g^* \sim 15$), the spin-split Hall plateau $\nu = 3$ is only beginning to appear at B = 10 T, due to disorder. The visibility of spin splitting is dictated by ($g^*\mu_B$B - Γ) > k_BT, where μ_B is the Bohr magneton, Γ is the disorder associated with Landau level broadening, and k_B is the Boltzmann constant. Magnetoresistance implies $\Gamma \sim 9$ meV in our samples, which is consistent with the mobilities reported here. This same disorder Γ is also responsible for the very late onset of the SdH oscillation (B $\sim$ 3 T), whose visibility is determined by ($\hbar$eB/m$^* - \Gamma$) > k_BT. At B = 17 T, the SdH oscillation minimum at $\nu = 2$ reaches $\rho_{xx} = 0$ in Figure 4.7a, implying that there is no parallel conduction from another conductive layer. This remains true at least until $n_{2D} = 2.8 \times 10^{12}$ cm^{-2} (V_g = -0.5 V). However, this does not exclude the possibility of a second subband populating the 2DEG. In fact, at $n_{2D} = 7.3 \times 10^{11}$ cm^{-2} (V_g = -8.5 V), there is a small mismatch (< 3%) between

the classical Hall density and the 2DEG density determined from the periodicity of SdH oscillations versus the inverse field. This mismatch grows significantly as the density of 2DEG increases (up to $n_{total} \approx 2n_{SDH}$). Energy level crossings in the Landau fan from Figure 4.7b confirm the presence of another 2D subband, most likely corresponding to the two spin-split branches of the lowest Landau level. We estimate that the second subband populates near $n_{2D} \approx 1 \times 10^{11}$ cm^{-2}, which is consistent with similar reports of populating second subbands in GaAs/AlGaAs and InAs/AlGaSb quantum wells [125, 141, 31]. At first sight, this onset of the second subband could appear inconsistent with the mobility peak in Figure 4.4c, where the decrease in mobility at higher densities could have been attributed to the onset of inter-subband scattering when the second subband populates. However, intersubband scattering in InAs/AlGaSb quantum wells typically limits mobilities to ~ 50 m^2/Vs far above the mobility of our samples (~ 1 m^2/Vs) and is therefore most unlikely to be the cause of the decrease in mobility in Figure 4.4c. On a different note, the curvature of the energy level associated with $\nu = 2$ is consistent with strong spin-orbit interactions in the system. Overall, the Landau fan, obtained by sweeping the top-gate at magnetic field increments, showcases the reproducibility and stability of gating characteristics with SiO_2.

4.3.3 Weak anti-localization

The wafers are characterized by a strong and tunable spin-orbit interaction (SOI), as demonstrated by the weak antilocalization (WAL) conductivity peak present in Figure 4.8a,b,c and observed in all Hall bars. The strength of SOI was determined from fits to $\Delta\sigma_{xx}$ using the Hikami-Larkin Nagaoka (HLN) model, where $\Delta\sigma_{xx} = \sigma_{xx}(B)$-$\sigma_{xx}(0)$, $\sigma_{xx}(B)$ is the field-dependent conductivity, and $\sigma_{xx}(0)$ is a constant background conductivity. Figure 4.8d shows the density dependence of the spin-orbit strength in sample G782, obtained from the fits presented in Figures 4.8a, b, and c. The Rashba coefficient α_{so} is related to spin-orbit length via $\alpha_{so} = \Delta_{so}/2k_F$ and $\Delta_{so} = \sqrt{2\hbar^2/\tau_D\tau_{so}}$ where Δ_{so} is the energy gap, k_F is the Fermi wave vector, τ_D is the diffusion time, and τ_{so} is the spin-orbit time. The Rashba coefficient α_{so} reaches a maximum of nearly 50 meV·Å at $n_{2D} = 1.4 \times 10^{12}$ cm^{-2} in G782 in agreement with reported values in the single subband regime of the InAs/InGaAs quantum well system [140, 135]. Being related to structural asymmetry, α_{so} is enhanced by the asymmetry of the wave function in the QW. The location of the 2DEG on the surface significantly enhances structural asymmetry in G782 due to a pinning of the Fermi level far below the edge of the conduction band (as discussed previously to explain the enhancement of the carrier density at $V_g = 0$ in devices with a top gate). In top-gated structures α_{so} is weakened over the measurable density range by nearly a factor of two. For negative

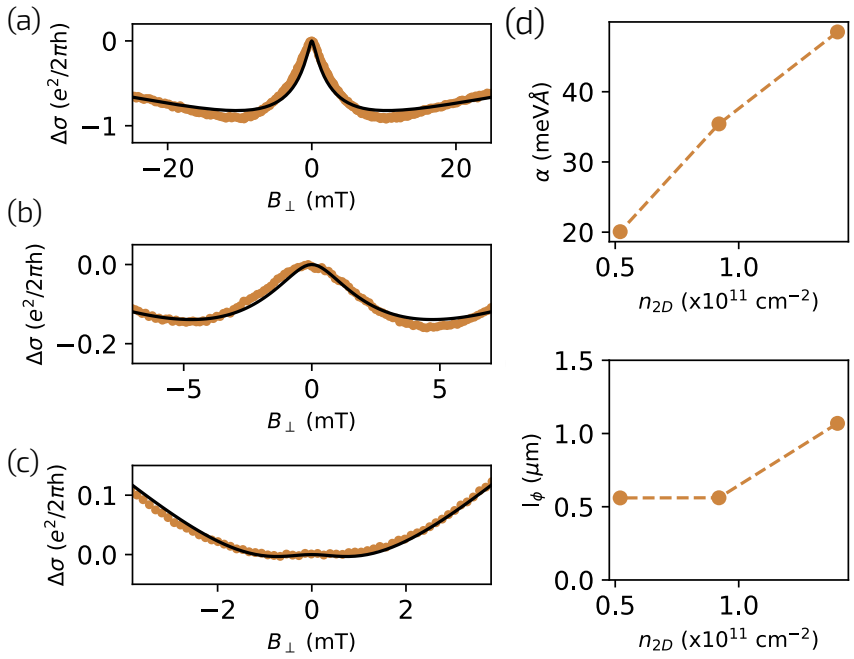

Figure 4.8: (a, b, c) Weak anti-localization of device G782 at carrier densities corresponding to 1.4×10^{12}, 0.92×10^{12} and 0.52×10^{12} cm^{-2} respectively. Experimental points are displayed as colored circles and fits to the HLN model are shown as black lines. (d) spin-orbit coefficient $\alpha = \Delta_{SO}/2k_F$ vs. density extracted from HLN fits to data in (a). (e) Phase coherence length l_ϕ vs. density acquired from HLN fits to data in (a) measured at T = 1.6 K.

gate voltages (decreasing carrier density), the field effect reduces the Fermi-level pinning below the conduction band and tilts the band structure in an orientation that pushes the 2DEG wavefunction away from the surface towards the center of the QW, thereby reducing the structural asymmetry and Rashba component of the SOI. This relationship $\alpha(n_{2D})$ is consistent with surface quantum wells without modulation doping (or back-gating), as previously shown in Chapter 3 for InSb surface quantum wells.

In summary, we have shown the magentotransport behavior of surface quantum wells in the InAs/AlGaSb material system. We have shown the choice in gate dielectric is highly influential over the 2DEG density, in all cases increasing the as-grown density, up to a factor of three. Furthermore, the choice in gate dielectric determines the quality of gating at low carrier densities, in some cases preventing full depletion of the 2DEG. We extract the Rashba SOC parameter up to 50 meV·Å in the single subband regime and show that it is in agreement with the more frequently reported InAs/InGaAs system. Considering the stark increase in carrier density observed in gated devices, which populates additional subbands in the quantum well, we recommend growing surface quantum wells thinner than the 24 nm width suggested for peak mobility in buried structures [125]. The reduced thickness will increase the subband spacing and move the single-subband regime to a more accessible gate-voltage range.

Chapter 5

Ex-situ superconducting contacts to surface quantum wells

This chapter describes the development of high-quality sputtered (ex-situ) superconducting contacts for planar Josephson junctions on a surface quantum well. In a planar junction geometry, the 2DEG extends beneath the superconducting contacts, differentiating it from the side-contact geometry of buried quantum well junctions [104, 57] or nanowires [16, 67]. Most efforts on the planar geometry in the last decade have focused on an in-situ platform of aluminum grown epitaxially on InGaAs/InAs quantum well heterostructures. This method achieves highly uniform, transparent interfaces between superconducting thin-film aluminum and an InAs surface quantum well, with reports of induced Δ^*'s approaching the gap of the parent superconductor [61, 60]. In-situ films are considered to be a more reliable process compared to ex-situ fabricated devices which must contend with the increased risk of contamination from air exposure and chemicals used in fabrication. However, this does not devalue the pursuit of improved ex-situ superconducting contacts. A reliable method of ex-situ contacts facilitates the study of alternative superconductors not typically available in III-V MBE systems [39, 47, 57]. Such alternative contacts would also be compatible with epitaxial aluminum samples to study the properties of multilayer superconductors [27]. Likely due to the quick advance of epitaxial aluminum junctions for the planar junction architecture, there is a void in the literature on ex-situ methods of fabrication, which this chapter aims to address.

5.1 Semiconductor cleanroom fabrication basics

All samples were fabricated in the quantum-nano fabrication and characterization facility (QNFCF) cleanroom at the University of Waterloo. The QNFCF cleanroom operates class 100 and class 10 modules corresponding to less than 100 and 10 particles/ft^3 respectively that are $\geq$0.3 μm in size. For reference, a typical domestic room has $\geq$ 100,000 particles/ft^3 of this size. More generally, a cleanroom is a controlled environment that maintains a low concentration of particles, a fixed temperature and humidity, and minimal vibration. Technologies originally developed by the semiconductor industry have been adapted for the needs of fabricating quantum devices where the length scales of devices are on the order of nanometers. The *planar process*, originally conceived by Jean Hoerni in 1959 to make transistors, is adopted in nano-fabrication and applied in this section.

As it sounds, the planar process begins with *planar* wafers and builds devices "layer by layer" through the repetition of three layer types: lithography (make a patterned film), deposition (grow a film), and etching (transfer a pattern into film). Each layer in a chip requires a combination of these three steps, and structures are built through successive cycles of fabrication. In research, lithography is typically performed using ultraviolet light (UV) or electron beams (e-beams) to write patterns where the resolution is proportional to the wavelength (λ). In UV lithography the minimum feature size is $\sim$ 1 μm and in e-beam lithography the resolution is $\sim$ 10 nm.

Lithography Lithography begins with the preparation of "resist", a photosensitive solution of long-chain polymers. The "resist" is poured across the surface of a sample, which sits on a rotating chuck and is subsequently accelerated to create a thin, uniform coating. The excess solvent is then removed by "softbaking" the sample on a hot plate to harden the resist and improve adhesion with the substrate. A pattern is transferred to the polymer film via optical UV or e-beam lithography, which alters the exposed polymers. In optical lithography, the spun polymer film is exposed to a UV lamp and the photoactive compound in the resist reacts with light. Light exposure either increases (positive) or decreases (negative) the solubility of resists in a mild basic solution called developer. For development, the exposed wafer is immersed in "developer" to develop for a set time. Too much time and features will appear wider than designed. Too little time and features will not be fully developed. A successful round of lithography will transfer a high-fidelity image of a device pattern into the resist film. In e-beam lithography, a similar process results in the dissolution of resist in developer depending on its exposure to a $\sim$nm diameter e-beam that "draws" out a pattern serially over a wafer. A lithographically defined pattern, whether

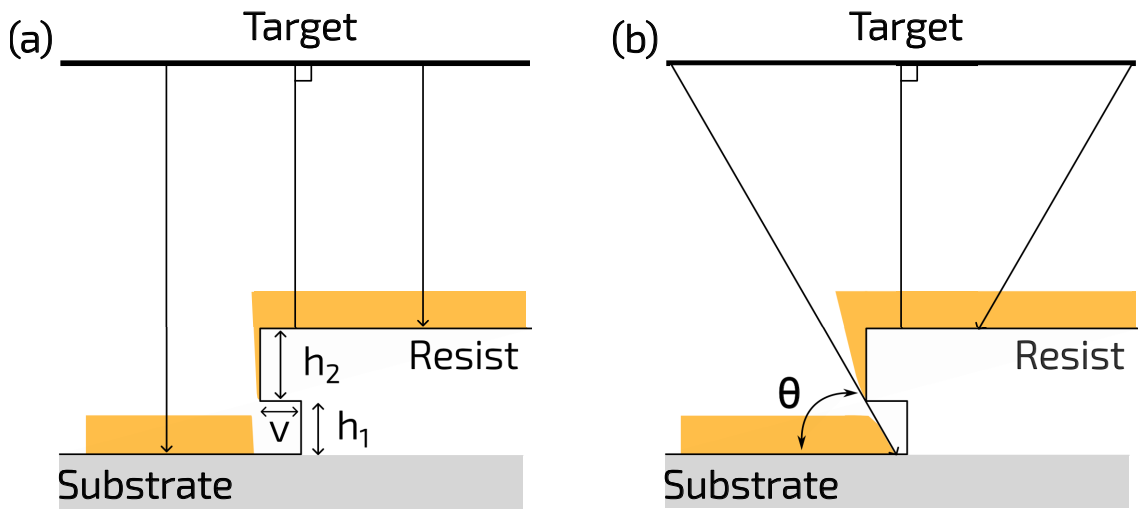

Figure 5.1: Lithographic parameters of an undercut resist profile. (a) Evaporative deposition of metal contacts normal to the substrate surface. The contact edge profile is nearly vertical and the undercut resist profile of depth v produces a pronounced discontinuity in the deposited metal film. (b) Sputter deposition includes various angles of incidence θ defined relative to the substrate. Deposition is therefore possible beneath the undercut and the contact edge will have a more pronounced taper.

optical or via e-beam, is ultimately permanently transferred to a substrate through the method of substrate etching or film deposition.

Deposition Metal films are commonly deposited by "physical vapour deposition" where a sample is put in a vacuum system and exposed to a beam of metal vapour. Two common ways of generating metal vapour are evaporation and sputtering. Evaporation heats a source with resistive heating or e-beam until the vapour pressure nears vacuum pressure in the chamber. This is a "line of sight" or directed deposition where the angle of incidence of atoms is generally normal to the substrate surface. On the other hand, sputtering involves physical bombardment of a source material with highly energetic ions to make a plume of material. The ejected atoms are then "sputtered" onto the substrate to form a film. It is a dense and "conformal" deposition, meaning atoms contact the sample at various angles of incidence.

When it comes to patterning a metal layer in a device structure, the differences in method of physical vapour deposition gains importance. The so-called "Lift-off" process

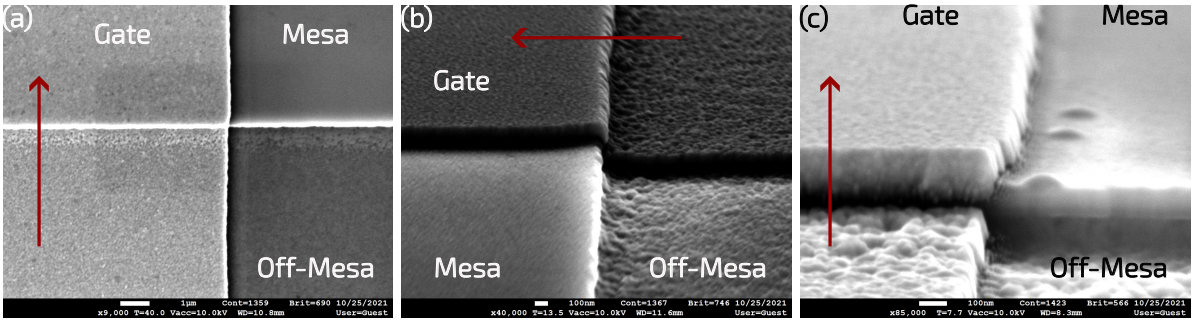

Figure 5.2: Deposited metal discontinuity caused by undercut profile. (a) Top view of a metal gate climbing the wall of a "mesa" with an undercut edge profile visible from the orientation shown in (b) which causes a discontinuity in the metal as shown in (c). Consistent perspectives are indicated by arrows.

is an extremely useful technique for lithographically patterning a metal layer prior to deposition. Metal deposits on the substrate where the pattern has been developed and on resist elsewhere. Excess metal deposited on the resist surface is then *lifted-off* when the resist below is dissolved in solvent. As shown in Figure 5.1a for evaporative deposition and 5.1b for sputtered deposition, this method requires an *undercut* edge profile in the resist that produces a discontinuity in the deposited metal film. The film would otherwise smoothly climb the resist causing deleterious tearing of the metal during lift-off. This method is therefore more commonly used with evaporative deposition since a sputtered metal is capable of coating beneath the undercut. Sputtered films are more commonly used as unpatterned layers in a device structure or are subsequently patterned via etching. An alternative example of edge profiles is provided in Figure 5.2 where an undercut profile from chemical etching of a substrate caused a discontinuity in a film deposited by electron-beam evaporation.

Etching Typically, etching is done by two methods: dry etching using a plasma reactor and wet etching using acid/base solutions. Dry reactive ion etching is the preferred method in industry where gas is introduced to a vacuum chamber, and then RF power is applied across a "parallel plate" geometry. Plasma discharge starts to create ions, radicals, and neutrals, which results in a mix of physical and chemical etching. Competing processes can ultimately be controlled to attain anisotropic or directional etching and is capable of etching high precision features when paired with a suitable resist for etch masking. Alternatively, wet etching uses an acid or base mixture to etch a film, it is a cheap and reliable process which often etches isotropically (in all directions at the same rate) and is

generally not suitable for very small features.

Scanning electron microscopy The success of any given fabrication step ultimately depends on consistent machine conditions or even the ambient state of the cleanroom. Optical microscopes are therefore compulsory equipment but are also limited in use for nano-scale features. Scanning electron microscopy (SEM) tools are widely used for this purpose, where resolution is generally a few nanometers. In SEM an e-beam is rastored across a sample surface by deflection coils and counts of secondary electrons are translated into "grey" level and projected on the screen. SEM is therefore suitable for imaging conductive samples.

5.2 Development of e-beam lithography for sputtering

Lithographic patterning of a substrate for lift-off of a sputtered metal is relatively uncommon due to the difficulty in producing smooth metal edges. Sharp edges are detrimental to top-down fabrication of field-effect transistors that rely on conformal deposition of a gate dielectric to isolate the gate from lower metallic layers in the device structure. Such films are incapable of conforming smoothly to sharp edges. Etching is therefore a more common method of pattering a sputtered metal, but is incompatible with the planar surface quantum well Josephson junctions that are the subject of this work since any damage to the semiconductor surface is reflected in the transport quality of the quantum well. Sputtered lift-off is therefore of general interest in applications that would be adversely effected by etching.

In the case of hybrid superconducting devices, sputtered contacts via lift-off are found in 1D nanowire devices [39], but they do not require the overlap of gates with the edges of the sputtered metal. The substrates were patterned with gates before the addition of nanowires and any attempt at depositing sputtered source and drain contacts. Therefore the quality of sputtered lift-off has no consequence on successful electrical isolation of the gate layer. For top-down fabrication of 2D quantum wells, lithographic gates are used on the surface of a quantum well heterostructure and commonly overlap with the edges of contacts. With the quick advance of epitaxial (in-situ) Josephson junctions on surface quantum wells, reports of ex-situ fabrication of superconductor-2DEG-superconductor junctions is limited to surface inversion layers or buried quantum wells where etching or etch masking is employed in the fabrication of contacts as opposed to a lift-off process.

As such, this chapter is devoted to my work developing a lift-off process for sputtered Nb using e-beam lithography. To provide context for the following sections, the fabrication of a Josephson junction device can be separated into the following stages:

1. Preparation (see A.1 for details)
2. Mesa (See A.2 for details)
3. Alignment marks
4. Superconducting source/drain contacts
    - e-beam lithography
    - Sulphur passivation
    - Sputtering
5. Interconnects (see A.6 for details).
6. Insulator (See A.4 for details)
7. Vias (See A.5 for details)
8. Top-gate and bond pads (see A.6 for details)

References to the relevant appendices are provided for more general fabrication steps. The focus of this section is on the development of superconducting contacts. More specifically, the development of a successful lift-off process that combines e-beam lithography, sulphur passivation, and sputtering.

5.3 Optimization of bilayer

I optimized a bi-layer resist profile for sputtered Ti/Nb contacts where both the height and depth of the undercut profile was tuned. Substrates used in this section were InAs surface quantum well wafers unless noted otherwise. The bilayer resist profile is composed of a first layer of lighter molecular weight PMMA (polymethyl methacrylate) A4 450k or copolymer MMA (methyl methacrylate) resist spun at 5000 rpm at a ramp rate of 1000 rpm/s for 60 seconds and baked on a hotplate at 180° C for 5 minutes followed by a second layer of heavier molecular weight PMMA A6 950k resist spun and baked with

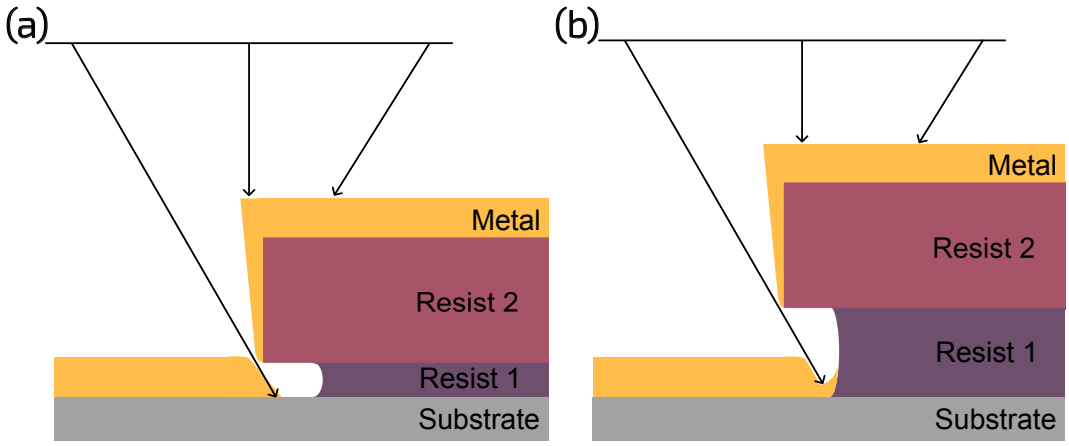

Figure 5.3: Metal contact edge profile for (a) thin and (b) thick resist 1 layer. Exact dimensions for each profile will depend on chamber geometry. For too thin layers a *microgap* will occur between the contact pad and metal deposited along the sidewall of resist 2 as beginning in (a). For too thick layers, deposition will occur continuously to the edge of resist 1 forming a skirt of metal around the primary contact pad.

the aforementioned parameters. Contact patterns are exposed via e-beam lithography and subsequently developed in a solution of IPA:DI water mixed 7:3 parts for 30 seconds with a final rinse in DI water to terminate development. Electron beam lithography is primarily employed to obtain a superconductor electrode separation of a few hundred nanometers which required the use of proximity effect correction to avoid overexposing the space between electrodes.

Metal contacts composed of sputtered Ti/Nb films were fabricated with titanium as an adhesion layer. The films were DC magnetron sputtered in an argon atmosphere on the lithographically patterned substrates using a AJA twin chamber sputter system. Prior to deposition, samples were ion milled using RF plasma for 6.5 minutes at 50 W power to remove native oxides resulting from air exposure. Typical film thicknesses for Ti (Nb) were 2 (80) nm at a deposition rate of 0.14 (0.15) nm/s. For both depositions the power was kept at 200 W.

Lift-off was performed by first soaking the sputtered wafers in PG-remover for longer than 10 hours at room temperature followed by heating in PG-remover at 70° C (in liquid) for 1 hour. Samples were then submersed in acetone and placed in an ultrasonic bath for an interval between 1 and 10 minutes. Time was dependent on lift-off results which were analyzed using an optical microscope as well as SEM.

In this study two parameters of the bilayer resist stack were varied: first layer thickness $h1$ and undercut depth v as defined in Figure 5.1. The layer thickness estimated from supplier spin-curves was confirmed by measuring with a Dektak profilometer as well as ellipsometry measurements. The undercut width v was varied by the relative development rates of the first and second layer of resist. SEM images were used to quantify the undercut width where sidewall deposition could be detected. A successful lift-off process was achieved before introducing sulfur passivation for use in more general applications. The effect of sulfur passivation is addressed afterwards.

5.3.1 Variation in first layer thickness

Variation in first layer thickness of a bilayer profile dictates the amount of metal that will deposit beneath the undercut. An example of this effect is provided in Figure 5.4, with corresponding SEM images of devices fabricated with variation in first layer thickness in Figures 5.4a,b. In Figure 5.4a, the lift-off from a PMMA/Copolymer bilayer produced contacts with a layer of metal (herein referred to as a 'skirt') bordering the edge of the intended contact pad area. In this case, the large $\sim$ 200 nm thickness of the copoloymer allowed a large range of incident sputtering angles to deposit underneath the undercut. For a thinner 80 nm layer of diluted MMA (1:4), deposition beneath the undercut is more restricted. The skirt shown in Figure 5.4b is reduced to a very fine metal layer likely consisting of highly energetic sputtered atoms that are capable of migrating along the surface of a substrate. In both cases, the edge of the skirt indicates where the edge of the first layer of resist resided and can be reduced by tailoring the depth of the undercut.

5.3.2 Depth of bilayer resist undercut

The undercut depth can be varied by the development time up to a point or by a change in the ratio of molecular weights of the resists involved in the bi-layer. In a bilayer resist stack, the ratio of molecular weights (Top layer/Bottom layer) is related to the depth of the undercut profile since the development rate is inversely proportional to the molecular weight. If the undercut is too shallow it will mimic single layer resist and if it is too deep then there will be a wide "skirt" deposited under the undercut.

PMMA resist is readily available as 495,000 and 950,000 molecular weight resins along with a Copolymer resist (MMA (8.5)). In deposition processes, a larger ratio (deeper undercut) generally corresponds to a more robust lift-off process. For sputtering, I compare two bilayer resist stacks with differing ratios of molecular weights. PMMA 950k served as

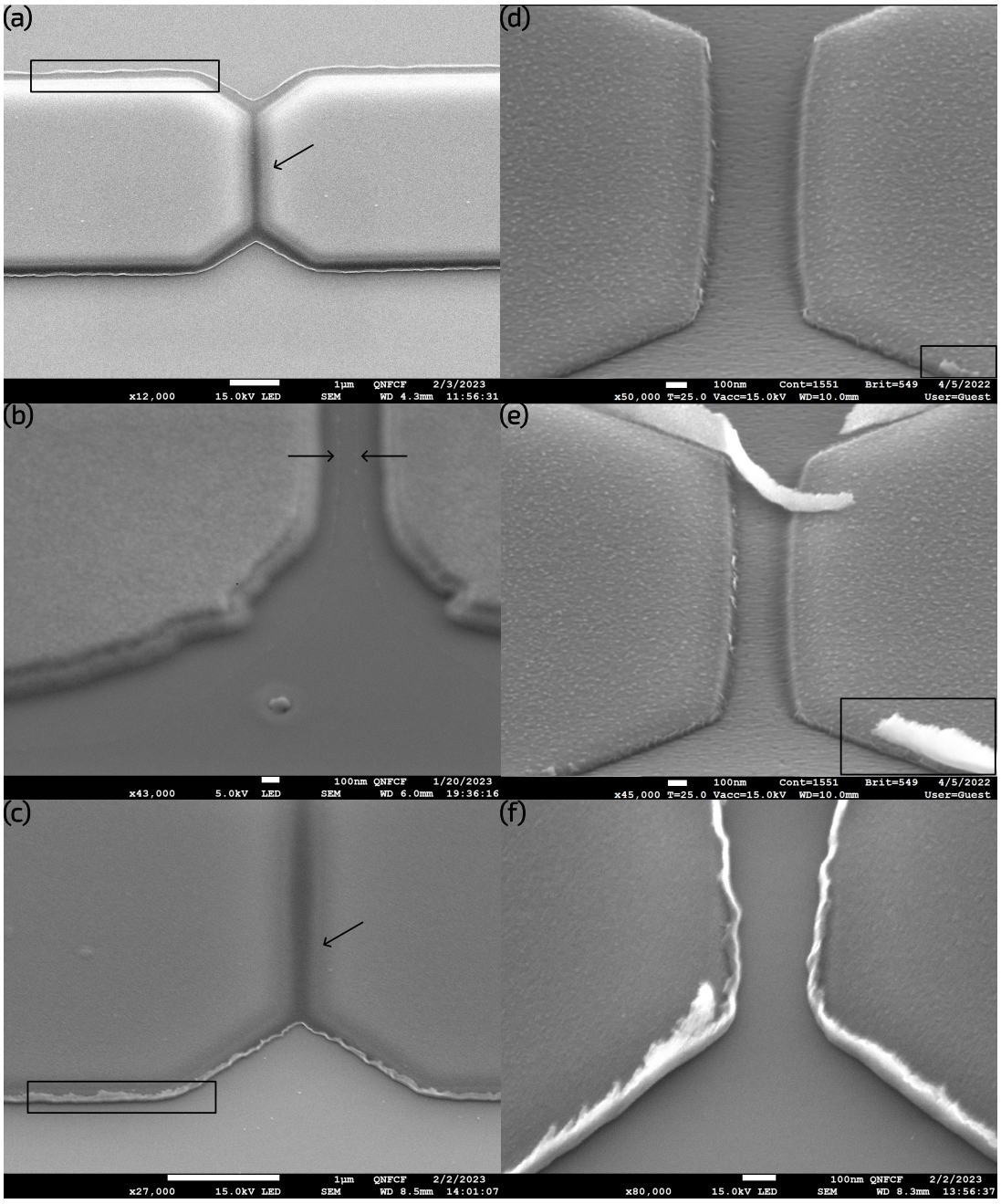

Figure 5.4: Caption located on following page.

Figure 5.4: (Previous page.) Progression of lift-off edges for bilayer resist profiles. (a) PMMA/MMA bilayer resist lift-off profile includes a thick, wide skirt of metal (box) that shorts the "gap" (arrow). By thinning the MMA layer (b), the thickness of metal composing the skirt is significantly reduced but the width is unchanged due to the migration of high energy atoms from sputtering under the undercut. The edge of this thin migration layer is marked by arrows for clarity. The width of the skirt can be reduced by reducing the undercut. (c) A smaller ratio of molecular weights in a bilayer PMMA 950k/PMMA 400K resist stack reduces the depth of undercut and reduces distance of migration of atoms. Some deposition of metal along the sidewall of the first resist layer is observed as a short edge of metal surrounding the pattern (box). (d) Ideal lift-off with smooth tapered edges. A small indication of fences is, however, observable in this Figure (box). (e) Gap between contact pad and deposition along sidewall of the resist is becoming insufficient for lift-off, thereby leaving 'fences' of metal (box). (f) The limit of a single layer resist profile creates steep "fences" of metal due to deposition along the sidewall of the resist that is taller than the deposition thickness.

the top layer in both stacks but the bottom layer was composed of either Copolymer MMA (8.5) or PMMA 495k. From figures 5.4b to 5.4f, the depth of undercut is reduced and a trend is observed. In figures 5.4b-d, the skirt of metal is first reduced until smooth metal edges are achieved, then upon further reduction the profile approaches a single-layer profile where substantial tearing or "fences" of metal are observed after lift-off as in Figures 5.4e,f.

5.3.3 Sulfur passivation

The process for successful lift-off of a sputtered metal pattern in the previous section was further tested for applications towards ex-situ high-transparency superconducting contacts to semiconductors. Ex-situ contacts to semiconductors are complicated by exposure to atmosphere (oxidation, particles, water adsorption, etc.) and cleanroom fabrication processes which cause surface contamination. To produce high-transparency contacts, clean and oxide-free surfaces must be prepared prior to deposition. We explored the method of sulfur passivation, a wet-etching process that removes native oxides and concurrently passivates the surface with a monatomic layer of sulfur atoms. The passivation reduces re-oxidation in air for the time it takes to transfer the passivated sample to a deposition chamber, approximately 1 minute, and is capable of producing high transparency contacts [39, 13, 71].

Following sample preparation methods of the previous sections, the sulfur passivation

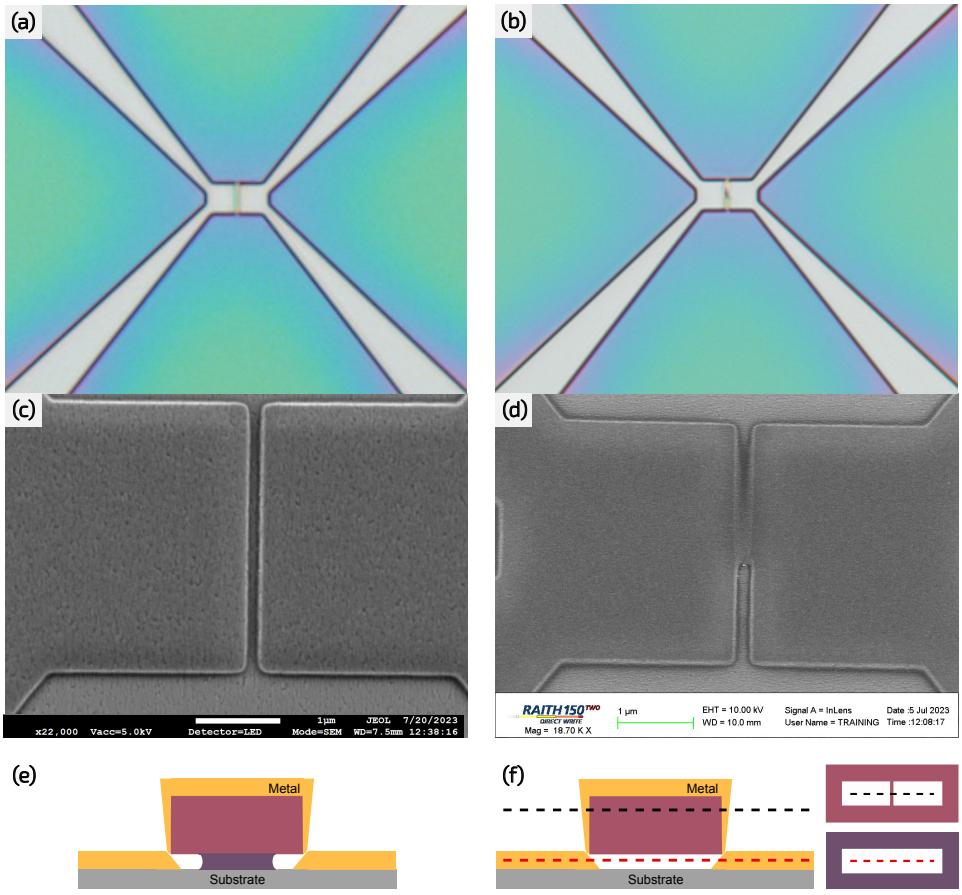

Figure 5.5: Optical images of fine features in resist (a) before and (b) after sulfur passivation reveal deformation of the resist by the sulfur passivation process. Subsequent SEM images of samples (c) without and (d) with defects from passivation reveal that contacts are connected by a skirt of metal where resist was deformed. As depicted in (e) the original bilayer resist profile is converted into (f) an air bridge due to the effective development of the first resist layer in passivation, resulting from poor adhesion of the resist to the substrate. In subsequent sputtering, the air bridge allows a skirt of deposited metal to short the contact pads.

process was introduced after development of a lithographically patterned sample and prior to loading the sample into the sputter chamber. The passivation process begins by removing the native oxide of the semiconductor with Buffered Oxide Etchant (1:10) in areas where the surface is clear of resist. The sample is then rinsed in DI water and transferred to a solution of ammonium polysulfide $(NH_4)_2S_x$ for 5-20 minutes of passivation under illumination and at room temperature. Optical images of the developed pattern before and after 20 minutes of passivation are shown in figures 5.5a,b. Observation with an optical microscope reveals that fine features of the resist are deformed by the wet etching process. Subsequent scanning electron microscopy is shown in Figures 5.5c,d reveals that the first layer of resist is cleared by passivation forming a resist bridge that allows the sputtered atoms to deposit beneath the bridge and connect adjacent patterns. A representative schematic of the original and modified resist profiles is provided in figures 5.5e, f.

For a shorter passivation period of 5 minutes, fine features obverved with optical microscopes appear robust to passivation. However, additional scanning electron microscopy revealed that poor adhesion properties from passivation persisted on InAs substrates, unlike on InSb substrates. As shown in Figure 5.6, a shadow pattern is visible on InAs substrates that corresponds to lateral etching of the native oxide in passivation due to poor adhesion of the resist to the substrate. An additional test was conducted to improve adhesion that included a native oxide etch of the substrate in Buffered Oxide Etchant (1:10) prior to spinning resist. The result improved adhesion, but introduced sharp edges in lift-off. However, the enhanced adhesion of resist to InSb substrates in particular, produced ideal devices with smooth lift-off of metal contacts and well defined features as shown in Figure 5.7. For longer passivation times of 20 minutes, fine resist features were effected on both InAs and InSb substrates.

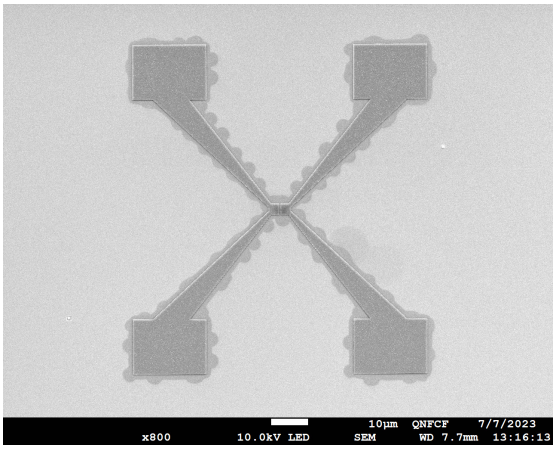

Figure 5.6: Scanning electron microscopy image of a Nb Josephson junction patterned on an InAs substrate with an etch shadow resulting from delamination of the resist during passivation.

In summary, we discussed the development of a nanofabrication procedure for high-quality, sputtered (ex situ) superconducting contacts for planar Josephson junctions on a surface quantum well using electron beam lithography, sulfur passivation, and sputtering. We have discussed the essential aspects of bilayer resist profiles and demonstrated that

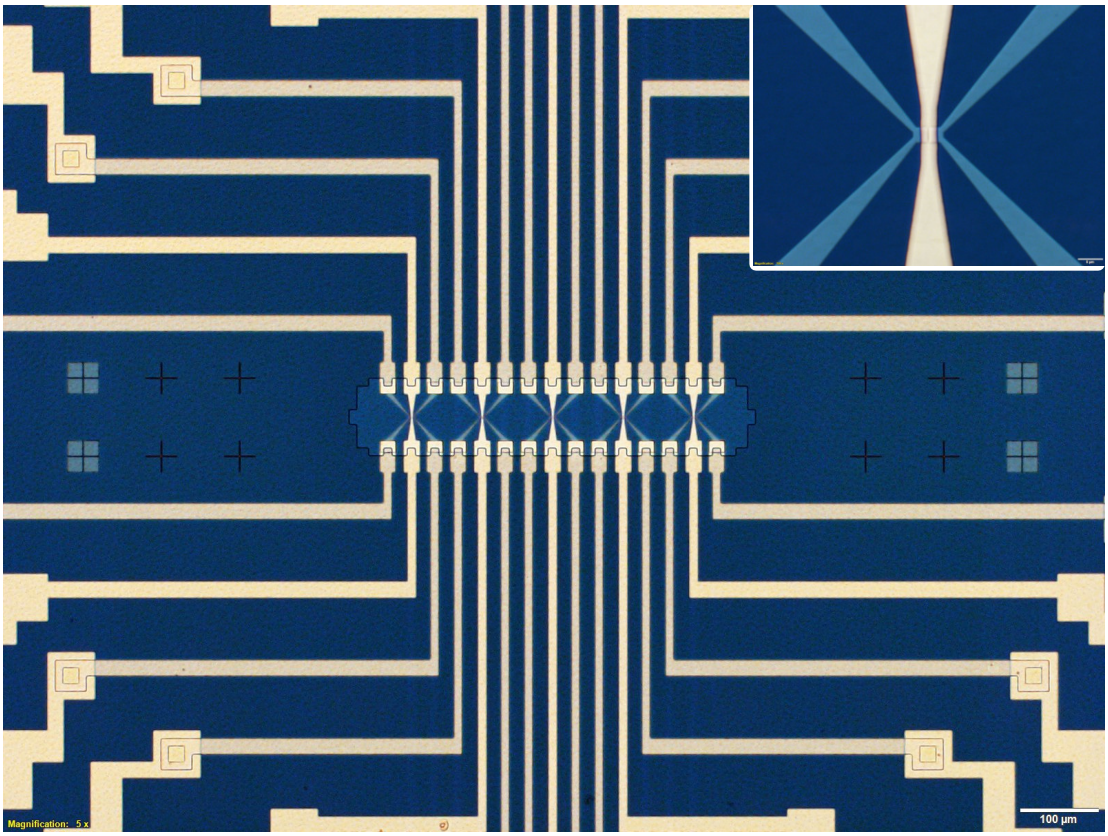

Figure 5.7: Optical image of five gated Josephson junction devices on an InSb surface quantum well wafer (G839). (Inset) Magnified view of a single junction emphasizing the quality of the sputtered Nb (light blue) lift-off procedure. Due to the quality of liftoff, a Ti/Au top-gate (yellow) was deposited over the junction overlapping with the Nb leads and was isolated (no electrical shorts) from the leads by a 60 nm dielectric.

systematically tailoring the resist profile dimensions can achieve a clean liftoff of sputtered Niobium. As confirmed by SEM imaging, we tailor the dimensions of the resist profile to demonstrate the transition between a skirt profile, a clean profile, and a fence profile at liftoff. Additionally, we discussed the limitations of our study when it comes to a wet etching procedure used to remove native oxides and ultimately achieve high-transparency contacts to the semiconductor quantum well, a necessity for future devices involving both our InAs and InSb material systems. Observation with an optical microscope reveals that fine features of the resist are deformed by the wet-etching procedure for passivation times exceeding 5 minutes because of limited surface adhesion of the resist, which was shown to be substrate dependent. Ultimately, the success of this fabrication procedure is given by the production of Josephson junction devices with high-quality device characteristics, as discussed in the following chapter.

Chapter 6

Proximity Superconductivity in InAs/AlGaSb surface quantum wells

Interest in the development of transparent contacts between superconductors and semiconductors (S-Sm systems) is motivated by potential applications in spintronics, topological superconductivity, and superconducting quantum computation [36, 34, 49]. Three factors can lead to a deterioration of the S/N interface: (1) The carrier density of the semiconductor is usually lower than that of the superconductor, which can cause a mismatch in the Fermi velocity of the carriers. (2) The interface between the two materials can be damaged due to fabrication of the sample (3) the semiconductor can inherently have an unfavorable conduction band profile (Schottky barrier) at the surface [94, 132]. Given these considerations, it has been shown that epitaxial contacts with high-density InAs surface quantum wells can improve the proximity effect in Josephson junctions, with interface transparencies ranging from 0.75 to 0.97 [61, 84, 50].

In this chapter, we focus on devices fabricated using ex-situ deposited contacts. Because InAs/AlGaSb quantum wells have surface Ferm-level pinning in the conduction band and are capable of extremely high carrier densities in undoped structures (on the order of 1×10^{12} cm^{-2}), Fermi velocity mismatch and barrier height at the interface with a superconductor are minimized compared to similar III-V systems (GaAs, InSb). With these properties, we achieve high transparency contacts, opening the door to studying proximity-induced superconductivity in a number of superconducting films not generally available in a III-V molecular beam epitaxy system.

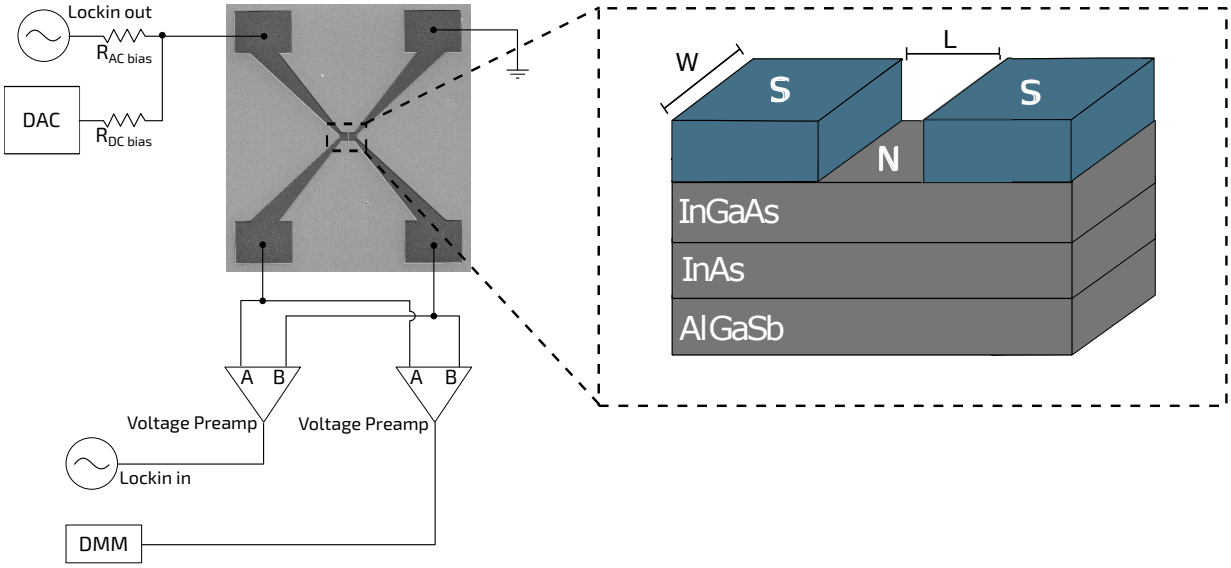

Figure 6.1: Current bias, 4–terminal measurement circuit used to measure the superconducting state of an SNS device. The resistance of the bias resistors is chosen based on the superconducting properties of the junction being measured. A schematic of the planar SNS junction on a surface quantum well heterostructure is shown in the figure expansion.

6.1 Measurement setup

Standard 4-terminal measurements can either be voltage-biased or current-biased. A 4-terminal measurement as shown in Figure 6.1 is used to measure solely the resistance of the sample and not the leads, since the current and voltage probes are separate. Since the characteristic feature of a superconductor is the absence of a voltage drop across the sample, the voltage-biased method is not best suited. Therefore, the measurement of SNS junctions is conducted using a 4-terminal constant current measurement setup. A constant current measurement is achieved by applying a source signal across a large resistor in series with the device. The large resistor, R, must be the dominating resistance in the circuit in order for small changes in the device resistance to be negligible to the circuit ($R >> R_{circuit}$). In doing so, a constant current passes through the circuit. I have performed constant current measurements using both standard dc and ac lock-in techniques discussed briefly here.

For measurements of the supercurrent with an anticipated critical current on the order of 10-100 μA, we use a bias resistor R_{DCbias} of 10 kΩ on the dc line and a bias resistor R_{ACbias} of 10 MΩ on the ac line with a 1 V ac excitation leading to I_{AC} = 100 nA. The 17 Hz oscillating current is multiplexed on the dc input current signal. The response voltage

thus has a 17 Hz component in a 100 nA sinusoidal window centered around the dc input current, multiplexed on the dc response voltage at the dc input current. Demultiplexing and downmixing the ac signal thus gives a direct measurement of differential resistance, at the same time as the dc I-V response curve is being measured. In the current bias setup the drain electrode is sent to ground to minimize noise in the circuit, but can be connected to a current preamp for diagnosing potential problems in the circuit.

6.2 Material Properties

Two generations of SNS samples were fabricated to study the interface transparency of our ex-situ fabrication process. The material properties of a two-dimensional electron gas (2DEG) heterostructure, essential for analyzing superconductor-normal-superconductor (SNS) devices, were determined in Chapter 4. The carrier density (n_{2D}) and mobility (μ) determined from the Hall bar devices of that chapter are used to derive the following quantities:

$$k_F = \sqrt{2\pi n_{2D}}, \qquad \lambda_F = \frac{2\pi}{k_F}, \qquad l_e = \frac{\hbar \mu_e}{e}\sqrt{2\pi n_{2D}}$$

where k_F is the Fermi wavevector, λ_F is the Fermi wavelength, and l_e is the mean free path. These quantities are reported for wafer G743 and G782 in Table 6.1.

Wafer	n (cm^{-2})	μ (cm^2/Vs)	k_F (nm^{-1})	λ_F (nm)	l_e (nm)
G743	2.0×10^{12}	7500	0.35	18	175
G782	1.6×10^{12}	11700	0.32	20	244

Table 6.1: Material properties of surface InAs/AlGaSb quantum wells in wafers G743 and G782. Quantities n and μ were measured using a Hall bar device from these wafers reported in Chapter 4. The remaining quantities in the table are derived.

The two generations of samples were fabricated with ebeam lithography and surface passivation techniques. The first generation of samples were patterned on wafer G743 with ebeam lithography using a single layer of PMMA resist and an ex-situ contact procedure:

1. Sulphur passivation for 20 minutes

2. Transfer to the sputter deposition system in under 2 minutes.

In the second generation of samples fabricated on wafer G782, the ebeam-lithography technique was modified according to Chapter 5 using a PMMA bilayer process and the modified ex-situ contact procedure:

1. Sulphur passivation for 5 minutes
2. Transfer to the sputter deposition system in under 30 seconds.

Further details of the sulphur passivation and sputter deposition procedure are provided in Appendix A.

6.3 Superconducting properties

I fabricated multiple planar Josephson junctions from InAs surface quantum well wafers G743 and G782. In the following assessment, we consider both scattering in the quantum well and the transparency of the InAs-Nb interfaces, which together introduce the relevant length scales characterizing transport. Semiconductor Josephson junctions (S-Sm-S) are classified according to the order of the following length scales: the mean free path of the 2DEG (l_e), the junction electrode separation length (L), and the superconducting coherence length in the semiconductor (ξ). The magnetotransport data of Chapter 4 yields a mean free path of 175 nm in wafer G743 and 244 nm in wafer G782. As summarized in Table 6.2, devices of different lengths L were fabricated from each wafer that span the quasi-diffusive ($L > l_e$) to quasi-ballistic ($L < l_e$) regimes.

As proximity superconductivity is a direct result of the Andreev reflection process, the effective superconducting coherence length in the Sm is determined by the length scale over which the Andreev process can maintain its phase coherence. This is affected by Δ_{Nb} of the 80 nm Nb film used for our sputtered electrodes in all devices. Using the BCS relation $\Delta = 1.75 k_B T_c$, we find $\Delta_{Nb} = 1.2$ meV. The coherence length in the semiconductor is then given by the following equations depending on whether the transport regime of the junction is determined to be ballistic ξ_b or diffusive ξ_d:

$$\xi_b = \frac{\hbar v_F}{2\Delta}, \qquad \xi_d = \sqrt{\frac{\hbar D}{\Delta}}$$

where v_F is the Fermi velocity given by $v_F = \hbar k_F/m^*$ and D is the diffusion constant $D = v_F l_e/2$ for a diffusive system with elastic scattering only [107, 85]. The ballistic and diffusive superconducting coherence length is reported in Table 6.2 for all samples. We can see from the table that all samples from G743 are likely in the short, diffusive and dirty regimes (($L < \xi$, $l_e < L$, $l_e < \xi_{d,b}$)). Samples from G782, with junction lengths of 150 nm or less, are likely in the short, quasi-ballistic, and dirty regimes ($L < \xi$, $l_e > L$, $l_e \approx \xi_{d,b}$) whereas longer junctions of 400 nm are likely in the long, diffusive and dirty regimes ($L > \xi$, $l_e < L$, $l_e \approx \xi_{d,b}$). It should be noted at this point that since the junction length is at best a factor of two smaller than the mean free path in our samples, the determination of a quasi-diffusive or quasi-ballistic nature requires further investigation into the behavior of the SNS.

Sample	L (nm)	l_e (nm)	ξ_b (nm)	ξ_d (nm)	Regime
G743J6 (C1)	200	175	346	246	short, diffusive, dirty
G743J6 (C2)	200	175	346	246	short, diffusive, dirty
G743J7 (C2)	200	175	346	246	short, diffusive, dirty
G782J1	120	244	220	320	short, quasi-ballistic, dirty
G782J2	120	244	220	320	short, quasi-ballistic, dirty
G782J3	150	244	220	320	short, quasi-ballistic, dirty
G782J4	400	244	240	380	long, diffusive, dirty
G782J5	400	244	230	350	long, diffusive, dirty

Table 6.2: Geometric properties of SNS junctions on InAs/AlGaSb surface quantum wells. The transport regimes are defined according to: short ($\xi > L$), diffusive ($l_e < L$) and dirty ($\xi > l_e$). For the reverse inequalities, the corresponding regimes are long, ballistic, and clean.

A parameter commonly used to assess the quality of an SNS junction is the product of the critical current and the normal state resistance, $I_c R_n$, known as the characteristic

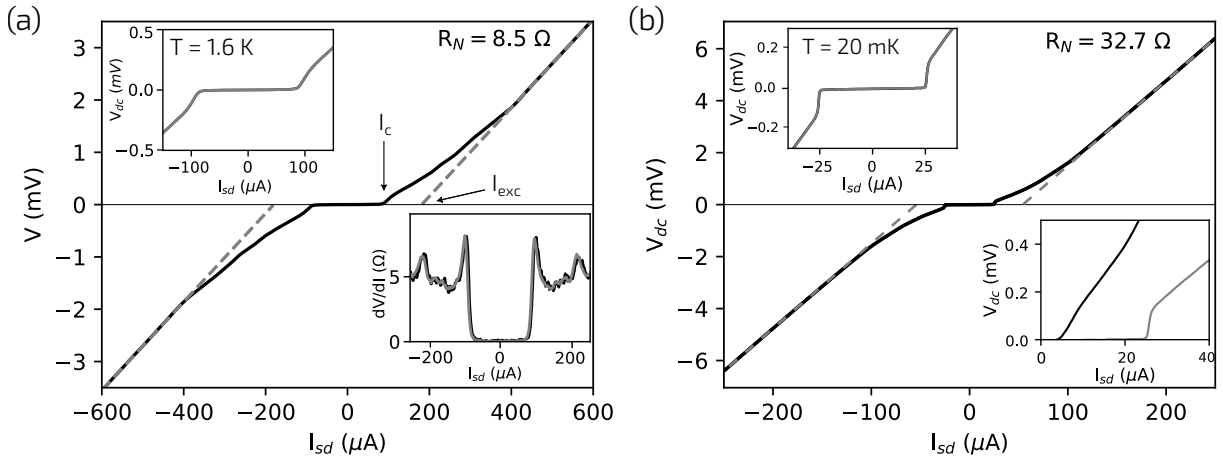

Figure 6.2: IV curve of (a) G743J6 taken at T = 1.6 K and (b) G782J2 taken at 20 mK. The critical (I_c) and excess (I_{exc}) currents are denoted for clarity. A fit to the normal state resistance at eV >> 2Δ is represented as a dashed line with the corresponding normal state resistance R_n indicated in the figure. Top inset, in both figures, shows overlapping bi-directional sweeps of the IV curve with no observable hysteresis. Bottom inset (a) shows the differential resistance versus source-drain current I_{sd}, with characteristics of a hard gap. Bottom inset (b) presents the IV of G782J2 (grey) with $L = 120$ nm in comparison to the IV of G782J4 (black) for a 400 nm junction.

Sample ID	I_c (μA)	I_{exc} (μA)	R_n (Ω)	Δ (meV)	I_cR_n (mV)	$I_{exc}R_n$ (mV)
G743J6 (C1)	102	202	8.14	1.11	0.83	1.60
G743J6 (C2)	89	183	8.55	1.07	0.76	1.60
G743J7 (C2)	52	135	10.28	0.95	0.54	1.40
G782J1	29	58	30	1.25	0.87	1.74
G782J2	25	54	33	1.25	0.83	1.78
G782J3	5	42	39	1.25	0.20	1.64
G782J4	5	24	53	1.10	0.27	1.27
G782J5	2	26	55	1.15	0.11	1.43

Table 6.3: Characteristic electronic properties of SNS junctions on InAs/AlGaSb surface quantum wells from wafers G743 and G782. The values of Δ were determined from the observation of multiple Andreev Reflection (MAR).

voltage V_0. Both junction parameters are determined from the analysis of the IV curve of the junction, as shown in Figure 6.2 and summarized in Table 6.3. As the dc source-drain bias current is swept from zero, a dissipationless current will initially pass through the junction as a supercurrent (no measured voltage drop across the device). Once the bias current exceeds a critical value, the junction will become resistive (finite voltage drop across the sample) and a dissipationless supercurrent will no longer be observed. The value of the bias current at the crossover between the superconducting and finite-resistance states is the critical current of the junction. For ease of the following discussion, we will generally consider only one junction from each generation of samples in the text, G743J6 and G782J2. As mentioned above, the properties of all other junctions are summarized in Table 6.3. The critical current of sample G743J6 is $I_c = 102\mu$A at a temperature of 1.5 K and the critical current of sample G782J2 is 10 μA at 1.6 K and 25 μA at 20 mK. It is worth noting here that our junctions do not exhibit any hysteresis in sweep direction of the IV curves; as emphasized in the top inset of Figures 6.2 a,b which shows bidirectional traces that overlap perfectly (within the step size of I_{sd} corresponding to 2 % of the critical current). This is in contrast to many reports of a switching (retracting) current below I_c, often attributed to Joule heating in the normal state [48, 130]. It is therefore interesting that we do not observe hysteresis in any of our samples, whether measured at a base temperature of 1.6 K or 20 mK. In our systems with large cooling capacity, the sample is immersed in liquid He in contrast to typical in-vacuum He^3-He^4 dilution refrigerators which have minimal cooling wattage available at the mixing stage at base temperature. Thus, the Joule heating of the dissipative current resulted in little to no change in temperature, and therefore no hysteresis in our measurements. Finally, to determine the characteristic voltage, the normal state resistance R_N is given by the slope of the linear portion of the IV curve occuring at $V_{sd} >> 2\Delta$. Given the information in Table 6.3, the characteristic voltages of G743J6 and G782J2 are near 70 % of Δ_{Nb}/e.

A high-quality junction is further characterized by high interface transparency at the SN interfaces, which corresponds to a high probability of Andreev reflection [14, 93, 35, 23]. Because the semiconductor extends under the superconducting region in the planar geometry, the interface is expected to be highly transparent and produce high yields of devices as a result of the large area of contact. This is in contrast to junctions fabricated with etched sidewall contacts to buried quantum wells or nanowires [104, 39, 57]. Since the Andreev reflection process occuring at the interface carries the supercurrent through the normal region, it is reflected in a measure of excess current I_{exc}. As shown in Figure 6.2a,b with dashed lines, a fit to the linear normal state resistance portion of the IV curve ($eV >> \Delta_{Nb}$) intersects the x-axis at a value greater than the critical current, known as the excess current I_{exc} resulting from the Andreev reflection process. As reported in Table

6.3, the excess current for sample G743J6 is $I_{exc} = 202$ μA at T = 1.6 K, while the excess current for sample G782J2 is $I_{exc} = 54$ μA at 20 mK.

In the Josephson regime, the interface transparency t is directly related to the magnitude of the proximity-induced gap inside the semiconductor by the superconducting leads. Significant effort in the last decade has focused on epitaxial Al contacts grown in-situ by MBE on InAs surface quantum well heterostructures in order to achieve $\mathcal{T} \sim 1$. However, epitaxial contacts are not a strict requirement for high-quality interfaces. I demonstrate that our ex-situ contacts are on par with the average reported transparency of in-situ epitaxial aluminum. The interface transparency of Majorana devices with epitaxial aluminum has been reported to be > 0.75 [61, 85, 84, 83]. For a perfectly transparent interface (Z=0, $\mathcal{T} = 1$) the product of $I_{exc}R_n = (4/3)(\Delta/e)$ [14]. Furthermore, for a diffusive junction, the product $I_{exc}R_n$ is approximated by $I_{exc}R_n = (\pi^2/4 - 1)(\Delta/e)$ [4, 22]. Using both formulas, the approximate induced delta determined from $I_{exc}R_n$ is therefore $1.1 < \Delta^* < 1.2$ meV in G743J6 and $1.2 < \Delta^* < 1.3$ meV in G782J2 depending on the transport regime and the transparency of the junction.

Comparing the data for the G782 samples in Table 6.3, which vary as a function of junction length L, we observe a crossover between the short and long junction regime. Between the 120 nm (G782J1, G782J2) and 400 nm (G782J4, G782J5) junctions, the measured critical current and the excess current are reduced. The critical current which is sensitive to elastic scattering in the semiconductor decreases with an increase in junction length by an order of magnitude. The excess current, which is less sensitive to elastic scattering, halves owing to the length exceeding the coherence length. Since the excess current is the result of the Andreev reflection process, it is more sensitive to the loss of phase coherence through non-elastic scattering. Understanding the two regimes, we now take interest in sample G782J3 which has an intermediate length of 150 nm. The excess current of 42 μA is consistent with the 120 nm samples for a junction in the short regime. However, the critical current of 5 μA is more similar to the 400 nm junctions with $L > l_e$ despite having a length $L < l_e$ itself. We therefore speculate that G782J3 is affected by an unfortunately located defect in the semiconductor that enhances elastic scattering and therefore does not change the measured excess current compared to G782J1 and G782J2.

6.3.1 Multiple Andreev Reflection (MAR)

As illustrated in Figure 6.3, Andreev reflection is the mechanism through which an electron incident on an NS interface transmits a Cooper pair into the superconducting region and retro-reflects a hole. In the supercurrent branch of the SNS junction, the incident Cooper

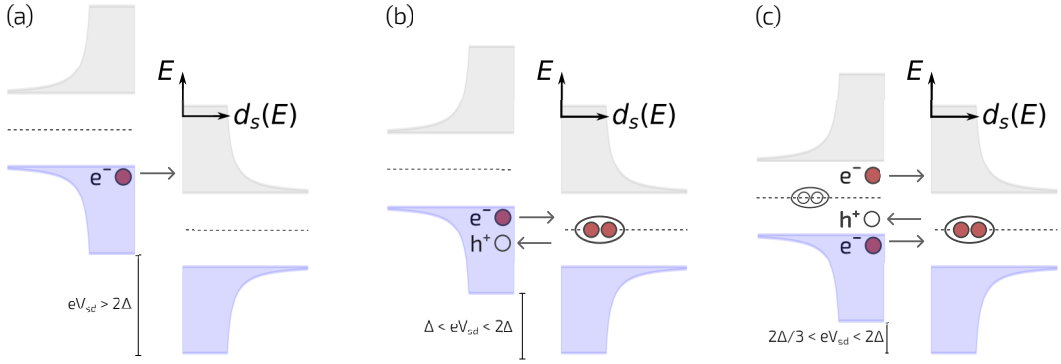

Figure 6.3: Spatial and energy diagram of an SNS junction. A bias eV_{sd} is applied across the junction. (a) An SNS junction with an applied voltage eV_{sd} larger than 2Δ corresponding to single particle transport.(b) 2^{nd} order multiple Andreev reflection. (c) 3^{rd} order multiple Andreev reflections.

pair (at zero energy) is transformed in the N section to a so called Andreev pair with constituent quasiparticles at symmetric energies, and back to a Cooper pair at the other S terminal; thus, Andreev reflection mediated proximity superconductivity. In the finite voltage regime the process of multiple Andreev reflection occurs, the number of Andreev reflections corresponds to the number of times a particle must traverse the gap before $neV_{sd} > 2\Delta$, allowing the particle to escape. The MAR process is important for understanding the behavior of superconducting devices, such as Josephson junctions, and can be used to create entangled electron pairs for quantum computing applications [17].

As shown in Figure 6.4, the supercurrent branch is present at zero bias voltage and the MAR signatures are visible at higher bias. As the bias is swept, the differential conductance of the junction, dI / dV, shows peaks in the bias voltages $V_n = 2\Delta^* / en$ for the integer n = 1, 2, 3, 4 corresponding to the number of Andreev reflections. From the MAR resonances at n = 1 in Figure 6.4a, b, Δ is estimated to be 1.11 mV in G743J6 and 1.05 mV in G782J2.

From the OTBK model describing the behavior of electrons in an SNS junction, a numerical derivation of the relationship between excess current and barrier strength (Z) was derived and is used extensively to determine interface transparencies in experimental devices [14]. More recently, an analytical result was derived in good agreement with the numerical result [92]. The analytical solution is given by

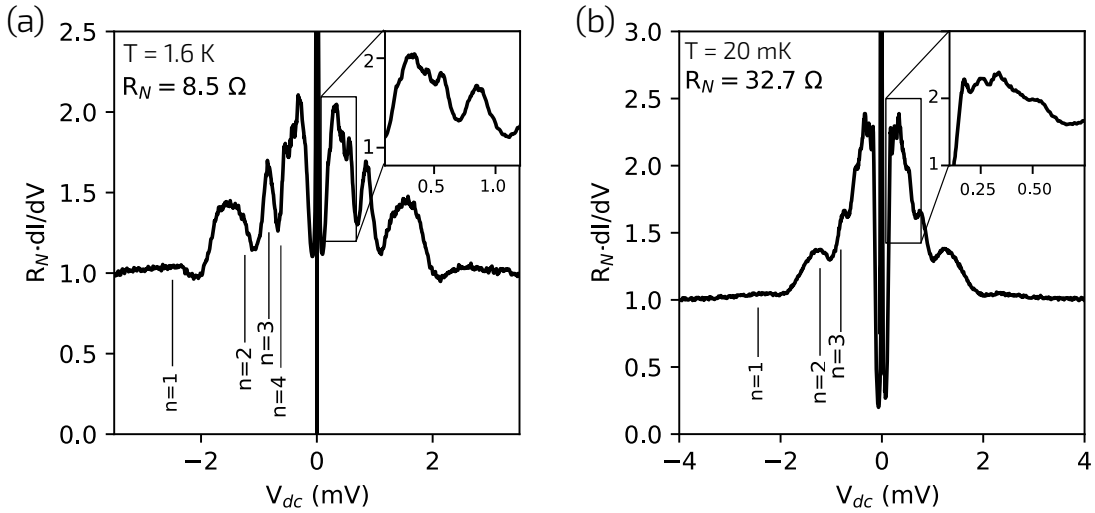

Figure 6.4: Resonant peaks in the conductance normalized to R_n indicating the onset of multiple Andreev reflection (MAR) in wafer (a) G743J6 and (b) G782J2. The numbers n indicate the corresponding order of MAR. Expanded regions highlight higher order oscillations above $n = 4$ indicating stronger coherence in the device.

$$\frac{eI_{exc}R_n}{\Delta} = 2(1+2Z^2)\tanh^{-1}(2Z\sqrt{(1+Z^2)/(1+6Z^2+4Z^4)}) \times (Z\sqrt{(1+Z^2)(1+6Z^2+4Z^4)})^{-1} - \frac{4}{3} \quad (6.1)$$

where I_{exc} and R_n are the excess current and normal state resistance measured in the finite-voltage regime of a Josephson junction. Inserting the figure of merit product $eI_{exc}R_N/\Delta$ of our devices into the OTBK model for the subharmonic gap structure yields the scattering parameter Z and is used to determine the interface transparency according to $\mathcal{T} = (1 + Z^2)^{-1}$. For G743J6 and G782J2, the corresponding contact transparencies are $\mathcal{T} \sim 0.85$ and $\mathcal{T} \sim 0.87$ respectively.

6.3.2 Temperature dependence of the critical current

As presented in Figure 6.5 for sample G743J6, temperature dependence of the critical current conveys further information on the transport behavior of the junction. As shown,

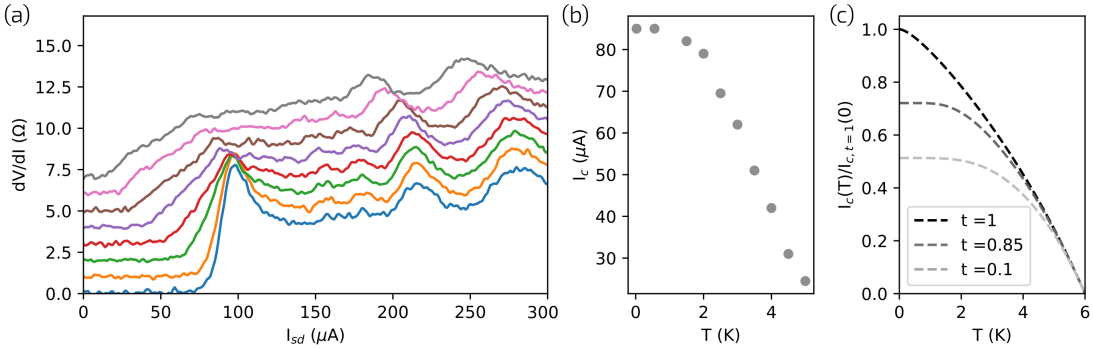

Figure 6.5: (a) Resistance of the junction as the bias current is swept to positive bias in sample G743J6. Each curve is offset by 1 Ω for viewing except for T = 1.6 K. The critical current is considered to be the threshold when $dV/dI > 1\Omega$. (b) Critical current as a function of temperature taken from data in (a). Saturation at low temperature is consistent with the behavior of a diffusive junction. Measurement in the saturated regime is limited by the base temperature of the cryostat at 1.6 K. (c) Equation 6.2 for $\mathcal{T} = 1$ (clean limit), $\mathcal{T} = 0.1$ (dirty limit) and $\mathcal{T} = 0.85$ (G743J6 transparency determined by MAR analysis).

the critical current begins to saturate near 2 K as the temperature decreases, consistent with the behavior of a diffusive junction. Unfortunately, this measurement was limited by the base temperature of our cryostat; otherwise, the measurement would have been conducted further into the saturated regime at low temperature.

For a junction with arbitrary transparency, the temperature dependence of the critical current is given by the generalized Kulik-Omelyanchuk relation [44] where

$$I(T,\phi,\mathcal{T}) = \max\left[\frac{\pi\Delta(T)}{2eR_N}\frac{\sin\phi}{\sqrt{1-\mathcal{T}\sin^2\phi/2}}\tanh\frac{\Delta(T)}{2k_BT}\sqrt{1-\mathcal{T}\sin^2\phi/2}\right] \tag{6.2}$$

Equation 6.2 is plotted in Figure 6.5c in the clean limit ($\mathcal{T} = 1$), in the dirty limit ($\mathcal{T} \ll 1$) and at the approximate transparency of sample G743J6 ($\mathcal{T} = 0.85$). Reasonable qualitative agreement between the behavior of the data and the model for $\mathcal{T} = 0.85$ further supports that our junction is in the diffusive regime with highly transparent interfaces. Although a similar data set has not yet been taken for the second generation of samples, the critical current of sample G782J2 is 10 μA at 1.5 K and improves to 25 μA at 20 mK.

In conclusion, we study Josephson junctions with ex-situ sputtered contacts to InAs 2DEGs using a surface passivation technique to achieve high-transparency contacts. We observe surprisingly consistent and highly transparent junction behavior with $\mathcal{T} = 0.85$ and $\mathcal{T} = 0.87$, respectively, between the two generations of samples in which the passivation parameters were not kept identical. Furthermore, the junction properties $I_c R_n$ and $I_{exc} R_n$ are remarkably agreeable for junctions of the same geometry. We therefore demonstrate that ex-situ contacts to InAs quantum wells are a viable method for reproducible and reliant transparent superconducting electrodes, on par with epitaxial aluminum systems, and do not depend on unreasonably stringent fabrication parameters in the InAs material system.

Chapter 7

Summary and Outlook

7.1 Summary

In this work, surface quantum well heterostructures have been developed in InSb/InAlSb and InAs/AlGaSb material systems using MBE for the experimental realization of proximity superconducting devices. Growth and fabrication challenges are addressed in both systems, resulting in high-quality field-effect devices suitable for ongoing work with electrostatically defined nanoscale devices. With strong spin-orbit interaction and a large Landé g-factor, both material systems have the properties necessary for studying the interplay of proximity superconductivity with Zeeman and SOI effects in the pursuit of topological quantum computation with Majorana zero modes.

Modulation doped, buried quantum wells in InSb/InAlSb were used in Chapter 2 to optimize heterostructure growth parameters and achieved single-subband occupation without parallel conduction at carrier densities near 1×10^{11} cm^{-2} in a 30 nm quantum well. The surface quantum wells in InSb/InAlSb were characterized similarly in Chapter 3. We demonstrate the influence of modulation doping on gating characteristics, magnetotransport behavior, and spin-orbit interaction. The spin-orbit interaction is the highest among modulation-doped InSb heterostructures with a Rashba component of $\sim$100 meVÅ. Magnetoresistance measurements confirm that intentional dopants in InSb are compatible with high-quality and reproducible transport characteristics, without parasitic parallel conduction or unstable carrier densities. As recommended, this could be further tested in a 2DEG heterostructure with a short-period InSb/InAlSb superlattice doping scheme, where only the thin layer is doped.

For the InAs/AlGaSb material system discussed in Chapter 4, buried quantum wells with a lattice-matched AlGaSbAs metamorphic buffer exhibited single subband occupation at a density of $\sim 1 \times 10^{12}$ cm^{-2} for a 24 nm quantum well. Moving the quantum well to the surface drove the quantum well into the second subband because of an increased carrier density from an abundance of surface states and Fermi-level pinning in the conduction band, which was highly influenced by the choice in dielectric for top-gated devices. Ideal gating characteristics were achieved in top-gated devices with a 60 nm SiO_2 gate dielectric and single subband transport was achieved for sufficiently negative gate voltages. These high density quantum wells are ideal for ex-situ fabrication of Josephson junctions with transparent interfaces, as discussed in Chapters 5 and 6, respectively. Josephson SNS junctions were fabricated with ex-situ sputtered Nb contacts to 2DEGs hosted in InAs/AlGaSb surface quantum wells using a bilayer e-beam lithography process for sputtered liftoff. We observed consistent and highly transparent interfaces with values of $\mathcal{T} > 75\%$. This result demonstrates that post-growth superconducting contacts to InAs quantum wells can be a viable method on a par with epitaxial aluminum systems and do not depend on unreasonably stringent fabrication parameters in the InAs material system.

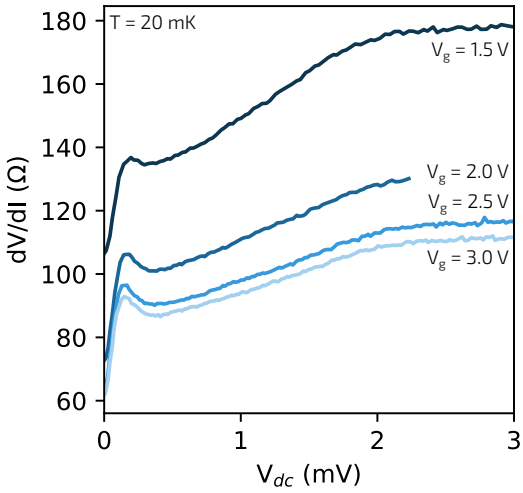

Figure 7.1: Top-gated Josephson junction in wafer G839. Dependence of differential resistance on V_{dc}. The gate voltage corresponding to each trace is indicated. An increase in gate voltage corresponds to an increase in carrier density in the junction. Data taken at a base temperature of 20 mK.

The InSb and InAs material systems studied in this work are both considered candidate material systems for topological superconducting systems. Although similar in terms of inherent material properties of III-V semiconductors, the challenges we faced in materials development were quite different and should be considered when choosing a system for future endeavors. The InSb system requires accommodation for significant lattice mismatch, generally operates in the accumulation regime unless intentionally doped, and contends with a Schottky barrier at the surface. On the contrary, the InAs system belongs to the 6.1 angstrom family of materials, operates in the depletion regime, and accommodates a surface inversion layer at the surface. Despite their differences, the fabrication techniques

developed to minimize degradation of surface quantum wells and fabricate high-quality ex situ superconducting contacts apply readily to both material systems. As such, both systems are mature enough for the ongoing pursuit of nanoscale devices.

7.2 Ongoing work and outlook

Our ongoing work concerns the fabrication and measurement of electrostatically gated Josephson junction devices with ex-situ fabricated contacts. The gated Josephson junctions fabricated in Chapter 6 on InSb substrates achieved smooth metal edges and were gated with a 60 nm HfO_2 gate dielectric and a Ti/Au metal top-gate defined by optical lithography. Figure 7.1 presents the gate dependence of the differential resistance as a function of the DC bias. The field effect from the top-gate induces a 2DEG in the semiconductor junction between the superconducting leads. No supercurrent was observed at gate voltages where a 2DEG is induced in the junction due to the low mobility of the semiconductor (G839) beneath the superconducting leads, but the differential resistance is reduced at small bias voltages compared to the normal state resistance due to the presence of Andreev reflections. For higher gate voltages corresponding to an increase in carrier density, the normal state resistance is reduced. With similar gating behavior observed in all devices fabricated in this sample batch, we conclude that our fabrication method is suitable for a high yield of devices with no observed electrical shorts between the sputtered contacts and the top-gate. Ongoing work will repeat this procedure in a wafer with a populated 2DEG as-grown ($V_g = 0$). Reduced normal scattering in the quantum well beneath the superconducting leads should result in observation of a supercurrent.

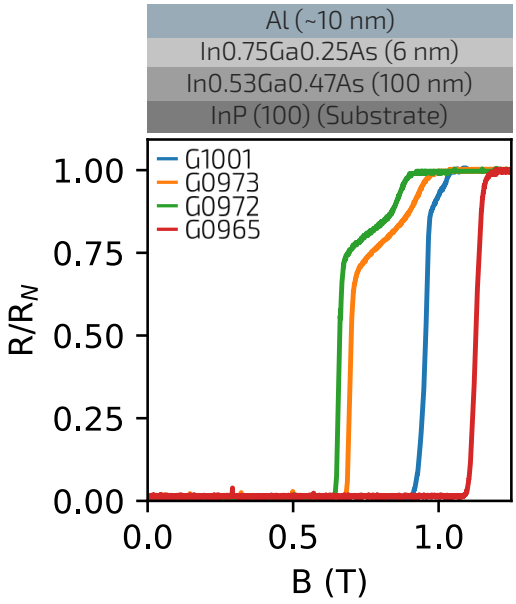

Figure 7.2: Epitaxial aluminum thin films. Critical in-plane magnetic field measurements of epitaxial aluminum films grown on $In_{0.75}Ga_{0.25}As$ as shown schematically above.

Further improvement of interface transparencies is possible with in-situ films which

are considered to be a more reliable process compared to ex-situ fabricated devices. Experiments on characterizing and improving the interface between epitaxial Al and III-V materials are currently being carried out in the Quantum Nano Center-MBE lab. In our submitted report [29], we present a study of epitaxial Al thin film growth at low temperatures on InAs/InGaAs by MBE, focusing on the effect of Al deposition rate, substrate temperature, and rotation during Al deposition on the quality of Al layers grown. As shown in Figure 7.2, the critical field of continuous smooth Al layers is confirmed at a base temperature of 20 mK. Our future work will combine the lithography procedure for smooth metal liftoff of sputtered metals with these epitaxial aluminum systems to enhance the induced superconducting properties through proximity effect transfer in multilayer superconductors [27]. Alternative superconductors such as niobium, which are not typically available in III-V MBE systems, are then more easily integrated in the study of proximity superconducting devices with near-unity transparencies.

Josephson junction devices similar to the ones discussed here are expected to exhibit topological superconductivity hosting Majorana zero modes. It has been suggested that an effective one-dimensional topological superconductor forms in the narrow (1D) semiconductor strip separating the superconducting leads, with Majorana zero modes appearing at the edges of the junction. Simulations of this device structure show a robust topological phase for interface transparencies of 75% and material parameters consistent with our material systems [49]. We are therefore optimistic about the outlook of this project towards the study of robust topological phases and the undoubtedly interesting physics that will result from the interplay of proximity superconductivity with the Zeeman and SOI effects.

References

[1] Purity levels listed by American Elements Inc. are: Ga (8N), As (7N5), In (7N), and Sb (7N).

[2] T. Ando, A. B. Fowler, and F. Stern. Electronic properties of two-dimensional systems. *Rev. Mod. Phys.*, 54:437, 1982.

[3] Tsuneya Ando, Alan B Fowler, and Frank Stern. Electronic properties of two-dimensional systems. *Reviews of Modern Physics*, 54(2):437, 1982.

[4] Sergey Nikolaevich Artemenko, AF Volkov, and AV Zaitsev. On the excess current in microbridges ScS and ScN. *Solid State Communications*, 30(12):771–773, 1979.

[5] Neil W Ashcroft and N David Mermin. *Solid state physics*. Cengage Learning, 2022.

[6] M. Baik, H.-K. Kang, Y.-S. Kang, K.-S. Jeong, Y. An, S. Choi, H. Kim, J.-D. Song, and M.-H. Cho. Electrical properties and thermal stability in stack structure of HfO_2/Al_2O_3/InSb by atomic layer deposition. *Scientific Reports*, 7:11337, 2017.

[7] John Bardeen, Leon N Cooper, and John Robert Schrieffer. Theory of superconductivity. *Physical review*, 108(5):1175, 1957.

[8] Karl-Heinz Bennemann and John B Ketterson. *Superconductivity: Volume 1: Conventional and Unconventional Superconductors Volume 2: Novel Superconductors*. Springer Science & Business Media, 2008.

[9] Djalal Benyahia, K Michalczewski, A Kebłowski, P Martyniuk, J Piotrowski, A Rogalski, et al. Optimization of the interfacial misfit array growth mode of GaSb epilayers on GaAs substrate. *Journal of Crystal Growth*, 483:26–30, 2018.

[10] E Annelise Bergeron, F Sfigakis, Y Shi, George Nichols, PC Klipstein, A Elbaroudy, Sean M Walker, ZR Wasilewski, and J Baugh. Field effect two-dimensional electron gases in modulation-doped InSb surface quantum wells. *Applied Physics Letters*, 122(1):012103, 2023.

[11] E.A. Bergeron, F. Sfigakis, A. Elbaroudy, A.W.M Jordan, F. Thompson, George Nichols, Y. Shi, Man Chun Tam, Z.R. Wasilewski, and J. Baugh. High transparency induced superconductivity in field effect two-dimensional electron gases in undoped InAs/AlGaSb surface quantum wells. *Applied Physics Letters*, Submission Number: APL24-AR-JOSE2023-00951, 2024.

[12] B Andrei Bernevig, Taylor L Hughes, and Shou-Cheng Zhang. Quantum spin Hall effect and topological phase transition in HgTe quantum wells. *science*, 314(5806):1757–1761, 2006.

[13] VN Bessolov and MV Lebedev. Chalcogenide passivation of III-V semiconductor surfaces. *Semiconductors*, 32(11):1141–1156, 1998.

[14] GE Blonder, m M Tinkham, and k TM Klapwijk. Transition from metallic to tunneling regimes in superconducting microconstrictions: Excess current, charge imbalance, and supercurrent conversion. *Physical Review B*, 25(7):4515, 1982.

[15] B Buonacorsi, F Sfigakis, A Shetty, MC Tam, HS Kim, SR Harrigan, F Hohls, ME Reimer, ZR Wasilewski, and J Baugh. Non-adiabatic single-electron pumps in a dopant-free GaAs/AlGaAs 2DEG. *Applied Physics Letters*, 119(11):114001, 2021.

[16] W Chang, SM Albrecht, TS Jespersen, Ferdinand Kuemmeth, P Krogstrup, J Nygård, and Charles M Marcus. Hard gap in epitaxial semiconductor–superconductor nanowires. *Nature nanotechnology*, 10(3):232–236, 2015.

[17] Wei Chen, DN Shi, and DY Xing. Long-range Cooper pair splitter with high entanglement production rate. *Scientific Reports*, 5(1):7607, 2015.

[18] SJ Chung, MA Ball, SC Lindstrom, MB Johnson, and MB Santos. Improving the surface morphology of insb quantum-well structures on gaas substrates. *Journal of Vacuum Science & Technology B: Microelectronics and Nanometer Structures Processing, Measurement, and Phenomena*, 18(3):1583–1585, 2000.

[19] Y. J. Chung, K. A. Villegas Rosales, K. W. Baldwin, P. T. Madathil, K. W. West, M. Shayegan, and L. N. Pfeiffer. Ultra-high-quality two-dimensional electron systems. *Nat. Mater.*, 20:632, 2021.

[20] PT Coleridge. Small-angle scattering in two-dimensional electron gases. *Physical Review B*, 44(8):3793, 1991.

[21] PT Coleridge, R Stoner, and R Fletcher. Low-field transport coefficients in GaAs/$Ga_{1-x}Al_xAs$ heterostructures. *Physical Review B*, 39(2):1120, 1989.

[22] JC Cuevas, J Hammer, J Kopu, JK Viljas, and M Eschrig. Proximity effect and multiple andreev reflections in diffusive superconductor–normal-metal–superconductor junctions. *Physical Review B*, 73(18):184505, 2006.

[23] JC Cuevas, A Martín-Rodero, and A Levy Yeyati. Hamiltonian approach to the transport properties of superconducting quantum point contacts. *Physical Review B*, 54(10):7366, 1996.

[24] Pierre-Gilles De Gennes. *Superconductivity of metals and alloys*. CRC press, 2018.

[25] MT Deng, S Vaitiekėnas, Esben Bork Hansen, Jeroen Danon, M Leijnse, Karsten Flensberg, Jesper Nygård, P Krogstrup, and Charles M Marcus. Majorana bound state in a coupled quantum-dot hybrid-nanowire system. *Science*, 354(6319):1557–1562, 2016.

[26] RB Dingle. Some magnetic properties of metals ii. the influence of collisions on the magnetic behaviour of large systems. *Proceedings of the Royal Society of London. Series A. Mathematical and Physical Sciences*, 211(1107):517–525, 1952.

[27] ACC Drachmann, HJ Suominen, M Kjaergaard, B Shojaei, CJ Palmstrøm, CM Marcus, and F Nichele. Proximity effect transfer from NbTi into a semiconductor heterostructure via epitaxial aluminum. *Nano letters*, 17(2):1200–1203, 2017.

[28] Gene Dresselhaus. Spin-orbit coupling effects in zinc blende structures. *Physical Review*, 100(2):580, 1955.

[29] A. Elbaroudy, B. Khromets, F. Sfigakis, E. Bergeron, Y. Shi, M.C.A. Tam, T. Blaikie, George Nichols, J. Baugh, and Z.R. Wasilewski. Observation of an abrupt 3D-2D morphological transition in thin Al layers grown by MBE on InGaAs surface. *Journal of Science and Technology A.*, Submission Number: JVA23-AR-MBE2024-00767, 2024.

[30] Ahmed Elbaroudy. Optimization of MBE growth of a high-quality 2-dimensional electron gas in InAs/AlGaSb material system for pursuing a top-down approach towards realization of topological qubits. Master's thesis, University of Waterloo, 2020.

[31] C Ellenberger, B Simovič, R Leturcq, T Ihn, SE Ulloa, K Ensslin, DC Driscoll, and AC Gossard. Two-subband quantum Hall effect in parabolic quantum wells. *Physical Review B*, 74(19):195313, 2006.

[32] Joseph Falson and Masashi Kawasaki. A review of the quantum Hall effects in MgZnO/ZnO heterostructures. *Reports on Progress in Physics*, 81(5):056501, 2018.

[33] F. F. Fang and P. J. Stiles. Effects of a tilted magnetic field on a two-dimensional electron gas. *Phys. Rev.*, 178:823, 1968.

[34] Francesca Finocchiaro, Francisco Guinea, and Pablo San-Jose. Topological π junctions from crossed andreev reflection in the quantum Hall regime. *Physical Review Letters*, 120(11):116801, 2018.

[35] K Flensberg, J Bindslev Hansen, and M Octavio. Subharmonic energy-gap structure in superconducting weak links. *Physical Review B*, 38(13):8707, 1988.

[36] Antonio Fornieri, Alexander M Whiticar, F Setiawan, Elías Portolés, Asbjørn CC Drachmann, Anna Keselman, Sergei Gronin, Candice Thomas, Tian Wang, Ray Kallaher, et al. Evidence of topological superconductivity in planar Josephson junctions. *Nature*, 569(7754):89–92, 2019.

[37] T. Fujita, R. Hayashi, M. Kohda, J. Ritzmann, A. Ludwig, A. D. Wieck, and A. Oiwa. Distinguishing persistent effects in an undoped GaAs/AlGaAs quantum well by top-gate-dependent illumination. *J. Appl. Phys.*, 129:234301, 2021.

[38] D Gershoni, CH Henry, and GA Baraff. Calculating the optical properties of multidimensional heterostructures: Application to the modeling of quaternary quantum well lasers. *IEEE journal of quantum electronics*, 29(9):2433–2450, 1993.

[39] Kaveh Gharavi, Gregory W Holloway, Ray R LaPierre, and Jonathan Baugh. Nb/InAs nanowire proximity junctions from Josephson to quantum dot regimes. *Nanotechnology*, 28(8):085202, 2017.

[40] AC Gossard. Modulation doping of semiconductor heterostructures. In *Molecular beam epitaxy and heterostructures*, pages 499–531. Springer, 1985.

[41] M Grayson and F Fischer. Measuring carrier density in parallel conduction layers of quantum Hall systems. *Journal of applied physics*, 98(1), 2005.

[42] Boris Grbić, Renaud Leturcq, Thomas Ihn, Klaus Ensslin, Dirk Reuter, and Andreas D Wieck. Strong spin-orbit interactions and weak antilocalization in carbon-doped p-type GaAs/$Al_xGa_{1-x}As$ heterostructures. *Physical Review B*, 77(12):125312, 2008.

[43] Sinem Erden Gulebaglan, Sirri Batuhan Kalkan, Serkan Sirt, Enver Metin Kendirlik, and Afif Siddiki. The dip effect under integer quantized Hall conditions. *The European Physical Journal B*, 87:1–7, 2014.

[44] W Haberkorn, H Knauer, and J Richter. A theoretical study of the current-phase relation in Josephson contacts. *physica status solidi (a)*, 47(2):K161–K164, 1978.

[45] E.H. Hall. On a new action of the magnet on electric currents. *American Journal of Mathematics*, 2:287–292, 1879.

[46] PH Hao, LC Wang, Fei Deng, SS Lau, and JY Cheng. On the low resistance Au/Ge/Pd Ohmic contact to n-GaAs. *Journal of applied physics*, 79(8):4211–4215, 1996.

[47] Sean Hart, Hechen Ren, Michael Kosowsky, Gilad Ben-Shach, Philipp Leubner, Christoph Brüne, Hartmut Buhmann, Laurens W Molenkamp, Bertrand I Halperin, and Amir Yacoby. Controlled finite momentum pairing and spatially varying order parameter in proximitized HgTe quantum wells. *Nature Physics*, 13(1):87–93, 2017.

[48] Dibyendu Hazra, Lætitia MA Pascal, Hervé Courtois, and Anjan K Gupta. Hysteresis in superconducting short weak links and μ-squids. *Physical Review B*, 82(18):184530, 2010.

[49] Michael Hell, Martin Leijnse, and Karsten Flensberg. Two-dimensional platform for networks of Majorana bound states. *Physical review letters*, 118(10):107701, 2017.

[50] A Hertel, LO Andersen, DMT Van Zanten, M Eichinger, P Scarlino, S Yadav, J Karthik, S Gronin, GC Gardner, MJ Manfra, et al. Electrical properties of selective-area-grown superconductor-semiconductor hybrid structures on silicon. *Physical Review Applied*, 16(4):044015, 2021.

[51] Shinobu Hikami, Anatoly I Larkin, and Yosuke Nagaoka. Spin-orbit interaction and magnetoresistance in the two dimensional random system. *Progress of Theoretical Physics*, 63(2):707–710, 1980.

[52] SH Huang, G Balakrishnan, A Khoshakhlagh, A Jallipalli, LR Dawson, and DL Huffaker. Strain relief by periodic misfit arrays for low defect density GaSb on GaAs. *Applied physics letters*, 88(13), 2006.

[53] Thomas Ihn. *Semiconductor Nanostructures: Quantum states and electronic transport*. OUP Oxford, 2009.

[54] Thomas Ihn. *Semiconductor Nanostructures*. Oxford University Press, 2010.

[55] SV Iordanskii, Yu B Lyanda-Geller, and GE Pikus. Weak localization in quantum wells with spin-orbit interaction. *ZhETF Pisma Redaktsiiu*, 60:199, 1994.

[56] Torsten Karzig, Christina Knapp, Roman M Lutchyn, Parsa Bonderson, Matthew B Hastings, Chetan Nayak, Jason Alicea, Karsten Flensberg, Stephan Plugge, Yuval Oreg, C M Marcus, and M H Freedman. Scalable designs for quasiparticle-poisoning-protected topological quantum computation with Majorana zero modes. *Physical Review B*, 95(23):235305, 2017.

[57] Chung Ting Ke, Christian M Moehle, Folkert K de Vries, Candice Thomas, Sara Metti, Charles R Guinn, Ray Kallaher, Mario Lodari, Giordano Scappucci, Tiantian Wang, R. E. Diaz, G. C. Gardner, M. J. Manfra, and S. Goswami. Ballistic superconductivity and tunable π–junctions in InSb quantum wells. *Nature communications*, 10(1):1–6, 2019.

[58] GA Khodaparast, RC Meyer, XH Zhang, T Kasturiarachchi, RE Doezema, SJ Chung, N Goel, MB Santos, and YJ Wang. Spin effects in InSb quantum wells. *Physica E: Low-dimensional Systems and Nanostructures*, 20(3-4):386–391, 2004.

[59] Giti A Khodaparast, RE Doezema, SJ Chung, KJ Goldammer, and MB Santos. Spectroscopy of Rashba spin splitting in InSb quantum wells. *Physical Review B*, 70(15):155322, 2004.

[60] Morten Kjærgaard, F Nichele, HJ Suominen, MP Nowak, M Wimmer, AR Akhmerov, JA Folk, K Flensberg, J Shabani, w CJ Palmstrøm, et al. Quantized conductance doubling and hard gap in a two-dimensional semiconductor–superconductor heterostructure. *Nature communications*, 7(1):12841, 2016.

[61] Morten Kjærgaard, Henri Juhani Suominen, MP Nowak, AR Akhmerov, J Shabani, CJ Palmstrøm, Fabrizio Nichele, and Charles M Marcus. Transparent semiconductor-superconductor interface and induced gap in an epitaxial heterostructure Josephson junction. *Physical Review Applied*, 7(3):034029, 2017.

[62] E. Kleinbaum, H. Li, N. Deng, G. C. Gardner, M. J. Manfra, and G. A. Csáthy. Disorder broadening of even-denominator fractional quantum Hall states in the presence of a short-range alloy potential. *Phys. Rev. B*, 102:035140, 2020.

[63] PC Klipstein. Hard-wall edge confinement in two-dimensional topological insulators and the energy of the Dirac point. *Physical Review B*, 104(19):195407, 2021.

[64] PC Klipstein, Y Livneh, A Glozman, S Grossman, O Klin, N Snapi, and E Weiss. Modeling InAs/GaSb and InAs/InAsSb superlattice infrared detectors. *Journal of electronic materials*, 43:2984–2990, 2014.

[65] K v Klitzing, Gerhard Dorda, and Michael Pepper. New method for high-accuracy determination of the fine-structure constant based on quantized Hall resistance. *Physical review letters*, 45(6):494, 1980.

[66] S. Komatsu, H. Irie, T. Akiho, T. Nojima, T. Akazaki, and K. Muraki. Gate tuning of fractional quantum Hall states in an InAs two-dimensional electron gas. *Phys. Rev. B*, 105:075305, 2022.

[67] P Krogstrup, NLB Ziino, W Chang, SM Albrecht, MH Madsen, Erik Johnson, Jesper Nygård, Charles M Marcus, and TS Jespersen. Epitaxy of semiconductor–superconductor nanowires. *Nature materials*, 14(4):400–406, 2015.

[68] Ivan Kulesh, Chung Ting Ke, Candice Thomas, Saurabh Karwal, Christian M Moehle, Sara Metti, Ray Kallaher, Geoffrey C Gardner, Michael J Manfra, and Srijit Goswami. Quantum dots in an InSb two-dimensional electron gas. *Physical Review Applied*, 13(4):041003, 2020.

[69] LD Landau. Diamagnetismus der metalle. *Zeitschrift für Physik*, 64:629–637, 1930.

[70] PJPRB Lawaetz. Valence-band parameters in cubic semiconductors. *Physical Review B*, 4(10):3460, 1971.

[71] MV Lebedev. Modification of the atomic and electronic structure of III-V semiconductor surfaces at interfaces with electrolyte solutions. *Semiconductors*, 54(7):699–741, 2020.

[72] Joon Sue Lee, Borzoyeh Shojaei, Mihir Pendharkar, Mayer Feldman, Kunal Mukherjee, and Chris J Palmstrøm. Contribution of top barrier materials to high mobility in near-surface InAs quantum wells grown on GaSb (001). *Physical Review Materials*, 3(1):014603, 2019.

[73] Ch A Lehner, Thomas Tschirky, T Ihn, Werner Dietsche, Janine Keller, Stefan Fält, and Werner Wegscheider. Limiting scattering processes in high-mobility InSb quantum wells grown on GaSb buffer systems. *Physical Review Materials*, 2(5):054601, 2018.

[74] Christian Lehner. On the limitations and prospects of MBE grown high-mobility InSb quantum wells. Ph.D. thesis, ETH Zurich, 2019.

[75] Zijin Lei, Erik Cheah, Km Rubi, Maurice E Bal, Christoph Adam, Rüdiger Schott, Uli Zeitler, Werner Wegscheider, Thomas Ihn, and Klaus Ensslin. High-quality two-dimensional electron gas in undoped InSb quantum wells. *Physical Review Research*, 4:013039, 2022.

[76] Zijin Lei, Christian A Lehner, Erik Cheah, Matija Karalic, Christopher Mittag, Luca Alt, Jan Scharnetzky, Werner Wegscheider, Thomas Ihn, and Klaus Ensslin. Quantum transport in high-quality shallow InSb quantum wells. *Applied Physics Letters*, 115(1):012101, 2019.

[77] Zijin Lei, Christian A Lehner, Erik Cheah, Christopher Mittag, Matija Karalic, Werner Wegscheider, Klaus Ensslin, and Thomas Ihn. Gate-defined quantum point contact in an InSb two-dimensional electron gas. *Physical Review Research*, 3(2):023042, 2021.

[78] Zijin Lei, Christian A Lehner, Km Rubi, Erik Cheah, Matija Karalic, Christopher Mittag, Luca Alt, Jan Scharnetzky, Peter Märki, Uli Zeitler, W. Wegscheider, T. Ihn, and K Ensslin. Electronic g-factor and magnetotransport in InSb quantum wells. *Physical Review Research*, 2(3):033213, 2020.

[79] Y. Livneh, P. C. Klipstein, O. Klin, N. Snapi, S. Grossman, A. Glozman, and E. Weiss. $\mathbf{k} \cdot \mathbf{p}$ model for the energy dispersions and absorption spectra of InAs/GaSb type-II superlattices. *Phys. Rev. B*, 86:235311, 2012.

[80] Y. Livneh, P. C. Klipstein, O. Klin, N. Snapi, S. Grossman, A. Glozman, and E. Weiss. Erratum: $\mathbf{k} \cdot \mathbf{p}$ model for the energy dispersions and absorption spectra of InAs/GaSb type-II superlattices [phys. rev. b 86, 235311 (2012)]. *Phys. Rev. B*, 90:039903, 2014.

[81] M. K. Ma, Md. S. Hossain, K. A. Villegas Rosales, H. Deng, T. Tschirky, W. Wegscheider, and M. Shayegan. Observation of fractional quantum Hall effect in an InAs quantum well. *Phys. Rev. B*, 96:241301(R), 2017.

[82] Philippe Mangin and Rémi Kahn. *Superconductivity: an introduction*. Springer, 2016.

[83] William Mayer, Matthieu C Dartiailh, Joseph Yuan, Kaushini S Wickramasinghe, Enrico Rossi, and Javad Shabani. Gate controlled anomalous phase shift in Al/InAs Josephson junctions. *Nature communications*, 11(1):212, 2020.

[84] William Mayer, William F Schiela, Joseph Yuan, Mehdi Hatefipour, Wendy L Sarney, Stefan P Svensson, Asher C Leff, Tiago Campos, Kaushini S Wickramasinghe, Matthieu C Dartiailh, et al. Superconducting proximity effect in InAsSb surface quantum wells with in situ Al contacts. *ACS Applied Electronic Materials*, 2(8):2351–2356, 2020.

[85] William Mayer, Joseph Yuan, Kaushini S Wickramasinghe, Tri Nguyen, Matthieu C Dartiailh, and Javad Shabani. Superconducting proximity effect in epitaxial Al-InAs heterostructures. *Applied Physics Letters*, 114(10):103104, 2019.

[86] TD Mishima, M Edirisooriya, N Goel, and MB Santos. Dislocation filtering by $Al_xIn_{1-x}Sb$/ $Al_yIn_{1-y}Sb$ interfaces for InSb-based devices grown on GaAs (001) substrates. *Applied physics letters*, 88(19):191908, 2006.

[87] TD Mishima, JC Keay, N Goel, MA Ball, SJ Chung, MB Johnson, and MB Santos. Effect of micro-twin defects on InSb quantum wells. *Journal of Vacuum Science & Technology B: Microelectronics and Nanometer Structures Processing, Measurement, and Phenomena*, 23(3):1171–1173, 2005.

[88] Sumit Mondal, Geoffrey C Gardner, John D Watson, Saeed Fallahi, Amir Yacoby, and Michael J Manfra. Field-effect-induced two-dimensional electron gas utilizing modulation-doped Ohmic contacts. *Solid state communications*, 197:20–24, 2014.

[89] Christopher Moore, Chuanchang Zeng, Tudor D Stanescu, and Sumanta Tewari. Quantized zero-bias conductance plateau in semiconductor-superconductor heterostructures without topological Majorana zero modes. *Physical Review B*, 98(15):155314, 2018.

[90] Vincent Mourik, Kun Zuo, Sergey M Frolov, SR Plissard, Erik PAM Bakkers, and Leo P Kouwenhoven. Signatures of Majorana fermions in hybrid superconductor-semiconductor nanowire devices. *Science*, 336(6084):1003–1007, 2012.

[91] B. Nedniyom, R. J. Nicholas, M. T. Emeny, L. Buckle, A. M. Gilbertson, P. D. Buckle, and T. Ashley. Giant enhanced g-factors in an InSb two-dimensional gas. *Phys. Rev. B*, 80:125328, 2009.

[92] Gabriel Niebler, Gianaurelio Cuniberti, and Tomáš Novotnỳ. Analytical calculation of the excess current in the Octavio–Tinkham–Blonder–Klapwijk theory. *Superconductor Science and Technology*, 22(8):085016, 2009.

[93] M Octavio, M Tinkham, GE Blonder, and TM Klapwijk. Subharmonic energy-gap structure in superconducting constrictions. *Physical Review B*, 27(11):6739, 1983.

[94] JMS Orr, Philip Derek Buckle, M Fearn, PJ Wilding, CJ Bartlett, MT Emeny, L Buckle, and T Ashley. Schottky barrier transport in InSb/AlInSb quantum well field effect transistor structures. *Semiconductor Science and Technology*, 21(10):1408, 2006.

[95] JMS Orr, AM Gilbertson, M Fearn, OW Croad, CJ Storey, L Buckle, MT Emeny, Philip Derek Buckle, and T Ashley. Electronic transport in modulation-doped InSb quantum well heterostructures. *Physical Review B*, 77(16):165334, 2008.

[96] Wei Pan, JS Xia, HL Stormer, DC Tsui, C Vicente, ED Adams, NS Sullivan, LN Pfeiffer, KW Baldwin, and KW West. Experimental studies of the fractional quantum Hall effect in the first excited landau level. *Physical Review B*, 77(7):075307, 2008.

[97] Loren Pfeiffer and KW West. The role of MBE in recent quantum Hall effect physics discoveries. *Physica E: Low-dimensional systems and Nanostructures*, 20(1-2):57–64, 2003.

[98] OJ Pooley, AM Gilbertson, Philip Derek Buckle, RS Hall, L Buckle, MT Emeny, M Fearn, LF Cohen, and T Ashley. Transport effects in remote-doped InSb/Al_xIn_{1-x}Sb heterostructures. *New Journal of Physics*, 12(5):053022, 2010.

[99] OJ Pooley, AM Gilbertson, Philip Derek Buckle, RS Hall, MT Emeny, M Fearn, MP Halsall, LF Cohen, and Tim Ashley. Quantum well mobility and the effect of gate dielectrics in remote doped InSb/Al_xIn_{1-x}Sb heterostructures. *Semiconductor Science and Technology*, 25(12):125005, 2010.

[100] Fanming Qu, Jasper Van Veen, Folkert K De Vries, Arjan JA Beukman, Michael Wimmer, Wei Yi, Andrey A Kiselev, Binh-Minh Nguyen, Marko Sokolich, Michael J

Manfra, F. Nichele, C. M. Marcus, and L. P. Kouwenhoven. Quantized conductance and large g-factor anisotropy in InSb quantum point contacts. *Nano letters*, 16(12):7509–7513, 2016.

[101] E.I. Rashba. Properties of semiconductors with an extremum loop. i. cyclotron and combinational resonance in a magnetic field perpendicular to the plane of the loop. *Sov. Phys.-Solid State*, 2:1109, 1960.

[102] M Reed, W Kirk, and P Kobiela. Investigation of parallel conduction in GaAs/Al_xGa_{1-x}As modulation-doped structures in the quantum limit. *IEEE journal of quantum electronics*, 22(9):1753–1759, 1986.

[103] Hechen Ren, Falko Pientka, Sean Hart, Andrew T Pierce, Michael Kosowsky, Lukas Lunczer, Raimund Schlereth, Benedikt Scharf, Ewelina M Hankiewicz, Laurens W Molenkamp, et al. Topological superconductivity in a phase-controlled Josephson junction. *Nature*, 569(7754):93–98, 2019.

[104] Leonid P Rokhinson, Xinyu Liu, and Jacek K Furdyna. The fractional ac Josephson effect in a semiconductor-superconductor nanowire as a signature of Majorana particles. *Nature Physics*, 8(11):795–799, 2012.

[105] M Rudolph and Jean J Heremans. Spin-orbit interaction and phase coherence in lithographically defined bismuth wires. *Physical Review B*, 83(20):205410, 2011.

[106] Yusuff Adeyemi Salawu, Jae Hyun Yun, Jong-Soo Rhyee, Minoru Sasaki, and Heon-Jung Kim. Weak antilocalization, spin–orbit interaction, and phase coherence length of a Dirac semimetal $Bi_{0.97}Sb_{0.03}$. *Scientific Reports*, 12(1):2845, 2022.

[107] Thomas Schäpers. *Superconductor/semiconductor junctions*, volume 174. Springer Science & Business Media, 2001.

[108] E Fred Schubert. *Light-Emitting Diodes (2006)*. Cambridge University Press, 2006.

[109] L Schubnikov and WJ De Haas. A new phenomenon in the change of resistance in a magnetic field of single crystals of bismuth. *Nature*, 126(3179):500–500, 1930.

[110] Javad Shabani, Morten Kjærgaard, Henri J Suominen, Younghyun Kim, Fabrizio Nichele, Kiryl Pakrouski, T Stankevic, Roman M Lutchyn, Peter Krogstrup, R Feidenhans, S Kraemer, C Nayak, M Troyer, C. M. Marcus, and C J Palmstrøm. Two-dimensional epitaxial superconductor-semiconductor heterostructures: A platform for topological superconducting networks. *Physical Review B*, 93(15):155402, 2016.

[111] A. Shetty, F. Sfigakis, W. Y. Mak, K. Das Gupta, B. Buonacorsi, M. C. Tam, H. S. Kim, I. Farrer, A. F. Croxall, H. E. Beere, A. R. Hamilton, M. Pepper, D. G. Austing, S. A. Studenikin, A. Sachrajda, M. E. Reimer, Z. R. Wasilewski, D. A. Ritchie, and J. Baugh. Effects of biased and unbiased illuminations on two-dimensional electron gases in dopant-free GaAs/AlGaAs. *Physical Review B*, 105:075302, 2022.

[112] Y. Shi, E. Bergeron, F. Sfigakis, J. Baugh, and Z. R. Wasilewski. Hillock-free and atomically smooth InSb QWs grown on GaAs substrates by MBE. *Journal of Crystal Growth*, 513:15, 2019.

[113] Y. Shi, D. Gosselink, K. Gharavi, J. Baugh, and Z. R. Wasilewski. Optimization of metamorphic buffers for MBE growth of high quality AlInSb/InSb quantum structures: Suppression of hillock formation. *Journal of Crystal Growth*, 477:7, 2017.

[114] Y. Shi, D. Gosselink, V. Y. Umansky, J. L. Weyher, and Z. R. Wasilewski. Threading dislocations in MBE grown AlInSb metamorphic buffers: Revealed and counted. *Journal of Vacuum Science and Technology B*, 35:02B112, 2017.

[115] Yinqiu Shi. *Molecular beam epitaxial growth of InSb quantum well heterostructures for applications in topological quantum computing*. PhD thesis, University of Waterloo, 2021.

[116] Yiqiu Shi. Molecular beam epitaxial growth of InSb quantum well heterostructures for applications in topological quantum computing. Ph.D. thesis, University of Waterloo, 2021.

[117] I Shlimak, K-J Friedland, V Ginodman, and SV Kravchenko. Disorder-induced features of the transverse resistance in a Si-MOSFET in the quantum Hall effect regime. *physica status solidi c*, 3(2):309–312, 2006.

[118] I Shlimak, V Ginodman, K-J Friedland, and SV Kravchenko. Manifestation of the exchange enhancement of valley splitting in the quantum Hall effect regime. *Physical Review B*, 73(20):205324, 2006.

[119] B Shojaei, ACC Drachmann, M Pendharkar, DJ Pennachio, MP Echlin, PG Callahan, S Kraemer, TM Pollock, Charles M Marcus, and CJ Palmstrøm. Limits to mobility in InAs quantum wells with nearly lattice-matched barriers. *Physical Review B*, 94(24):245306, 2016.

[120] John Singleton. *Band theory and electronic properties of solids*, volume 2. OUP Oxford, 2001.

[121] N Tajik, CM Haapamaki, and RR LaPierre. Photoluminescence model of sulfur passivated p-InP nanowires. *Nanotechnology*, 23(31):315703, 2012.

[122] C. Thomas, A. T. Hatke, A. Tuaz, R. Kallaher, T. Wu, T. Wang, R. E. Diaz, G. C. Gardner, M. A. Capano, and M. J. Manfra. High-mobility InAs 2DEGs on GaSb substrates: A platform for mesoscopic quantum transport. *Phys. Rev. Mater.*, 2:104602, 2018.

[123] C Thomas, AT Hatke, A Tuaz, R Kallaher, T Wu, T Wang, RE Diaz, GC Gardner, MA Capano, and MJ Manfra. High-mobility inas 2degs on gasb substrates: A platform for mesoscopic quantum transport. *Physical Review Materials*, 2(10):104602, 2018.

[124] Michael Tinkham. *Introduction to superconductivity*. Courier Corporation, 2004.

[125] T. Tschirky, S. Mueller, Ch. A. Lehner, S. Fält, T. Ihn, K. Ensslin, and W. Wegscheider. Scattering mechanisms of highest-mobility InAs/$Al_xGa_{1-x}Sb$ quantum wells. *Phys. Rev. B*, 95:115304, 2017.

[126] G. Tuttle, H. Kroemer, and J. H. English. Effects of interface layer sequencing on the transport properties of InAs/AlSb quantum wells: Evidence for antisite donors at the InAs/AlSb interface. *J. Appl. Phys.*, 67:3032, 1990.

[127] MM Uddin, HW Liu, KF Yang, K Nagase, K Sekine, CK Gaspe, TD Mishima, MB Santos, and Y Hirayama. Gate depletion of an InSb two-dimensional electron gas. *Applied Physics Letters*, 103(12):123502, 2013.

[128] V Umansky, Moty Heiblum, Y Levinson, J Smet, J Nübler, and Merav Dolev. MBE growth of ultra-low disorder 2DEG with mobility exceeding 35×10^6 cm^2/vs. *Journal of Crystal Growth*, 311(7):1658–1661, 2009.

[129] Leo J van der Pauw. A method of measuring the resistivity and Hall coefficient on lamellae of arbitrary shape. *Philips technical review*, 20:220–224, 1958.

[130] D Yu Vodolazov and FM Peeters. Origin of the hysteresis of the current voltage characteristics of superconducting microbridges near the critical temperature. *Physical Review B*, 84(9):094511, 2011.

[131] Igor Vurgaftman, J áR Meyer, and L Ramdas Ram-Mohan. Band parameters for III-V compound semiconductors and their alloys. *Journal of applied physics*, 89(11):5815–5875, 2001.

[132] Zhong Wan, Aleksandr Kazakov, Michael J Manfra, Loren N Pfeiffer, Ken W West, and Leonid P Rokhinson. Induced superconductivity in high-mobility two-dimensional electron gas in gallium arsenide heterostructures. *Nature communications*, 6(1):7426, 2015.

[133] LC Wang, PH Hao, JY Cheng, F Deng, and SS Lau. Ohmic contact formation mechanism of the Au/Ge/Pd/n-GaAs system formed below 200°C. *Journal of applied physics*, 79(8):4216–4220, 1996.

[134] PT Webster, NA Riordan, S Liu, EH Steenbergen, RA Synowicki, Y-H Zhang, and SR Johnson. Measurement of InAsSb bandgap energy and InAs/InAsSb band edge positions using spectroscopic ellipsometry and photoluminescence spectroscopy. *Journal of Applied Physics*, 118(24), 2015.

[135] Kaushini S Wickramasinghe, William Mayer, Joseph Yuan, Tri Nguyen, Lucy Jiao, Vladimir Manucharyan, and Javad Shabani. Transport properties of near surface InAs two-dimensional heterostructures. *Applied Physics Letters*, 113(26), 2018.

[136] Michael G Wood, Christopher P Hains, Patrick Sean Finnegan, Chad A Stephenson, John F Klem, and Quinn Looker. Formation of Ohmic contacts to n-GaAs at temperatures compatible with indium flip-chip bonding. In *Electrochemical Society Meeting Abstracts 236*, number 13, pages 881–881. The Electrochemical Society, Inc., 2019.

[137] K. F. Yang, H. W. Liu, T. D. Mishima, M. B. Santos, K. Nagase, and Y. Hirayama. Nonlinear magnetic field dependence of spin polarization in high-density two-dimensional electron systems. *New J. Phys.*, 13:083010, 2011.

[138] Wei Yi, Andrey A Kiselev, Jacob Thorp, Ramsey Noah, Binh-Minh Nguyen, Steven Bui, Rajesh D Rajavel, Tahir Hussain, Mark F Gyure, Philip Kratz, Q. Qian, M. J. Manfra, V. S. Pribiag, L. P. Kouwenhoven, C. M. Marcus, and M Sokolich. Gate-tunable high mobility remote-doped InSb/$In_{1-x}Al_xSb$ quantum well heterostructures. *Applied Physics Letters*, 106(14):142103, 2015.

[139] PeterY Yu. *Fundamentals of semiconductors*. Springer, 2005.

[140] Teng Zhang, Tyler Lindemann, Geoffrey C Gardner, Sergei Gronin, Tailung Wu, and Michael J Manfra. Mobility exceeding 100000 cm^2/Vs in modulation-doped shallow InAs quantum wells coupled to epitaxial aluminum. *Physical Review Materials*, 7(5):056201, 2023.

[141] XC Zhang, Donald Richard Faulhaber, and HW Jiang. Multiple phases with the same quantized Hall conductance in a two-subband system. *Physical review letters*, 95(21):216801, 2005.

[142] Tong Zhou, Matthieu C Dartiailh, William Mayer, Jong E Han, Alex Matos-Abiague, Javad Shabani, and Igor Žutić. Phase control of Majorana bound states in a topological x junction. *Physical review letters*, 124(13):137001, 2020.

[143] Tong Zhou, Matthieu C Dartiailh, Kasra Sardashti, Jong E Han, Alex Matos-Abiague, Javad Shabani, and Igor Žutić. Fusion of Majorana bound states with mini-gate control in two-dimensional systems. *Nature Communications*, 13(1):1738, 2022.

APPENDICES

Appendix A

Fabrication recipes for surface quantum wells

All devices discussed in this thesis were fabricated in the Quantum-Nano Fabrication and Characterization Facility (QNFCF) at the University of Waterloo.

A.1 Preparation

1. **Cleave** wafer (generally 2 or 3 inch wafers) into smaller rectangular pieces for processing. Wafers are cleaved along the x and y perpendicular wafer orientations.
2. **Clean** the sample in acetone and isopropal alcohol (IPA): Submerge cleaved sample into a plastic beaker of acetone and sonicate the sample for 10 minutes, transfer to a beaker of IPA and repeat sonication. Blow dry with N_2.

A.2 Mesa

1. **Photolithography (S1811 single layer)**
   (a) Spin S1811 at 5000 rpm for 60 s with a ramp rate of 1000 rpm/s.
   (b) Bake S1811 for 90 s at 120 °C.
   (c) Expose using either a SUSS MA6 aligner or a MLA150 Direct Write UV Lithography system (both systems are available at QNFCF).

(d) Develop in MF319 for 1 minute 30 seconds, rinse in deionized (DI) water for 30 s and blow dry with N_2. Confirm development under microscope, add development time if necessary.

2. Mesa etch

   (a) **Plasma ash** (YES CV-200RFS Photoresist Asher) for 20 s at an RF power of 50 W, a pressure of 100 mTorr, and an O2 flow of 10 sccm. Ashing removes any resist residue that might remain within the developed pattern following photolithography.

   (b) Use a profilometer to measure the thickness of spin-coated resist.

   (c) Remove the native oxide using a Buffered Oxide Etch (BOE, HF:NH4F 1:10 parts by volume). Dip the sample in BOE for 30 s and follow with a rinse in DI water for approximately 2 minutes.

   (d) Transfer the wafer to a mesa etch solution (a solution of H_2O_2:H_3PO_4:$C_6H_8O_7$:H_2O mixed 3:4:9:44 by volume) with an etch rate of approximately 3 nm/s. Aim to etch through the quantum well into the buffer, approximately 100 nm for a surface QW.

   (e) Return to profilometer to check the depth that has been etched (Measured depth - resist thickness = etch depth).

3. Strip resist using the standard clean procedure described in the preparation section. Confirm etch depth with profilometer.

A.3 Ohmics

1. **Photolithography (MMA EL10/S1811 bi-layer)**

   (a) Spin MMA EL10 at 5000 rpm for 60 s with a ramp rate of 1000 rpm/s.

   (b) Bake MMA EL10 for 5 minutes at 150 °C.

   (c) Spin S1811 at 5000 rpm for 60 s with a ramp rate of 1000 rpm/s.

   (d) Bake S1811 for 90 s at 120 °C.

   (e) Expose S1811 using either a SUSS MA6 aligner or a MLA150 Direct Write UV Lithography system (both systems are available at QNFCF).

   (f) Develop in MF319 for 1 minute 30 seconds (or until fully developed).

(g) Re-flow bake the resist for 5 minutes at 150 °C.

(h) Expose MMA EL10 using UV ozone for 10 minutes at 9 mm.

(i) Develop MMA EL10 in a solution of IPA:H_2O with a ratio of 7:3 parts by volume for 2 minutes 30 seconds. Rinse in DI water for at least 30 seconds and blow dry with N_2.

(j) Plasma ash (see A.2 for details)

2. **Sulphur passivation**:

   (a) Prepare sulphur passivation solution

      i. Place 500 mg of sulphur powder in a beaker and top-up with ammonium sulfide to 5 mL.

      ii. Sonicate mixture until the sulphur powder is completely dissolved and the solution appears clear (approximately 30 minutes).

      iii. Draw 1 mL of ammonium sulfide solution and dilute with 500 mL of DI water.

   (b) Dip the sample in BOE (HF:NH4F 1:10 parts by volume) for 3 s and follow with a rinse in DI water for approximately 20 minutes.

   (c) Transfer immediately to sulphur passivation solution and passivate for 5 minutes with light.

   (d) Rinse for 30 s in DI water, blow dry with N_2, and transfer quickly to a deposition chamber (minimize the time spent in air).

3. Thermal evaporation (Ti/Au, 20/80 nm, 2/4 A/s) at a chamber pressure of 1.5×10^{-6} Torr.

4. **Lift-off**: Leave overnight in PG-remover then rinse with acetone followed by IPA and finally blow dry with N_2. Do not sonicate the sample once metal has been deposited.

A.4 Atomic layer deposition (ALD)

1. Clean the chamber (Oxford PlasmaLab 100 FlexAL ALD system).

2. Condition the chamber with 20 nm of low-temperature oxide (HfO_2 with TEMAH precursor, Al_2O_3 with TMA precursor, and SiO_2 with BTBAS precursor). The oxide is deposited at 150 °C with a deposition rate of approximately 0.1 nm/cycle.

3. Deposit 60 nm of oxide at at 150 °.

A.5 Vias

1. Photolithography (S1811 single layer)
2. Plasma ash (see A.2 for details)
3. Use a profilometer to measure the thickness of spin-coated resist.
4. Wet-etch the HfO_2 using BOE (HF:NH4F 1:10 parts by volume). The etch rate for HfO_2 deposited at 150 °C in our system was found to be 4-5 s/nm.
5. Confirm etch depth with profilometer (equivalent to thickness of oxide)
6. Strip resist

A.6 Top-gate and bond pads

1. Photolithography (MMA EL10/S1811 bi-layer)
2. Plasma ash (see details in section A.2.)
3. Thermal evaporation (Ti/Au 20/80 nm 2/4 A/s)
4. Strip resist

A.7 SNS

1. Preparation (see A.1 for details)
2. Mesa (See A.2 for details)
3. Optical alignment marks (Ti/Au 20/100 nm)
4. E-beam alignment marks (Ti/Au 20/100 nm)
5. E-beam for Nb (See Chapter 6)

(a) Exposure parameters for using a 100 kV excitation voltage. The beam current is ∼1 nA with a beam size of ∼17 nm.

(b) Develop in IPA:DI water for 30 seconds and check under microscope.

6. Sulphur passivation (see Chapter 6)

7. Sputtered Ti/Nb in AJA conductors chamber at room temperature:

   (a) Ion mill 2 minutes with shutter closed at 50 W and 2 mT then open shutter and continue for 6.5 minutes. Ion milling removes 2-3 nm of native oxide and sulphur.

   (b) Sputter 2 nm of Ti at 200 W (Deposition rate is 8.92 nm/min).

   (c) Sputter 80 nm of Nb at 200 W (Deposition rate is 9.36 nm/min).

   (d) Lift-off overnight in PG remover followed by 20 minutes in heated PG remover (no stirrer) and 20 minutes in heated PG remover with stirrer at 350 rpm. Remove from hotplate and pipet for 5 minutes with glass pipet. Transfer sample to plastic beaker filled with acetone and sonicate for 20 seconds (do not expose to air). Rinse with acetone and propanol then blow dry with nitrogen gun.

8. SNS Interconnects: Optical lithography pattern is available on MLA or optical lithography mask. Lithography and metal deposition details are the same as in section A.6.

9. Atomic layer deposition (ALD) (See A.4 for details)

10. Vias (See A.5 for details)

11. Top-gate and bond pads (see A.6 for details)